Optical spectroscopy of indirect excitons and electron spins in semiconductor nanostructures

Chahine Abbas

THÈSE POUR OBTENIR LE GRADE DE DOCTEUR DE L'UNIVERSITÉ DE MONTPELLIER

Spécialité: Physique

École doctorale: I2S

Unité de recherche : Laboratoire Charles Coulomb

Optical spectroscopy of indirect excitons and electron spins in semiconductor nanostructures

Présentée par Chahine ABBAS

Le 14 octobre 2019

Sous la direction de Maria VLADIMIROVA et Denis SCALBERT

Devant le jury présidé par Brahim GUIZAL et composé de

Maria CHAMARRO	Professeur des Universités	INSP (Paris)	Rapporteur
Thierry AMAND	Directeur de recherche	LPCNO (Toulouse)	Rapporteur
Vasilii BELYKH	Senior researcher	LPI RAS (Moscou)	Examinateur
Brahim GUIZAL	Professeur des Universités	L2C (Montpellier)	Examinateur
Maria VLADIMIROVA	Directeur de recherche	L2C (Montpellier)	Directeur de thèse
Denis SCALBERT	Directeur de recherche	L2C (Montpellier)	Directeur de thèse
Steeve CRONENBERGER	Maître de conférence	L2C (Montpellier)	Membre invité

UNIVERSITÉ DE MONTPELLIER

Abstract

Encoding information on the electron spin degree of freedom is seriously considered as a way to take over the actual microelectronic technology. In this context, controlling the spin state of a system is of crucial importance. Spin dynamics in semiconductors has therefore become an active research field. In this work, we use three different optical techniques to study two different spin systems.

Excitons are bosonic quasi-particles which were predicted to form quantum collective states. Such phenomena being governed by the excitonic fine structure, understanding the excitons spin dynamics is essential to their comprehensive study. In this work, indirect excitons in GaAs/(AlGa)As asymmetric coupled quantum wells are studied by two different methods: time and polarisation resolved photoluminescence and pump-probe spectroscopy. Optimal conditions have been identified to obtain long lifetime and spin relaxation time which have been found to reach $\tau_r = 15$ ns and $\tau_s = 5$ ns respectively in photoluminescence. Spin coherence of this system have also been studied with a particular pump-probe setup with a very low repetition rate. In this case, the spin relaxation time reaches 25 ns.

Beside these two widely used optically methods, spin noise spectroscopy has more recently emerged as a very interesting tool. It provides information on spin dynamics without perturbing it, via spontaneous spin fluctuations. They are detected optically as fluctuations of the polarisation state of the off-resonant laser beam.
Until this work, this technique was limited to temporal spin dynamics. Here, we present a setup allowing for study both spatial and temporal spin dynamics. As a first application we studied electron gas in n-doped CdTe thin layers. In this material, the spin dynamics is expected to present similarity with the much better known GaAs. We actually observe the precession of electrons in the randomly fluctuating nuclear field which has already been reported in GaAs. It allowed for the determination of the nuclear field at saturation in CdTe $B_S = 0.11$ T.
Simultaneous measurements of both spin relaxation time and spin diffusion coefficient by spatio-temporal spin noise spectroscopy are performed in different experimental conditions. Their variation as a function of the electron correlation time on a donor site can be interpreted in term of a competition between the hyperfine interaction and the anisotropic exchange interaction. In the long correlation time regime - when the hyperfine interaction dominates - a transition from inhomogeneous to homogeneous broadening is observed. This transition is confirmed by a modification of the shape

of spin noise spectra. However, this model matches the experimental data only if we consider an active donor concentration reduced by several orders of magnitudes with respect to the nominal values. This is a strong clue that our knowledge of spin relaxation in GaAs can not be directly transposed to CdTe.

Acknowledgements

I would like to thank everyone who contributed to the realisation of this work. Many thanks to my advisors, Masha, Denis and Steeve which were always available and understanding. I also thank the referees and examiners in my thesis jury: Maria Chamarro, Thierry Amand, Vasilii Belykh and Brahim Guizal. I really appreciated your interest and your constructive comments.
So much people contributed to make the three last years a great experience. Among them, I am grateful to Vasilii Belykh who supervised me during my stay in Dortmund. To those of the E2 lab who welcomed me, many thanks for this very nice opportunity. Everyone in the L2C lab being always available for helping or giving a piece of advice and I thank every one in this lab, more particularly Pierre valvin, Christian Lhenoret and Abir Nachawaty.

I am also indebted to some person which are important to me and I have the pleasure to thank them. Of course my parent for all they gave me. Thank you *baba*, thank you *maman*, thank you *sito*.
I am infinitely grateful to the pedagogic team of the University of Avignon without whom, none of this would have been possible. Thank you Philippe Lieutaud for your illimited forbearance. Thank you Gilles Micolau for all the opportunities you gave me. I sincerly hope that our academic paths will be closer an closer. I also wait this writing time for several years to dedicate this work to my men Cyril Gignoux who plays a important role in Avignon. The presence of both of you to my defense was an immense pleasure.
There are also some people in the L2C lab who are greatly involved in this achievement: Hervé Peyre, Brahim Guizal and Mauro Antezza. Many thanks to both of you. Brahim, I am truly honoured that you have been the president of my thesis jury.

Finally, I would like to thank all my entourage for the last three years. Of course, many thanks to my wife, my little brother and my young sister for their unfailing support.
It was a pleasure to share my office with so much nice people: Hamis, Richard, Florian, Pierre, Maha, François, Anthony, Clément, Minggang and Kevin. Thank you all. François, I sincerly think that your presence in the lab is a blessing for so many people. As far I am concerned, I really appreciated all our stimulating discussions, your joyful presence and your comforting empathy. You learnt me more than you think. I wish you the best for the future.

I will finish with some special mentions. Pascale, Denis, Sandrine, Olivier : it seems to be finished! Pierre Doyeux, you are a good friend and your advices were important to me. Abir Nachawaty, you achieved a miracle: your help has been providential. I wish you the very best in your life. Jean-Marc Nicollet, you are a boss. My regards to my friends Farid, Omar, Sofiane, Iadh, Ashraf, Fabrice, Mouhssine, Néné and Omar again, to the family Beghidja, and to the Abbes brotherhood.
Love to my very young daughter (DON'T TOUCH the Masha's *"Spin physics in semiconductors"* book!) and to my baby boy (I will rapidly give back the book to Masha!).

Contents

Introduction

The last few years have witnessed a slowdown in the evolution of the classical electronic devices performances [1]. The microelectronic industry does not follow the Moore's law anymore and has increasingly focused on the needs of the IoT market segment. Additionally, the research for new technologies going beyond actual limitations is still in progress.
In this context, quantum features - such as superposition or entanglement - acquire technological interest in several application fields. They include long-distance quantum communication [2, 3], quantum sensors [4], quantum imaging [5, 6] and quantum computing and are based on various material systems. Quantum simulations are for instance performed in cold atom systems [7], in trapped ion systems [8] and in polariton condensates [9]. Solid state quantum bits - of which integration in consumer devices should be easier - are also implemented. Major industrial actors bet for example on superconducting Josephson junctions [10]. Electron and nuclear spins in semiconductors are also seriously considered [11–13] since they enable the compatibility with current semiconductor-based technologies.
One of the major issue that limits the implementation of a system with a large number of q-bits is the decoherence. A lot of fundamental studies and work on material are still to be done to achieve the quantum supremacy. In such circumstances, we address in this manuscript spin coherence of conduction electrons in two systems: electron gas in n-CdTe thin layers and indirect excitons in GaAs/(AlGa)As quantum wells.

Studies of indirect excitons (IX) spin dynamics were initiated soon after the claim of their macroscopic coherence [14–16]. Since then, many works dealt with spin diffusion [17, 18], spin relaxation [19–21] and polarisation pattern formation [22, 23]. The role of their spin properties in their condensation has also been pointed out in [24]. This work predicts that the IX ground state is optically inactive and, therefore, that an IX Bose-Einstein condensate should be dark. It has been experimentally confirmed in several works [25–27]. Photoluminescence is therefore not suited to study the IX

condensation. Knowing this, a pump-probe based methodology has been proposed to access to their spin and population dynamics [28]. Up to now, the experimental proof-of-concept of this suggestion has only been realised in a symmetric coupled quantum wells structure [29] that does not allow for the discernment of dark and bright excitons. In this regard, the first part of this work provides the study of an asymmetric CQW structure.

Furthermore, the study of the electron spin relaxation in semiconductors is still an active research field. Various spin relaxation mechanisms exist and compete, depending on the characteristics of the studied system. In n-GaAs, the electron spin relaxation is now well understood on a wide range of doping densities [30, 31]. The interplay between spin relaxation and spin diffusion is also understood [32]. Despite strong similarities between the two materials, the electron spin relaxation is much less known in n-CdTe. Here, we investigate electron spin dynamics using spin noise spectroscopy (SNS). Initially performed in atomic vapors [33, 34], this optical method has known major technical advances making it a powerful tool for spin dynamics in semiconductors [35, 36]. Since then, improving its abilities - including the possibility to address both spatial and temporal spin correlations - has received an ongoing attention. The second part of this work is dedicated to the study of the electron spin dynamics in n-CdTe with an innovative SNS-setup which can address spatio-temporal spin correlations.

The following of this manuscript is organised in five chapters. The first one is dedicated to introducing the basic physics underlying our discussion. Its first section is dedicated to optical spin orientation, spin relaxation mechanisms and optical tools for spin dynamics studies. The second section introduces spin noise spectroscopy (SNS), underlying its potential abilities. Its last section is devoted to excitons, introducing their proprieties and presenting the motivations of this work.
The second and the third chapters discuss original results obtained in SNS. Both the study of electron spin relaxation and spin diffusion in n-CdTe and the experimental development of a setup providing access to spatial correlation are covered.
The fourth chapter is dedicated to optical spectroscopy of IX in biased asymmetric CQW. It includes original results obtained by photoluminescence (PL) and pump-probe spectroscopy. Although non-conclusive in terms of dark state detection, they allow for the comparison of lifetime and spin relaxation time measured in PL and in time-resolved Kerr rotation. Then, a concluding chapter closes the manuscript bringing to light further opportunities.

Bibliography

[1] M Mitchell Waldrop. The chips are down for moore's law. *Nature News*, 530(7589):144, 2016. [(document)]

[2] Nicolas Gisin and Rob Thew. Quantum communication. *Nature photonics*, 1(3):165, 2007. [(document)]

[3] Ji-Gang Ren, Ping Xu, Hai-Lin Yong, Liang Zhang, Sheng-Kai Liao, Juan Yin, Wei-Yue Liu, Wen-Qi Cai, Meng Yang, Li Li, et al. Ground-to-satellite quantum teleportation. *Nature*, 549(7670):70, 2017. [(document)]

[4] Christian L Degen, F Reinhard, and P Cappellaro. Quantum sensing. *Reviews of modern physics*, 89(3):035002, 2017. [(document)]

[5] LA Lugiato, A Gatti, and E Brambilla. Quantum imaging. *Journal of Optics B: Quantum and semiclassical optics*, 4(3):S176, 2002. [(document)]

[6] Yanhua Shih. Quantum imaging. *IEEE Journal of Selected Topics in Quantum Electronics*, 13(4):1016–1030, 2007. [(document)]

[7] Immanuel Bloch, Jean Dalibard, and Sylvain Nascimbene. Quantum simulations with ultracold quantum gases. *Nature Physics*, 8(4):267, 2012. [(document)]

[8] Rainer Blatt and Christian F Roos. Quantum simulations with trapped ions. *Nature Physics*, 8(4):277, 2012. [(document)]

[9] Natalia G Berloff, Matteo Silva, Kirill Kalinin, Alexis Askitopoulos, Julian D Töpfer, Pasquale Cilibrizzi, Wolfgang Langbein, and Pavlos G Lagoudakis. Realizing the classical xy hamiltonian in polariton simulators. *Nature materials*, 16(11):1120, 2017. [(document)]

[10] John Clarke and Frank K Wilhelm. Superconducting quantum bits. *Nature*, 453(7198):1031, 2008. [(document)]

[11] MV Gurudev Dutt, L Childress, L Jiang, E Togan, J Maze, F Jelezko, AS Zibrov, PR Hemmer, and MD Lukin. Quantum register based on individual electronic and nuclear spin qubits in diamond. *Science*, 316(5829):1312–1316, 2007. [(document)]

[12] Hendrik Bluhm, Sandra Foletti, Izhar Neder, Mark Rudner, Diana Mahalu, Vladimir Umansky, and Amir Yacoby. Dephasing time of gaas electron-spin qubits coupled to a nuclear bath exceeding 200 μs. *Nature Physics*, 7(2):109, 2011. []

[13] DA Gangloff, Gabriel Éthier-Majcher, Constantin Lang, EV Denning, JH Bodey, DM Jackson, Edmund Clarke, Maxime Hugues, Claire Le Gall, and Mete Atatüre. Quantum interface of an electron and a nuclear ensemble. *Science*, 364(6435):62–66, 2019. [(document)]

[14] LV Butov, AC Gossard, and DS Chemla. Macroscopically ordered state in an exciton system. *Nature*, 418(6899):751, 2002. [(document)]

[15] LV Butov, CW Lai, AL Ivanov, AC Gossard, and DS Chemla. Towards bose-einstein condensation of excitons in potential traps. *Nature*, 417(6884):47, 2002. []

[16] D Snoke, S Denev, Y Liu, L Pfeiffer, and K West. Long-range transport in excitonic dark states in coupled quantum wells. *Nature*, 418(6899):754, 2002. [(document)]

[17] J. R. Leonard, Y. Y. Kuznetsova, Sen Yang, L. V. Butov, T. Ostatnický, A. Kavokin, and A. C. Gossard. Spin transport of excitons. *Nano Lett*, 9:4204–4208, 2009. [(document)]

[18] A Violante, R Hey, and P V Santos. Coherent transport and manipulation of spins in indirect-exciton nanostructures. *Phys. Rev. B*, 91(12):125302, March 2015. [(document)]

[19] K Kowalik-Seidl, X P Vögele, B N Rimpfl, S Manus, J P Kotthaus, D Schuh, W Wegscheider, and A W Holleitner. Long exciton spin relaxation in coupled quantum wells. *Appl. Phys. Lett.*, 97(1):011104, 2010. [(document)]

[20] Mussie Beian, Mathieu Alloing, Edmond Cambril, Carmen Gomez Carbonell, Johann Osmond, Aristide Lemaître, and François Dubin. Long-lived spin coherence of indirect excitons in GaAs coupled quantum wells. *EPL*, 110(2):27001–5, April 2015. []

[21] Ran Finkelstein, Kobi Cohen, Benoit Jouault, Ken West, Loren N Pfeiffer, Masha Vladimirova, and Ronen Rapaport. Transition from spin-orbit to hyperfine interaction dominated spin relaxation in a cold fluid of dipolar excitons. *Phys. Rev. B*, 96(8):085404, August 2017. [(document)]

[22] A. A. High, A. T. Hammack, J. R. Leonard, Sen Yang, L. V. Butov, T. Ostatnický, M. Vladimirova, A. V. Kavokin, T. C. H. Liew, K. L. Campman, and A. C. Gossard. Spin currents in a coherent exciton gas. *Phys. Rev. Lett.*, 110:246403, 2013. [(document)]

[23] DV Vishnevsky, H Flayac, AV Nalitov, DD Solnyshkov, NA Gippius, and G Malpuech. Skyrmion formation and optical spin-hall effect in an expanding coherent cloud of indirect excitons. *Physical review letters*, 110(24):246404, 2013. [(document)]

[24] Monique Combescot, Odile Betbeder-Matibet, and Roland Combescot. Bose-einstein condensation in semiconductors: The key role of dark excitons. *Physical review letters*, 99(17):176403, 2007. [(document)]

[25] Monique Combescot, Roland Combescot, Mathieu Alloing, and François Dubin. Optical signatures of a fully dark exciton condensate. *EPL (Europhysics Letters)*, 105(4):47011, 2014. [(document)]

[26] Mathieu Alloing, Mussie Beian, Maciej Lewenstein, David Fuster, Yolanda González, Luisa González, Roland Combescot, Monique Combescot, and François Dubin. Evidence for a bose-einstein condensate of excitons. *EPL (Europhysics Letters)*, 107(1):10012, 2014. []

[27] Mussie Beian, Mathieu Alloing, Romain Anankine, Edmond Cambril, Carmen Gomez Carbonell, Aristide Lemaître, and François Dubin. Spectroscopic signatures for the dark bose-einstein condensation of spatially indirect excitons. *EPL (Europhysics Letters)*, 119(3):37004, 2017. [(document)]

[28] AV Nalitov, Maria Vladimirova, AV Kavokin, LV Butov, and NA Gippius. Nonlinear optical probe of indirect excitons. *Physical Review B*, 89(15):155309, 2014. [(document)]

[29] Peristera Andreakou, Steeve Cronenberger, Denis Scalbert, A Nalitov, NA Gippius, AV Kavokin, Michal Nawrocki, JR Leonard, LV Butov, KL Campman, et al. Nonlinear optical spectroscopy of indirect excitons in coupled quantum wells. *Physical Review B*, 91(12):125437, 2015. [(document)]

[30] RI Dzhioev, KV Kavokin, VL Korenev, MV Lazarev, B Ya Meltser, MN Stepanova, BP Zakharchenya, D Gammon, and DS Katzer. Low-temperature spin relaxation in n-type gaas. *Physical Review B*, 66(24):245204, 2002. [(document)]

[31] VV Belykh, KV Kavokin, DR Yakovlev, and M Bayer. Electron charge and spin delocalization revealed in the optically probed longitudinal and transverse spin dynamics in n-gaas. *Physical Review B*, 96(24):241201, 2017. [(document)]

[32] Jan G Lonnemann, Eddy P Rugeramigabo, Michael Oestreich, and Jens Hübner. Closing the gap between spatial and spin dynamics of electrons at the metal-to-insulator transition. *Physical Review B*, 96(4):045201, 2017. [(document)]

[33] EB Aleksandrov and VS Zapasskii. Magnetic resonance in the faraday-rotation noise spectrum. *Zh. Eksp. Teor. Fiz*, 81:132–138, 1981. [(document)]

[34] SA Crooker, DG Rickel, AV Balatsky, and DL Smith. Spectroscopy of spontaneous spin noise as a probe of spin dynamics and magnetic resonance. *Nature*, 431(7004):49, 2004. [(document)]

[35] Michael Oestreich, M Römer, Rolf J Haug, and D Hägele. Spin noise spectroscopy in gaas. *Physical review letters*, 95(21):216603, 2005. [(document)]

[36] M Römer, J Hübner, and M Oestreich. Spin noise spectroscopy in semiconductors. *Review of Scientific Instruments*, 78(10):103903, 2007. [(document)]

Chapter 1

Main physical principles

The first chapter of this manuscript is dedicated to setting the scene of this work. The first part introduces the physics of spin systems in semiconductors. The following three key points are discussed: creation of a polarised carriers population, spin dynamics of such a population and optically detection of this polarisation. The second part is devoted to spin noise spectroscopy. Basic principles and historical development are first considered in order to highlight its major asset, its actual limitations and above all its potential improvement. Finally, the last part deals with exciton physics with a particular attention paid to the observation of their collective states.

1.1 Spin physics in semiconductors

The studies of the spin physics in semiconductors (SC) relies largely on concepts and methods deployed in the studies of atomic vapors and in magnetic resonance. The principles of optical orientation has been first developped in the fifties and the sixties, particularly by Kastler and Brossel. Then, it has been transposed into semiconductors by Lampel in 1968 [1] and by Parsons in 1969 [2]. Since then, this field has known a huge success and generates an ongoing interest fifty years later.
Of course, non optical techniques - such as transport or magnetic resonance method - have also been developed in order to study spin system and their dynamics in semiconductors. Because of the content of this work, this section provides a non exhaustive introduction to spin physics in semiconductors through the assumed narrow prism of optical method applied to zinc-blende structure semiconductors, such as many of III-V and II-VI.
Naturally, all the content of this section can be found in the two famous books [3] and [4] but also in great reviews such as [5–7], which all have been a source of inspiration

for this section and also for the rest of this manuscript.

1.1.1 Optical orientation

In semiconductors, the angular momentum conservation has an important direct consequence: photo-generated carriers can be polarised by light. Indeed, the angular momentum of the incident photon (± 1 depending on the helicity of the light) is shared between the created electron and hole. This distribution obeys the selection rules imposed by the band structure.

Band structure of cubic zinc-blende semiconductors

In cubic zinc-blende semiconductors, such as GaAs or CdTe which are of interest in this work, the band structure presents a direct gap and we will focus on the Γ-point. In $k = 0$, the dispersion relation is parabolic. The conduction band is two-fold degenerated due to the spin of electrons $S_e^z = \pm 1/2$ (the orbital angular momentum is $\mathbf{L} = 0$). Because its orbital momentum is $\mathbf{L} = 1$, the valence band is not described by the spin $\mathbf{S_e}$ anymore but by the total angular momentum $\mathbf{J} = \mathbf{S_e} + \mathbf{L}$. The $\mathbf{J} = 3/2$ band is four-fold degenerated while the $\mathbf{J} = 1/2$ is two-fold degenerated. They are separated by an energy Δ_{SO} due to spin-orbit coupling. This situation is depicted in figure 1.1(a).

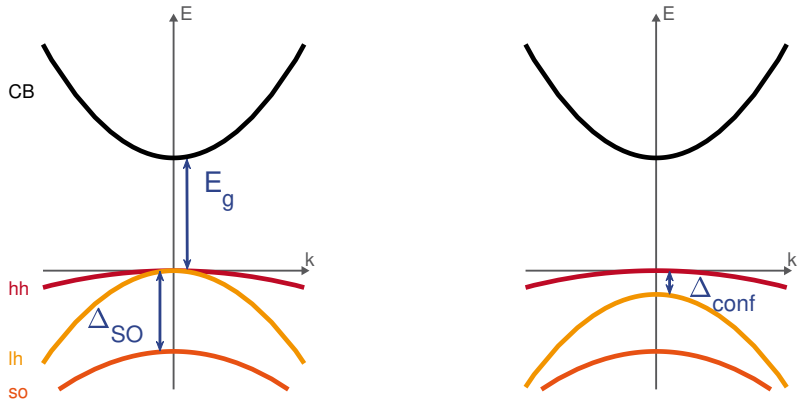

(a) bulk (b) quantum well

Figure 1.1: Schematic band structure of a cubic Zinc blende semiconductor close to the center of the Brillouin zone. Conduction band and valence band are separated by E_g. The valence band is composed of light hole band, heavy hole band and split-off band. While in bulk SC light and heavy hole bands are degenerated at $k = 0$, in quantum wells, the degeneracy is removed. In both cases, the split-off band is shifted by Δ_{SO}

Selection rules in cubic zinc-blende semiconductors

The selection rules for light absorption (the light energy is above the gap $E > E_g$) reflects the conservation of the angular momentum. For light circularly polarised along the z-axis, this leads to the variation $\Delta J^z = \pm 1$ where J^z is the $z-$component of $\mathbf{J}$. Allowed transitions are summarized in fig 1.2 with their respective probabilities. Transitions involving heavy holes (hh) are three times higher than transitions from light holes (lh).

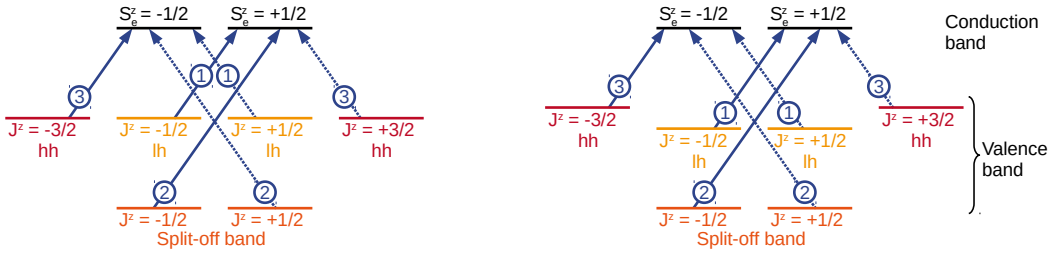

(a) Selection rules in bulk SC (b) Selection rules in quantum well

Figure 1.2: Selection rules at $k = 0$ for both σ^+ (solid lines) and σ^- (dotted lines) excitation in cubic Zinc blende semiconductors. Relative probabilities of each transition is represented by circles.

Let's define the degree of electron spin polarisation ρ_e by:

$$\rho_e = \frac{n_\uparrow^e - n_\downarrow^e}{n_\uparrow^e + n_\downarrow^e} \tag{1.1}$$

where $n_\uparrow^e$ and $n_\downarrow^e$ are the respective populations of electron with spin $S_e^z = +1/2$ and $S_e^z = -1/2$.

The maximal reachable degree of electron spin polarisation depends on the excitation energy E_{exc}. Indeed, if $E_{exc} > E_g + \Delta_{SO}$, transitions can involve the split-off band. Probabilities of transitions involving this band are two times higher than probabilities of transitions involving light holes. All transitions are involved and under σ^+ excitation, we obtain:

$$\rho_e = \frac{1+2-3}{1+2+3} = 0 \tag{1.2}$$

which means that no polarisation is possible.

In contrast, if $E_g + \Delta_{SO} > E_{exc} > E_g$, only transitions from light and heavy holes are involved in the population of $n_\uparrow$ and $n_\downarrow$. In case of σ^+ incident light, it leads to a polarisation of 50%:

$$\rho_e = \frac{1-3}{1+3} = -0.5 \tag{1.3}$$

Here, the sign is due to the fact that a σ^+ polarisation increases the $n_\downarrow$ population.

In quantum wells (QW), the degeneracy of heavy and light holes band vanishes. The difference of the confinement potential for each sort of holes introduces a splitting energy Δ_{conf} between the two corresponding bands (see figure 1.1(b)). In this case, it is possible to reach a maximal degree of spin polarisation of 100% by selective excitation on heavy hole band. In this case, $E_g + \Delta_{conf} > E_{exc} > E_g$ and the degree of electron polarisation is:

$$\rho_e = \frac{0-3}{0+3} = -1 \tag{1.4}$$

A similar reasoning is also valid for holes. However, semiconductors are either n-doped or p-doped and photo-generated carriers will recombine with majority carriers (see section 1.1.3).

* *
*

Considerations developed in this section bring us to a central question in spin physics: after its creation, what happens to a non-equilibrium spin population? Of course, it comes back to its thermodynamic equilibrium but how does it take place? The next section will introduce the main mechanisms allowing this relaxation.

1.1.2 Spin dynamics

An arbitrary spin state $|\mathbf{S}\rangle$ can be described by its spherical coordinates onto a Bloch sphere. For a given quantization axis, the North and South poles of this sphere correspond to the "up" and "down" eigenstates $|\uparrow\rangle$ and $|\downarrow\rangle$. Polar θ and azimuthal Φ angles characterise the state $|\mathbf{S}\rangle$ as a combination of the two eigenstates:

$$|\mathbf{S}\rangle = \cos(\frac{\theta}{2})\,|\uparrow\rangle + e^{i\Phi}\sin(\frac{\theta}{2})\,|\downarrow\rangle \tag{1.5}$$

If the two eigenstates are split (for instance in the presence of a magnetic field which defines the quantization axis), the spin will precess. That means θ remains constant while Φ linearly increases with time. This time evolution is characterised by the spin splitting between the two eigenstates $\hbar\omega_L = \mu_B g B$ and defines the Larmor frequency of the precession.
In this current form, the time evolution of the spin state does not take into account any interaction with the environment and provides for a precession for an indefinitely time. However, spin states are never isolated and different interactions lead to the decay of the average spin $\mathcal{S}$. This decay is described by the following phenomenological Bloch

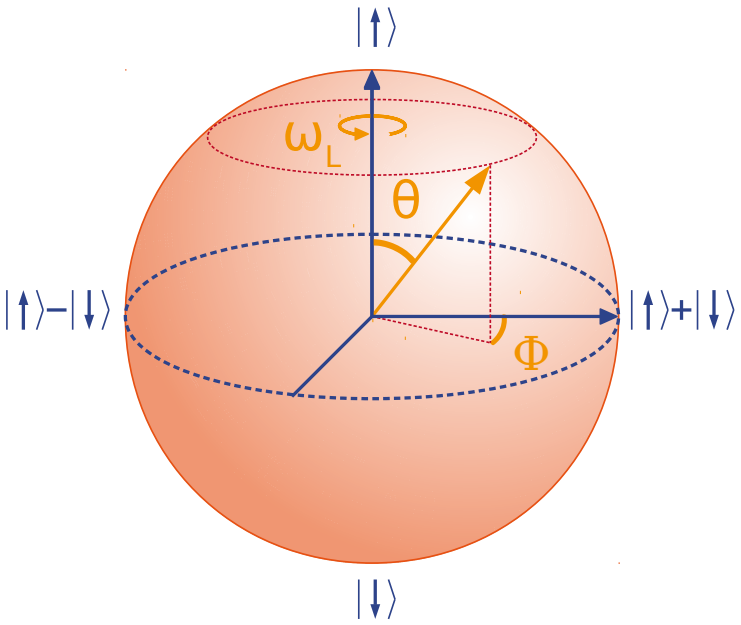

Figure 1.3: Larmor precession of an arbitrary spin state visualised on the Bloch sphere. The magnetic field is vertical. The two eigenstates $|\uparrow\rangle$ and $|\downarrow\rangle$ are respectively at North and South pole and two other remarkable states are shown to browse the Bloch sphere.

equations:

$$\frac{d\mathcal{S}_x}{dt} = \gamma(\vec{\mathcal{S}} \wedge \vec{B})_x - \frac{1}{T_2}\mathcal{S}_x \tag{1.6}$$

$$\frac{d\mathcal{S}_y}{dt} = \gamma(\vec{\mathcal{S}} \wedge \vec{B})_y - \frac{1}{T_2}\mathcal{S}_y \tag{1.7}$$

$$\frac{d\mathcal{S}_z}{dt} = \gamma(\vec{\mathcal{S}} \wedge \vec{B})_z - \frac{1}{T_1}(\mathcal{S}_z - \mathcal{S}_{eq}) \tag{1.8}$$

where $\gamma = \mu_B g/\hbar$ is the gyromagnetic ratio and $\mathcal{S}_eq$ is the equilibrium value of the average spin, oriented along the magnetc field (here along the z-axis). Here, the spin relaxation occurs with two different characteristic times T_1 and T_2 corresponding to the longitudinal and the transverse spin relaxation respectively.

In this framework, the spin relaxation time T_1 corresponds to the thermalisation with the lattice (the spin system reaches its thermal equilibrium population and transfers energy to the lattice) and is also called the spin-lattice relaxation time. T_2 is the coherence time after which the phase of the precession of the transverse spin component is lost.

In what follows, unless otherwise noted, we will consider $T_1 \approx T_2$ (this assumption is true for low magnetic fields) and we will talk about the spin relaxation time τ_s.

Origin of spin relaxation

A wide variety of spin interactions could take place in semiconductors: spin-orbit interaction, hyperfine interaction (if some nuclei hold a spin), electron-hole or electron-electron exchange interactions, s-d or p-d exchange interactions with magnetic impurities or interactions with phonons. Each of them could provide a relaxation channel for the spin system. In the end, the polarisation of the spin population decays to zero with a characteristic time τ_s referred to as the spin relaxation time.
Spin relaxation mechanisms can be understood as the result of a fluctuating effective magnetic field. For moving spin carriers, fluctuations originate from scattering events (with phonons, impurities or between carriers) while for localised spin carriers, they are due to fluctuations of the environment. It is customary to use the classical random walk framework [8] and to describe this randomly fluctuating field using two parameters: its correlation time τ_c and the rms value of the spin precession frequency Ω. The former is the characteristic time during which the field remains unchanged. The latter depends on the amplitude of the effective field. In such a fluctuating field, the spin observes a precession at Ω around one direction. After a typical time τ_c, the effective field changes randomly: the axis of the spin precession and its frequency change as well.
Depending on the value of these two parameters, relaxation phenomena act differently. We could envisage two distinct cases corresponding to two limit values of $\delta\phi = \Omega\tau_c$ which is the angle of rotation performed during τ_c.

If $\Omega\tau_c \ll 1$, the interruption of the spin precession occurs so frequently that $\delta\phi$ is small. During a time t, in other words after t/τ_c steps, the total squared precession angle is $(\Omega\tau_c)^2 \times t/\tau_c$. Defining the spin relaxation time τ_s as the time after which this squared angle is of the order of 1 [8], we obtain:

$$\frac{1}{\tau_s} \sim \Omega^2\tau_c \tag{1.9}$$

This situation is referred to as « motional narrowing » because a short correlation time leads to a long spin relaxation time [9].

In the opposite limit case, if $\Omega\tau_c \gg 1$, the spin can achieve one (or more) entire precession around each value of the effective field. During τ_c, the projection of the spin on the random field is conserved but its transverse projection is lost. The projection of the spin on its initial direction decreases at each step. This process recurs and the initial direction is destroyed [10]. In this case, the angle $\delta\phi$ no longer

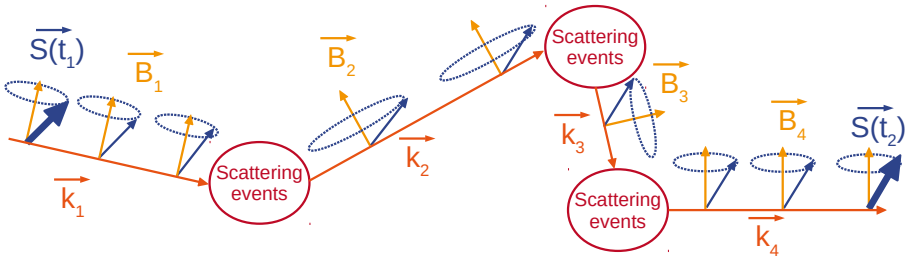

(a) $\Omega\tau_C \ll 1$

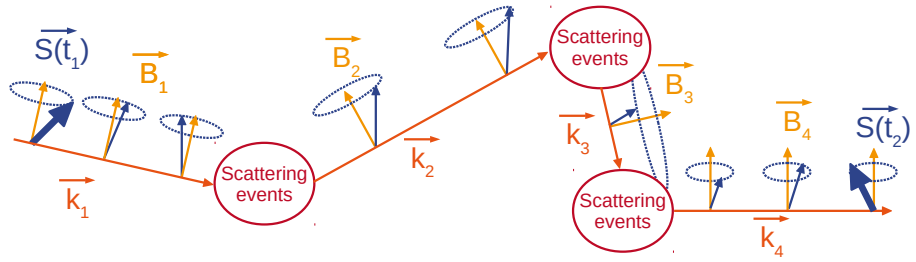

(b) $\Omega\tau_C \gg 1$

Figure 1.4: Precession of a spin (blue arrows) in a randomly fluctuating field (yellow arrows). Here, the field is k-dependent and its changes are due to any scattering event leading to a variation of both its orientation and its amplitude. Two different cases corresponding to two different ratios between the correlation time of the field τ_c and the precession period are represented. In case (a) (top panel), the spin only realises very weak rotations which are averagade due to the short τ_c time. The final orientation is similar to the initial orientation (see bold arrows). This situation is referred as to motional narrowing regime. In case (b) (bottom panel), the spin can realise a valuable fraction of a complete rotation and the initial orientation is lost.

depends on τ_c which leads to:

$$\tau_s \sim \tau_c \tag{1.10}$$

Depending on the system of interest, different spin relaxation mechanism - such as Elliot-Yafet [11], Bir-Aronov-Pikus [12, 13], Dyakonov-Perel [14] - could dominate the spin relaxation. Some of them have been pointed out for decades while other have been understood more recently [15]. In what follows, most relevant for further discussions mechanisms are introduced.

Main relaxation mechanisms

Dyakonov-Perel mechanism In SC crystals with no inversion symmetry, the spin-orbit coupling leads to a splitting of the energy bands:

$$E_{k,\uparrow} = E_{-k,\downarrow} \neq E_{k,\downarrow} \tag{1.11}$$

This splitting could have two origins. In non-centrosymmetric semiconductors (such as III-V or II-VI), the Bulk Inversion Asymmetry (BIA) leads to such a lack of symmetry. This splitting is known as the Dresselhaus splitting. This lack of symmetry could also come from Structure Inversion Asymmetry (SIA) - asymmetry of the confining potential due to heterostructure or electrical field - and it is known as Rashba-Sheka splitting. In 2D systems, the BIA term depends on the growth direction. Both the BIA and the SIA contributions could be involved and the relaxation is usually anisotropic, that means spin relaxation depends on the relative orientation of the spin and the growth axis.
Therefore, an additional **k**-dependent term in the electron hamiltonian appears in the form of:

$$H_{SO} = \hbar\, \mathbf{\Omega_{SO}}(\mathbf{k}).\mathbf{S_e} \tag{1.12}$$

Since this effective field depends on **k**, it changes randomly for each collision event and its correlation time is the momentum relaxation time τ_P (due to impurities, phonon, or electron-electron interaction).
Usually, the characteristic parameters of the field lead to the situation of motional narrowing and the spin relaxation time is described by:

$$\frac{1}{{\tau_s}^{DP}} \sim \Omega_{SO}^2 \tau_c \tag{1.13}$$

Hyperfine interaction with nuclear spin system In material with non-zero spin nuclei, magnetic interaction may couple the electronic spin system (ESS) and the nuclear spin system (NSS). This Fermi contact interaction is known as hyperfine interaction (HI) and can be expressed as [4]:

$$H_{HI} = A\, \mathbf{I} \cdot \mathbf{S_e} \tag{1.14}$$

where $\mathbf{I}$ and $\mathbf{S_e}$ are the nuclear and the electron spin. The hyperfine constant A being dependant on the square of the electron wave function at the nucleus location, this interaction will have a major play for localised or confined electrons.

A polarisation of the ESS may lead to a polarisation of the NSS. In this case, electrons undergo an effective magnetic field from the NSS which is called the Overhauser field. This field acts in turn on the dynamic of the ESS: electron spins precess in this random nuclear field providing a channel spin relaxation. The nuclear spin also experiences the effective magnetic field of electrons which is called the Knight field.

Two different origins of the electron spin relaxation due to the HI can be considered. For localised electrons with long correlation time, fluctuations of the Overhauser field lead to spin relaxation.
Inversely, if electrons hop from on nuclear site to another with a typical correlation time shorter than their precession period, the precession of nuclear spins can be considered as frozen. The spin relaxation occurs therefore in the motional narrowing and the spin relaxation time is given by [16] :

$$\frac{1}{{\tau_s}^{HF}} \sim \Omega_N^2 \tau_c \tag{1.15}$$

where τ_c is the typical amount of time the electron spends on a nuclear site and Ω_N is the precession frequency in the Overhauser field.

Anisotropic exchange interaction In semiconductors, the spin-orbit interaction gives rise to an anisotropic part in the exchange interaction hamiltonian. This antisymetric part is called the Dzyaloshinskii-Moriya and is well known for magnetic ions. Kavokin pointed out this interaction will provide a relaxation mechanism for pair of localised electrons [17]. When a spin tunnels from one donnor site to an other, it undergoes a finite rotation θ_{AEI} which contributes to relaxation. Hopping of electrons also leads to a similar relaxation [18], [19]. Finally, the spin relaxation time is:

$${\tau_s}^{AEI} \sim \Omega_{AEI}^2 \tau_c \tag{1.16}$$

where $\Omega_{AEI}^2 = \frac{3}{2}\frac{1}{\theta_{AEI}^2}$ and θ_{AEI} is the rotation angle of the spin due to hopping between donors.

Competition between different mechanisms

The electron spin relaxation in n-doped GaAs at low temperature can be explained on the whole range of doping densities with these three different mechanisms.
Dzhioev *et al.* [20] have performed systematic experimental study of spin relaxation for different doping levels. Spin relaxation time are obtained by Hanle depolarisation of photoluminescence (see section 1.1.3) obtained in this work are shown in figure 1.5. At low doping density, electrons are localised and the hyperfine interaction is the predominant channel of relaxation. At high doping level, this is the Dyakonov-Perel which dominates. Dzhioev *et al.* have also shown that the anisotropic interaction prevails in an intermediate doping level which corresponds to the end of the insulator regime. Whatever the predominant relaxation mechanism, the spin relaxation time

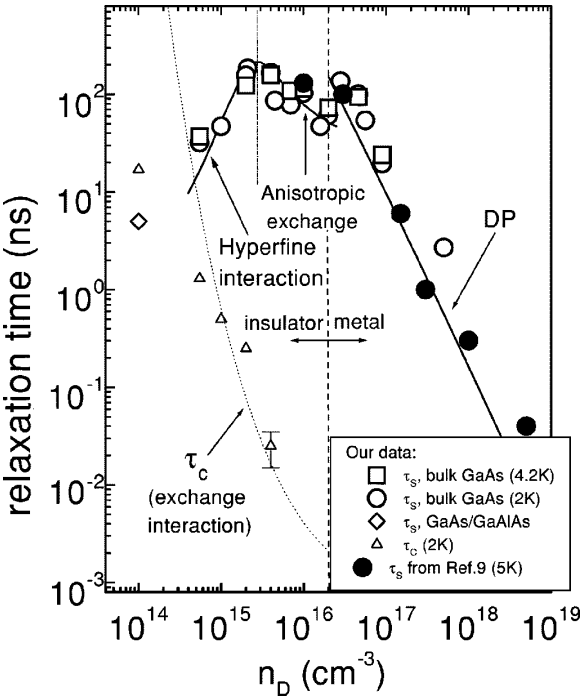

Figure 1.5: Spin relaxation time for different doping levels. Solid lines show expected values for hyperfine interaction (left region, low densities), anisotropic exchange interaction (intermediate densities) and Dyakonov-Perel (right region, metallic regime). Figure taken from [20].

is given by:

$$\frac{1}{\tau_s} = \frac{1}{{\tau_s}^{SO}} + \frac{1}{{\tau_s}^{HF}} + \frac{1}{{\tau_s}^{AE}}$$

This work was a milestone in the comprehension of spin dynamics in n-GaAs which is now well understood. More recent works address both optical measurements of spin relaxation time and tranport measurement [21, 22] providing a deeper understanding of electron spin dynamics in n-GaAs, connecting spin relaxation and spatial dynamics of electrons.

* *
*

The next section is dedicated to the optical tools allowing to monitor the spin dynamics in semiconductors, that means to measure spin relaxation time or g-factor in different conditions.

1.1.3 Optical way to access spin dynamics

From the beginning of spin physics studies (in atomic vapors), optical orientation based techniques have been widely used to understand the spin dynamics. Historically, first methods relied on continuous excitation. Then, in the 1990's, time-resolved

measurements - provided by the recent arrival of ultrafast pulses excitation - allowed to directly observe the spin dynamics. This section intends to introduce the working principle of these techniques in order to bring to light the opportunities they offer and to understand their limitations. The first part will deal with polar-resolved photoluminescence measurements and the second one will deal with dispersive measurements based on the Faraday rotation.

Polarisation of the photoluminescence

Photo-generated carriers have finite lifetime and recombine after a typical recombination time τ_r. This recombination is accompanied by the emission of a photon. The angular momentum being conserved during the process, a spin polarisation gives rise to a polarised photoluminescence. Thus, measuring the polarisation of the photoluminescence (PL) provides a direct access to spin polarisation in a system. Here, we define the degree of polarisation of the photoluminescence $\mathcal{P}_c$ by:

$$\mathcal{P}_c = \frac{I_{\sigma^+} - I_{\sigma^-}}{I_{\sigma^+} + I_{\sigma^-}} \tag{1.17}$$

where I_{σ^+} and I_{σ^-} are respectively the intensity of the σ^+ and σ^- component of the photoluminescence.

Continuous wave measurement Let's consider the ideal case of a σ^+ excitation of a bulk SC at an energy somewhere above the band gap but below $E_g + \Delta_{SO}$. Thus, we deal with heavy and light holes only and the created - the maximum reachable - electron spin polarisation is $\rho_e = -0.5$.
If each created carrier recombines with its co-created partner, the emitted light will be fully polarised σ^+. However, during the holes and electrons lifetime their spin relax and the PL polarisation is affected.
In many cases - and more specifically in systems we study in this work - hole spin relaxation occurs very fast [23]. In what follows we therefore consider the recombination of a polarised electron population with non polarised holes. We will derive the expected polarisation of the spectrally integrated PL in the absence and in the presence of electron spin relaxation.

The created electron spin polarisation $\rho_e = -0.5$ means that one half of the electron population have a spin $S_e^z = -1/2$ and one half is unpolarised. Thus, we can denote the two subpopulation of spins $S_e^z = +1/2$ and $S_e^z = -1/2$ by $n_\uparrow^e = 0.25\ n^e$ and $n_\downarrow^e = 0.75\ n^e$ where n^e is the total density of created electrons.

Following the selection rules (see figure 1.2), the total emitted photons n_σ are given by:

$$n_\sigma = \frac{1}{4}\left(\frac{1}{4}\, n_{\sigma^+} + \frac{3}{4}\, n_{\sigma^-}\right) + \frac{3}{4}\left(\frac{3}{4}\, n_{\sigma^+} + \frac{1}{4}\, n_{\sigma^-}\right) = \frac{10}{16}\, n_{\sigma^+} + \frac{6}{16}\, n_{\sigma^-} \tag{1.18}$$

where the first term corresponds to the emitted photons due to $S_e^z = +1/2$ electrons and the second term corresponds to the emitted photons due to $S_e^z = -1/2$ electrons. Here $n_{\sigma^\pm}$ denotes the $\sigma_\pm$ polarised photons.
In the linear regime, the intensity of the two circular components of the emitted light being proportional to $n_{\sigma^\pm}$, we obtain:

$$\mathcal{P}_c^{max} = \frac{I_{\sigma^+} - I_{\sigma^-}}{I_{\sigma^+} + I_{\sigma^-}} = \frac{10-6}{10+6} = 0.25 \tag{1.19}$$

which is the highest reachable value of PL polarisation in this case (excitation energy lower than $E_g + \Delta_{SO}$, bulk SC and instantaneous hole spin relaxation).
Up to now, we have been considering that all the free carriers are photocreated. n-doped semiconductors are also interesting. In this case, the ratio of photocreated carriers and resident carriers ζ is given by the power of the excitation energy. Following the same reasoning gives directly a degree of PL polarisation of :

$$\mathcal{P}_c^{max} = 0.25\frac{\zeta}{1+\zeta} \tag{1.20}$$

Electron spin relaxation strongly affect the measured PL polarisation. If the recombination time is much lower than the spin relaxation time, the PL polarisation remains $\mathcal{P}_c^{max}$. In the opposite limit case, if electron spin relaxation is much faster than recombination, the PL polarisation will be null. The competition between the two phenomena leads to a PL polarisation given by:

$$\mathcal{P}_c = \frac{\mathcal{P}_c^{max}}{1 + \tau_r/\tau_s} \tag{1.21}$$

Thus, measuring the PL polarisation under continuous excitation provides the ratio τ_r/τ_s and the extraction of τ_s requires the knowledge of τ_r.
In n-doped semiconductors, the ratio of photocreated carriers and resident carriers ζ is not always easy to evaluate. It is therefore necessary to perform measurement at different excitation power P_{exc} in order to extract the linear dependence of $\mathcal{P}_c$ with P_{exc} ($\mathcal{P}_c^{max} \propto P_{exc}$). However, this implies to assume that both τ_r and τ_s do not vary with P_{exc}.
The next paragraph describes a way to unravel τ_r and τ_s using a transverse magnetic

field .

Hanle effect The precession of the average electron spin density $\vec{\mathcal{S}}$ in the presence of a transverse magnetic field $\vec{B}$ is described by the following equation:

$$\frac{d\vec{\mathcal{S}}}{dt} = \gamma(\vec{\mathcal{S}} \wedge \vec{B}) - \frac{\vec{\mathcal{S}}}{\tau_s} - \frac{\vec{\mathcal{S}}}{\tau_r} + \frac{\vec{\mathcal{S}}_0}{\tau_r} \tag{1.22}$$

which includes the precession, the spin relaxation, the recombination and the photogeneration. Here, $\vec{\mathcal{S}}_0 = \mathcal{S}_0\vec{e_z}$ is the initial average electron spin density (without relaxation) and is along the optical axis which is now fixed along the z-axis and $\gamma = \mu_B g/\hbar$ is the gyromagnetic ratio.
In the absence of magnetic field, this differential equation leads to a steady state with null x and y-components and a non null z-component described by:

$$\mathcal{S}_z(B=0) = \frac{\mathcal{S}_0}{1+\tau_r/\tau_s} \tag{1.23}$$

which matches with equation 1.21.
In the presence of a transverse magnetic field with respect to the optical axis, the equation 1.22 leads to an equilibrium state along the z-axis described by:

$$\mathcal{S}_z(B) = \frac{1}{1+(\gamma B\tau^*)^2}\,\mathcal{S}_z(B=0) \tag{1.24}$$

where it is convenient to define

$$\frac{1}{\tau^*} = \frac{1}{\tau_s} + \frac{1}{\tau_r} \tag{1.25}$$

Figure 1.6 shows the Lorentzian evolution of $\mathcal{S}_z$ with the intensity of a transverse magnetic field. It is also applicable to the degree of electron spin polarisation and to the degree of polarisation of the photoluminescence. Such a variation is characterised by two parameters: its height and its width. Thus, Hanle measurement allows to unravel both τ_s and τ_r.

Time-resolved measurement The arrival of ultrafast pulses laser has allowed to follow carriers spin dynamics directly in time domain. Indeed, the synchronisation between laser pulses and a streak camera enables to monitor the decay of the photoluminescence. Such a time-resolved photoluminescence may be polar-resolved providing not only τ_r but also τ_s.
This technique does not require any application of a magnetic field. However, the

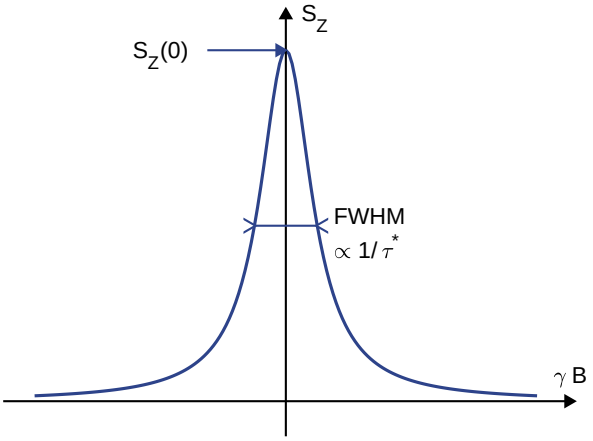

Figure 1.6: Spin projection along the optical axis for different transverse magnetic field. The curve has a Lorentzian shape caracterised by two parameters: its width and its intesity from wich one can extract both recombination time τ_r and spin relaxation time τ_s. This evolution applies to polarisation of the photoluminescence or to the Faraday rotation (see section 1.1.3).

time resolution allows the direct observation of the precession mentioned in equation 1.22 and study spin dynamics under magnetic field is of great interest.
Being created, a spin polarisation leads to a magnetisation of the crystal. The effect of this magnetisation on an incident light is also a widely used method to study the spin dynamics.

Dispersive measurements

The contribution of an optical transition to the dielectric response function is given by:

$$\epsilon_{res}(\omega) \propto \frac{1}{\omega^2 - \omega_0^2 - i\Gamma\omega} \tag{1.26}$$

where ω_0 is the resonance frequency of the transition and Γ describes its broadening. In the case of a spin-selective transition (see section 1.1.1), an imbalance in the spin subpopulations leads to different amplitude of this contribution - and accordingly to a difference between the complex refractive index ($n = \sqrt{\epsilon}$) - for the two circular polarisations. Close to the resonance, the complex refractive index for the two circular polarisations can be written as follows:

$$n_\pm(\omega) = n'_\pm(\omega) - in''_\pm(\omega) \tag{1.27}$$

where n' and n'' denote respectively the real and the imaginary part of n corresponding to the refractive index and the absorption. Here, indexes $\pm$ denote the two circular polarisations.

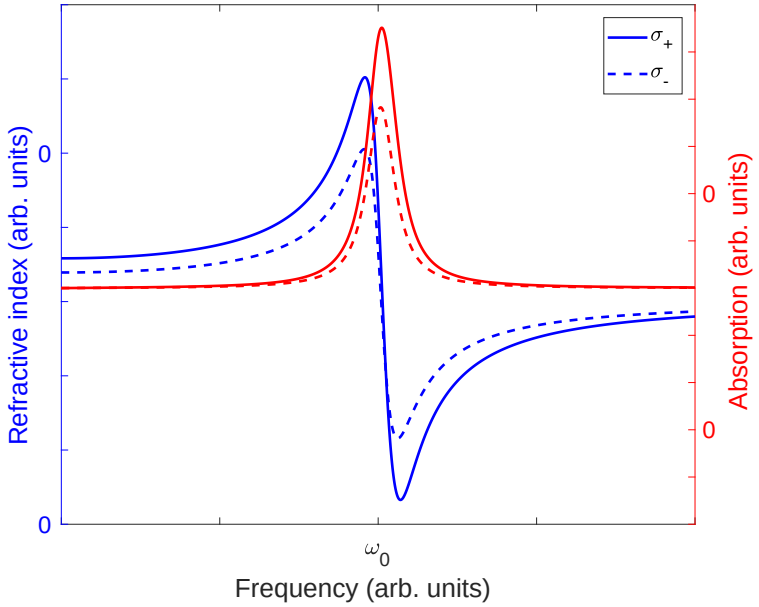

Figure 1.7: Refractive index (blue lines) and absorption coefficient (red lines) for the two different circular polarisations (denoted respectively by solid and dashed lines). We can see that $\Delta n'(\omega)$ decays slower than $\Delta ni'(\omega)$ when the detuning increase.

Figure 1.7 shows the two parts of the complex refractive index for the two circular polarisations in the case of a spin dependent transition. These differences of amplitude for both n' and n'' offer an opportunity to probe the spin system.
Let's consider an incident wave propagating along the z-axis and linearly polarised along the x-axis. At a given incident frequency ω, the difference of refractive index $\Delta n'(\omega) = n'_+(\omega) - n'_-(\omega)$ leads to a phase difference between its two circularly polarised components. In this manner, the linearly polarised incident wave undergoes a rotation of its polarisation plane which is known as the Faraday rotation (FR). This rotation is given by:

$$\theta_{FR}(\omega) = \pi l/\lambda \Delta n'(\omega) \tag{1.28}$$

where l is the length travelled and λ is the laser wavelength.
The difference of absorption $\Delta n''(\omega) = n''_+(\omega) - n''_+(\omega)$ is also detectable through an amplitude difference of the two circular components. In this case, the incident beam acquires an induced ellipticity revealing the spin subpopulations.
From figure 1.7 we directly see that the absorption effect is stronger that the dispersive effect at low detuning, while the situation is reversed for higher detuning. It is important to note that this understanding of dispersive measurement remains true provided that we have a negligible Zeeman splitting of the transition energies regarding the linewidth of the transition (here we have made the assumption than

$\omega_{0+} = \omega_{0)}$).
Finally, it is important to note that an equivalent effect occurs in reflection. It is called the magneto-optic Kerr effect and allows to study non-transparent samples. Once again, the effect of a transverse magnetic field provides a way to access spin relaxation time by Hanle effect.

Pump-probe technique It is also possible to optically generate a polarised spin system and then to detect the induced Faraday (or ellipticity) effect. The idea consists in using a circularly polarised laser beam as a pump and on probing the spin subpopulations unbalance with a weaker linearly polarised laser beam. Introducing a delay between the pump and the probe provides a direct access to the spin dynamics of the system. Such a pump-probe technique relies on non linear optics and the pump have to be resonant with an optical transition. The probe however can both have the same energy than the pump or be detuned from the pump providing a spectroscopic method.

In the presence of an external magnetic field, this method provides precious informations about the dynamics of a spin system. Depending on the orientation of the field, we can consider two configurations.
In the Faraday configuration, the applied magnetic field is along the optical axis and therefore. In this case, we expect a monotonous decay of the longitudinal component of the magnetisation governed by T_1 (see section 1.1.2).
In the Voigt configuration, the applied field is perpendicular to the optical axis. Here, we can monitor the precession of the magnetisation and its relaxation governed by T_2.
The situation requires our attention. The experimentally observed value of this decay has two different contributions, a homogeneous one and an inhomogeneous one. The inhomogeneous contribution T_2^{inh} is due to spatial and/or temporal variation of precession frequencies and is given by:

$$T_2^{inh} = \frac{\hbar}{\Delta g \mu_B B} \tag{1.29}$$

where Δg is the spread of the g-factor and is due to g-factor inhomogeneities. This g-factor spread implies slightly different Larmor frequencies. Interference between each of these oscillations is less and less constructive (see figure 1.8) leading to a measured decay $T_2{}^*$ (called dephasing time) lower than the homogeneous value T_2:

$$\frac{1}{T_2{}^*} = \frac{1}{T_2} + \frac{1}{T_2^{inh}} \tag{1.30}$$

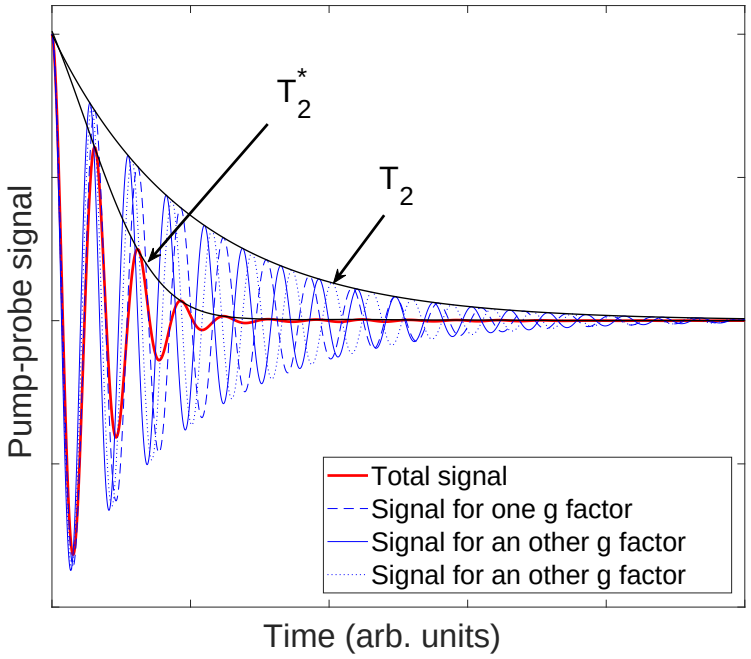

Figure 1.8: Evidence of the effect of a spread of g-factor on the measured decay time. Normalised signals from three different spin carriers with the same coherence time T_2 but slightly different arbitrary g-factors are shown in blue (solid, dashed and dotted lines). At the beginning, they are in phase but they become progressively more and more dephased. Normalised total signal for a large number of spin carriers with the same decoherence time but a normally distributed random g-factor around an arbitrary mean value is represented in red solid line. Their respective envelope are shown in black. We clearly observe a much faster decay for the total signal due to destructive interference between the different contributons.

These two last equations describe a linear dependence between $\frac{1}{T_2{}^*}$ and the magnetic field. Therefore, the two contributions can be unravelled: varying B allows one to extract T_2 from the intercept and Δg from the slope. The inhomogeneous contribution being reversible, it can be removed by spin echo techniques [24] or by spin mode locking [25].

Finally, Faraday rotation can also encode the stochastic spontaneous fluctuation of a spin system. This is the the basic principle of spin noise spectroscopy which is introduced in the next section.

* *
*

All the optical techniques introduced in this section rely on optical orientation, that is on carrying out the electron spin system out of equilibrium and observe its relaxation. The perturbation due to excitation light or to the presence of magnetic

field might be avoided thanks to the spin noise spectroscopy which plays a central role in this work. The next section will introduce this powerful technique.

1.2 Spin noise spectroscopy

Despite appearances, noise is not just a source of annoyance in measurements. Quite the contrary, it is a great source of informations on the studied system. Indeed, it is well known that a system in its equilibrium state experiences fluctuations which are directly linked to its dynamics. This relation between spontaneous fluctuations around the equilibrium state and the way the system relaxes from non equilibrium to equilibrium state is described by the so-called fluctuation-dissipation theorem [26–28]. This principle has been used in a wide range of different fields in physics [29]: diffusion and Brownian motion, light absorption and thermal radiation or even the stiffness of a spring. Practically speaking, it provides a non-perturbative access to the dynamics of many different systems. A famous example is the Johnson-Nyquist noise [30, 31] allowing the measurement of the electrical resistance of a sample without any application of current.

Application of this principle to spin systems and their magnetisation fluctuation has led to the emergence of a technique known as spin noise spectroscopy. In the last fifteen years, this method has known a rapid development due to its broad range of applications including in semiconductors.
The first paragraph of this section will introduce the basics of spin noise spectroscopy. Then, the second one will present the evolution of this technique through two closely related questions: the historical experimental development of spin noise setup and the successively reached physical spin systems. Finally, we will interrogate one non-used potentiality of this subtle technique.

1.2.1 Principles

This paragraph is devoted to introducing the working principles of spin noise spectroscopy (SNS). A simple way to explain how it works starts from the Faraday rotation and is the topic of the first part of this paragraph. However, another point of view allows one to understand the full range of possibilities offered by spin noise spectroscopy. This perspective is addressed in the second part of this paragraph.

Spontaneous fluctuations of a spin system detected via Faraday rotation

Let's consider a paramagnetic system, with a population of N non interacting spin carriers such as electrons. At thermal equilibrium and in the absence of magnetic field, the two subpopulations corresponding to the two spin states $n^e_\uparrow$ and $n^e_\downarrow$ are equal and the spin polarisation $\rho_e = \frac{n^e_\uparrow - n^e_\downarrow}{n^e_\uparrow + n^e_\downarrow}$ is null. Because N has a finite value, this is true on average in time but the standard deviation of these populations leads to a standard deviation of ρ_e.
The basic idea of spin noise spectroscopy is the following: thanks to the Faraday rotation (see section 1.1.3), spontaneous spin fluctuations can be detected through the fluctuations of the polarisation plane of a laser beam. Indeed, the instantaneous non-zero spin polarisation leads to a circular birefringence coming from the difference in the absorption of σ_+ and σ_- circularly polarised light. For a linearly polarised light beam, this birefringence results in a rotation of its polarisation plane known as Faraday rotation. This rotation being proportional to ρ_e, stochastic fluctuations of the spin system can be detected via the fluctuations of the polarisation plane of a linearly polarised laser beam passing across the studied sample.
All the information about the dynamics of the system is therefore contained in its auto-correlation function $g(t)$ which is defined as:

$$g(t) = \langle \mathcal{S}_z(t)\mathcal{S}_z(0)\rangle \tag{1.31}$$

where $\mathcal{S}_z(t)$ is the projection of the instantaneous average spin along the optical axis (here, the z-axis).
The Wiener-Khintchine theorem links the auto-correlation and the noise power spectrum $C_{SN}(\omega)$ as follows:

$$C_{SN}(\omega) = 2\int_0^\infty cos(\omega t)g(t)dt \tag{1.32}$$

Technically, the basic setup consists in probing the sample with a linearly polarised laser beam and in analysing the polarisation of the transmitted beam (see figure 1.9). Intensity fluctuations of its cross-polarised component contains both the spin fluctuations and the laser intensity fluctuations. This undesirable noise affecting equally the two polarisation components, they are separated with a polarised beam splitter and sent to a balanced detector. This optical bridge converts the polarisation fluctuation into intensity fluctuation and removes the laser intensity noise. Finally, the electrical signal is frequency analysed in order to obtain its power spectrum. It

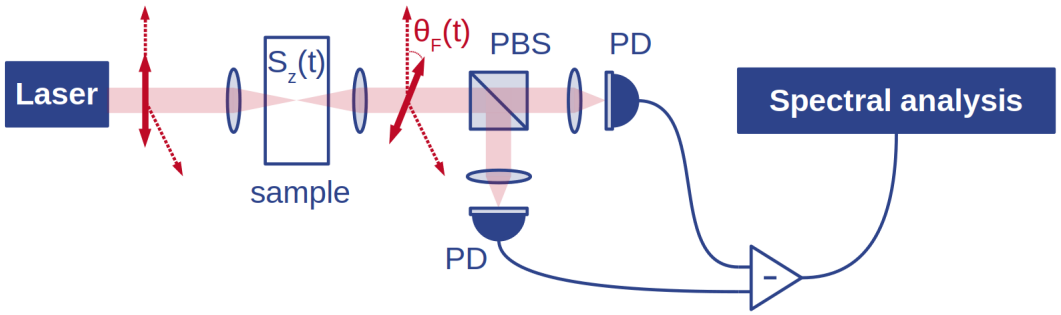

Figure 1.9: Basic spin noise spectroscopy setup. A linearly polarised laser beam passes through the sample and undergoes a very small instantaneous Faraday rotation $\theta_F(t)$ which is proportional to $\mathcal{S}_z(t)$ the stochastic magnetisation of the sample along the optical axis. This rotation is detected with a optical bridge which consists in a polarised beam splitter (PBS) and two photodetectors (PD). Then, the electrical signal is analysed in frequency domain.

is then normalised in order to remove other noise sources coming from the detection/digitalisation scheme.

Depending on the orientation of the magnetic field, we can consider two configurations (see section 1.1.3) which lead to different shapes of the spin noise power spectrum.
In the Faraday configuration, the magnetic field being along the optical axis, the $\mathcal{S}_z(t)$ component decays exponentially with a relaxation time T_1. It therefore leads to:

$$g(t) \propto e^{-t/T_1} \tag{1.33}$$

and the resulting noise power spectrum is given by:

$$C_{SN}(\omega) \propto \frac{1}{\omega^2 + \dfrac{1}{T_1^2}} \tag{1.34}$$

which is a zero-centred Lorentzian peak whose width is inversely proportional to the longitudinal time T_1.
In the Voigt configuration, the magnetic field being transverse to the optical axis, the $\mathcal{S}_z(t)$ component also decays exponentially but with a relaxation time T_2. In this case, the precession of the magnetisation yields to a modulation of this decay at the Larmor frequency ω_L. It leads to:

$$g(t) \propto \cos(\omega_L t) e^{-t/T_2} \tag{1.35}$$

and the noise power spectrum is given by:

$$C_{SN}(\omega) \propto \frac{1}{(\omega-\omega_L)^2+\frac{1}{T_2^2}} + \frac{1}{(\omega+\omega_L)^2+\frac{1}{T_2^2}} \tag{1.36}$$

which corresponds to two Lorentzian peaks spread on both side of the frequency domain, centred on the Larmor frequency (which can be far away from zero at high magnetic field) and for which the width is inversely proportional to the transverse time T_2.

It is important to note that while we detect only positive frequencies, we have to pay attention to the low magnetic field case: if the width of the peak is comparable to the Larmor frequency, the negative peak goes beyond the negative side and the two peaks overlap.

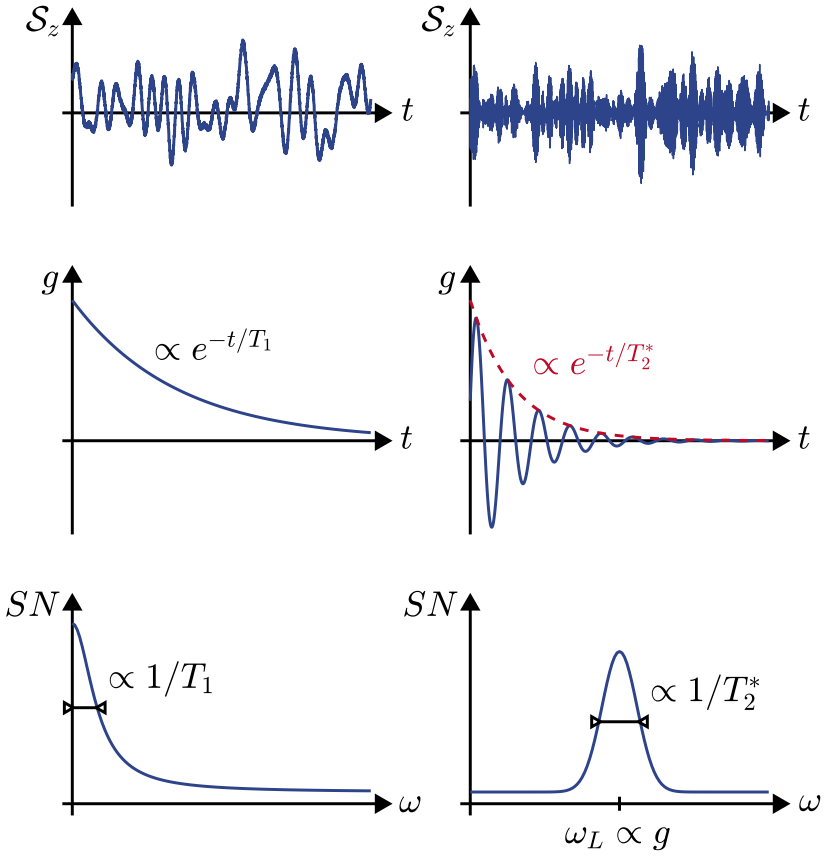

Figure 1.10: Origin of the spin noise signal for Faraday (left panels) and Voigt (right panels) configurations. Upper panels show time-fluctuations of the z-projection of the spin average. Middle panels shows corresponding autocorrelation functions. Lower panels shows corresponding power spectrum.

In Voigt configuration, as it has been pointed out in section 1.1.3, measurements are sensitive to disorder or any reasons leading to slightly different precession frequencies

such as g-factor or magnetic field inhomogeneity due to nuclear field for example. The electron spin experiences a fluctuating effective magnetic field as it moves through the sample. Depending whether the correlation time of this effective field is long or short compared to their precession period in this field, the spin resonance line will be homogeneously broadened or not. Homogeneous broadening leads to a Lorentzian line with a width providing the T_2 time while the inhomogeneous case leads to a Gaussian line with a width providing T_2^*.
In the case of a tilted magnetic field, the noise power spectrum consists in three peaks (one zero centred and two centred on $\pm\omega_L$).

Finally, from the position and the width of these peaks, we obtain precious informations about the spin dynamics in the studied system such as T_1 and T_2 times or the Landé g-factor from the value of the Larmor frequency (see figure 1.10).

The definition of the correlator function in equation 1.31, directly leads us to consider some other informations contained in spontaneous fluctuations. Indeed, we can consider cross-correlations between two spin systems [32, 33] or higher order correlators [34, 35] for example. These powerful tools have been used in several works which gives a sense to the possibilities offered by the spin noise spectroscopy.
An other consideration offers new perspectives to improve these possibilities. It relies on the intimate link between Faraday rotation and spin-flip Raman scattering which is introduced in what follows.

Relation with spin-flip Raman scattering

This paragraph intends to elucidate the reason to see the Faraday rotation as a direct consequence of the scattering of the probe light by the sample.

A material media receiving an electromagnetic wave re-emits this wave in all the directions. This is due to the fluctuations of the dielectric permittivity which lead to an induced polarisation. This induced polarisation emits in turn the scattered field. This phenomenon is governed by the propagation equation of the electric field of an electromagnetic wave:

$$\Delta\vec{E} = \mu_0 \frac{\partial^2 \vec{D}}{\partial t^2} \tag{1.37}$$

where $\vec{D} = \epsilon_0\epsilon_r\vec{E} = \epsilon_0\vec{E} + \vec{P}$ is the electric displacement where ϵ_r is the relative electric permittivity and $\vec{P}$ is the electric polarisation.
Considering the incident wave implies a modification $\delta\epsilon_r$ of the relative electric

permittivity we can write $\epsilon_r = \widetilde{\epsilon_r} + \delta\epsilon_r$.
The total electric displacement is

$$\vec{D}^{tot} = \vec{D}_i + \vec{D}_s = \epsilon_0\epsilon_r(\vec{E}_i + \vec{E}_s) = \epsilon_0\widetilde{\epsilon_r}\vec{E}_i + \epsilon_0\delta\epsilon_r\vec{E}_i + \epsilon_0\widetilde{\epsilon_r}\vec{E}_s + \epsilon_0\delta\epsilon_r\vec{E}_s \tag{1.38}$$

where indexes i and s denote respectively the incident and the scattered electric field. The last term can be neglected and we can identify the electric displacement related to the scattered field $\vec{D}_s = \epsilon_0\delta\epsilon_r\vec{E}_i + \epsilon_0\widetilde{\epsilon_r}\vec{E}_s$. Thus, equation 1.37 for the scattered field is:

$$\Delta\vec{E}_s - \frac{\widetilde{\epsilon_r}}{c^2}\frac{\partial^2\vec{E}_s}{\partial t^2} = \frac{\delta\epsilon_r}{c^2}\frac{\partial^2\vec{E}_i}{\partial t^2} \tag{1.39}$$

The left hand term is the free propagation of $\vec{E}_s$ and the right hand term corresponds to the source term.
Different contributions to $\delta\epsilon_r$ leads to both Rayleigh, Brillouin and Raman scattering. Rayleigh and Brillouin scattering have the same frequency ν_i than the incident field while the Raman scattering contribution have two frequencies $\nu_i \pm \nu_R$ where ν_R is the frequency modulation of the dielectric permittivity. In conventional Raman scattering, this frequency corresponds to phonons but Raman scattering is also sensitive to spin waves.

In the case of a gyrotropic media undergoing a magnetisation $\vec{M}$, the relative electric permittivity ϵ_r is a second rank tensor because the electric polarisation is given by [36] :

$$\vec{P} = \epsilon_0\chi_e\vec{E} + i\vec{E} \wedge \bar{G}\vec{M} \tag{1.40}$$

where $\chi_e = \epsilon_r - 1$ is the electric susceptibility and $\bar{G}$ is a second rank tensor. Here, we can associate the precession of spins to a modulation of the magnetisation at the Larmor frequency. This is the origin of the so called spin-flip Raman scattering (SFRS).

Finally, we can link the SFRS to the Faraday rotation considering the two following situations (see figure 1.2.1). Let's first consider an incident wave linearly polarised along the x-axis $\vec{E}_i = E_0e^{-i\omega t}\vec{e}_x$, and a magnetic field $\vec{H}$ along the x-axis. The z-axis is the optical axis and we consider an isotropic medium in which G

becomes a scalar. Then, the induced electric polarisation is given by :

$$\vec{P} = iG \begin{pmatrix} E_0 e^{(-i\omega t)} \\ 0 \\ 0 \end{pmatrix} \wedge \begin{pmatrix} M_{//} \\ M_\perp \cos(\omega_L t) \\ M_\perp \sin(\omega_L t) \end{pmatrix} = iG \begin{pmatrix} 0 \\ \frac{-1}{2} E_0 M_\perp (e^{-i(\omega+\omega_L)t} - e^{-i(\omega-\omega_L)t}) \\ \frac{i}{2} E_0 M_\perp (e^{-i(\omega+\omega_L)t} + e^{-i(\omega-\omega_L)t}) \end{pmatrix} \tag{1.41}$$

where the magnetisation $\vec{M}$ is divided in two parts: $M_{//}$ is directed along the magnetic field and $M_\perp$ is the rotating orthogonal projection of $\vec{M}$. Stokes and anti-Stokes contribution of the SFRS correspond to the y component (cross polarised with respect to $\vec{E}_i$).

Let's now consider an incident wave linearly polarised along the x-axis $\vec{E}_i = E_0 e^{-i\omega t}\vec{e}_x$, and a magnetic field $\vec{H}$ along the optical z-axis. The induced electric polarisation is given by :

$$\vec{P} = iG \begin{pmatrix} E_0 e^{-i\omega t} \\ 0 \\ 0 \end{pmatrix} \wedge \begin{pmatrix} M_\perp \cos(\omega_L t) \\ M_\perp \sin(\omega_L t) \\ M_{//} \end{pmatrix} = iG \begin{pmatrix} 0 \\ -E_0 M_{//} e^{-i\omega t} \\ E_0 M_\perp \sin(\omega_L t) e^{-i\omega t} \end{pmatrix} \tag{1.42}$$

Here, the y component is cross polarised with respect to $\vec{E}_i$ and has the same frequency. It corresponds to the forward Rayleigh scattering and is the origin of the so called Faraday rotation.

Thus, the intimate link between Faraday rotation and SFRS, highlighted in [37–39], becomes clear. This understanding offers an opportunity to have two interpretations of the signal origin in SNS. The Faraday rotation fluctuation can also be understood as interferences of the incident wave and the fluctuating scattered one. This has been pointed out from the very beginning of the SN by Gorbovitsky and Perel [40] as early as 1983. However, while SNS differs from SFRS only by the order of arrangement of the spectrum analyzer and photodetector [41], SNS presents some advantages compared to SFRS. It has actually demonstrated the ability to probe the inner structure of a resonance [42, 43] and the aptitude to be spatially resolved, the signal increasing with the inverse of the probed volum [44]. The deep understanding of this link have given rise to different extensions of the basic SNS setup (see chapter 3).

* *
*

The following paragraph will introduce the state of the art of SNS in order to figure out both the importance of practical aspects in SNS and the major role played by this not so new interpretation in the past and present development of SNS.

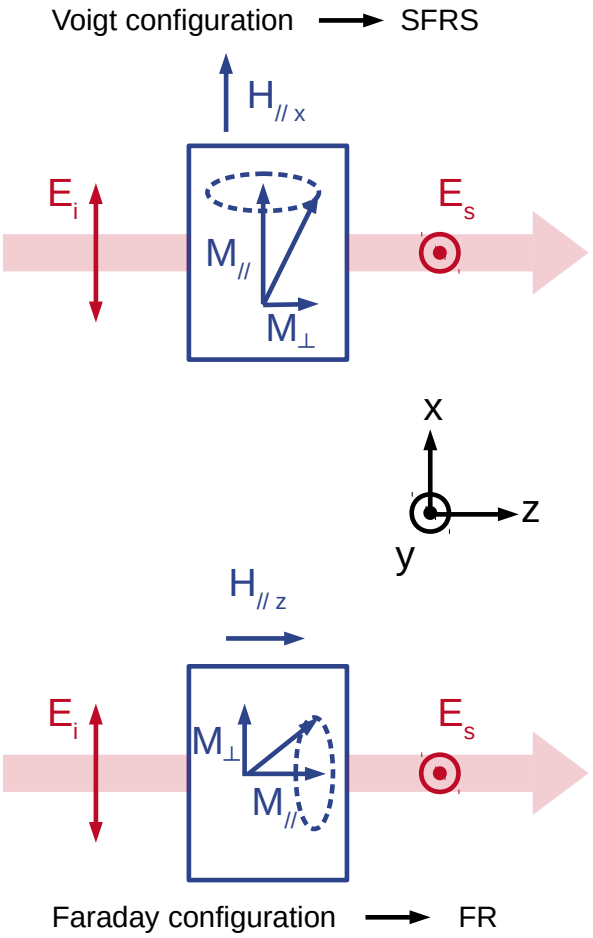

Figure 1.11: Spin-flip Raman scattering (top panel) and Faraday rotation (bottom panel) correspond to the same physical effect for different orientation of the applied magnetic field.

1.2.2 State of the art

During the last fifteen years, SNS has evolved very quickly and its applications are more and more abundant. This development is driven by the necessity to enhance the sensitivity and the bandwidth of this powerful technique in order to reach new physical systems. Thus, technical evolution of SNS and its applications are particularly connected.

Technical evolution

First Faraday rotation noise measurement The first measurement of spin noise (SN) has been realised in 1981 [45]. In this work, Aleksandrov and Zapasskii have recorded the magnetic resonance of sodium vapor in the noise spectrum of its transverse magnetisation. While these fluctuations was already reached through the Faraday rotation (using a balance polarimeter), the noise was recorded for only one

frequency (which was adjusted to enhance the signal) and it was the magnetic field which varied in order to observe the resonance.

Rise of spin noise spectroscopy An important milestone has been achieevd by Crooker *et al.* in 2004 [46]. In this work, the signal from the balanced detector is directly sent to a sweeping spectrum analyser, providing the observation of noise spectrum in a wide range of frequencies. In 2007, Römer *et al.* [47] reported the use of fast Fourier transformation analyser. While sweeping spectrum analyser accesses to a very restricted frequencies range at a time, FFT analyser performs the high rate digitalisation of the signal and provides a real time FFT calculation on the full frequencies range. In the same way a Fourier transform spectrometer records all wavelengths at the same time while a scanning monochromator selects only one wavelength, an FFT analyser offers a substantial time saving, hence a significant gain of sensitivity.

Improvement of the bandwidth Because of the characteristics of low-noise balanced detectors and acquisition cards, the SNS is usually restricted to low frequencies. An extented SNS setup has been proposed in [48] taking advantage of pulsed-laser to improve the bandwidth. A first implementation of such a broadband setup have been performed in [49] where a stroboscopic method is implemented, allowing measurements centred at more than 3.5 GHz in a range of 70 MHz. In this work, Müller *et al.* also argue the possibility to reach the THz range with a 1 GHz detectable line width. This method has also been implemented in [50] with two phase-locked lasers with a bandwidth of 60 GHz.
Finally, an other method have been implemented in [51]. In this work, the scanning temporal ultrafast delay [52] allows one to reach a bandwidth of several tenth of GHz but with a poor spectral resolution.

Homo/heterodyning In 2016, Cronenberger and Scalbert [53] have implemented a cw-laser based SNS setup using optical heterodyning. A continuous laser beam (with a frequency f_0) is split into a probe and an auxiliary beam which can possibly have a stable relative phase. This auxiliary beam is sent through a Mach-Zender electro-optic modulator (EOM) in order to create two new frequency components at $f_0 \pm f$ where f is the frequency of the EOM. Then, it is sent to an actively stabilised Fabry-Perot, allowing the selection of the central peak (homodyne configuration) or one of the two satellite peaks (heterodyne configuration). After all these modifications, the resulting beam acts as a local oscillator (LO). It is finally recombined with the light from the sample and they interfere onto the detector.

This setup not only improves the bandwidth up to several GHz but also presents precious technical advantages. First of all, shifting the signal to f allows the elimination of low frequency noise and thus the observation of the signal at very low frequencies. Furthermore, the signal-to-noise ratio of the detector is usually better at not so low incident light power. Because the LO does not pass through the sample, this limitation can be overcame by increasing the power ratio between LO and probe in favour of the LO.
Finally, this work highlighted the fact that conventional SNS corresponds to the interference of the scattered light (from Rayleigh diffusion) with the incident light, as it has been seen in paragraph 1.2.1. It allows one to understand that the second interfering field is not required to pass through the sample. The conventional configuration is therefore renamed self-homodyne configuration to distinguish it from homodyne (LO with the same frequency but not passing through the sample) or heterodyne (LO with a different frequency and not passing through the sample) configurations. The homodyne configuration has been used in recent works [54, 55] in order to increase the sensitivity of SNS.

Further abilities of SNS Eventually, trickier setup have promoted SNS beyond the usual opportunities offered by linear optics. Changing the wavelength of the probe allows one to obtain insights about the intrinsic structure of an inhomogeneous broadened transition [42]. Higher order correlator has also been under investigation in several works [34, 56].
Two beams arrangement have been also proposed and implemented. Using two different probes with two slightly different wavelengths allows one to determine the homogeneous width of a transition [43]. In the case of a multi species spin system, this also provides the determination of spin cross-correlation between different spin systems [32]. Finally, introducing a spatial distance between two beams at the same energy has been suggested to provide information about spin transport [57]. An other approach had also been proposed: a two beams arrangement with different incident angles, thus different wave vectors, should offer an access to spatial fluctuations [58, 59]. However, until the beginning of this work, no implementation of such a setup have been demonstrated.

Applications of SNS: from atomic vapors to semiconductors

Thanks to this variety of setup, application of SNS have covered an increasingly wide domain. SN has been firstly investigated in atomic vapors such as Sodium [45] or Rubidium and Potassium [46]. The first success of applying SNS in semiconductors

stems from the work of Oestreich *et al.* [60] in which electron spins are studied in bulk GaAs. Progressively, SNS has been applied in low dimensional systems such as quantum wells [61] or quantum dots [62]. Fluctuations of a single hole have even been detected in reference [63].
SN has also been used to probe paramagnetic impurities such as manganese ions embedded in CdTe [64], polariton [65, 66] and effective fields such as Stark optic [67] or Overhauser field [68, 69].

1.2.3 Further extension of SNS

Conservation of the total momentum in the Raman scattering process allows us to probe excitations of the medium with a given wave vector by selecting the wave vector of the scattered light. Considering the link between Faraday Rotation and SFRS leads naturally to the following question: how can we reach such precious informations with SNS?
Of course it implies to proceed to the interference of the incident light with scattered light out of the optical axis. This seems to be difficult because interferences are possible only at the same wave vector. However, using a local oscillator (deployed for instance in hetero/homodyning setup) should allow generating such interferences.

This idea has been pursued by Kozlov *et al.* and it has been understood that a SNS setup sensitive to the wave vector will probe not only temporal correlation but also spatial correlation of the spin system [58, 59]. Hence, the generalised susceptibility and thus the diffusion of the spin system are reachable. It has also been predicted that the diffusion will broaden the SNS signal. However, no experimental realisation of such a setup has ever been reported and was a distant goal in our team at the beginning of this work.
A further idea strengthened our motivation to elaborate more on this analogy between SFRS and SNS: Raman scattering offers a particular configuration which provides precious informations about the two subpopulations of a spin system. It consists in detecting light orthogonally scattered with respect to the optical axis. Depending on the magnetic field configuration, Stokes and anti-Stokes peak intensities will reveal the distribution between two different subpopulations in the spin system.

* *
*

An important part of this work is devoted to study indirect exciton and it has been showed that only non linear optical methods will be able to unravel the behaviour of their dark and bright states. Then, it is only natural, albeit lofty, to consider

the use of spin noise spectroscopy for their study. The next - and last - part of this introductory chapter is therefore devoted to exciton physics.

1.3 Excitons and their collective states

The last section of this introduction is devoted to excitons. We discuss their ability to form collective states. Their essential features are introduced in order to lay out the origin of these states and main issues in their observation. Then, the historical background and the state-of-the-art is provided. Finally, we focus on dipolar excitons in GaAs coupled quantum-wells, highlighting the encountered issues and the proposed solutions.

1.3.1 Theoretical background about excitons

Generalities

In a semiconductor, the absorption of a photon whose energy is above the band-gap is accompanied by the creation of an electron-hole pair: an electron from the valence band is promoted to the conduction band and leaves a lack called a hole. This hole is a quasi-particle characterised by its effective mass and a positive elementary charge e. Electrical charges of these two photo-created particles being opposite, the electron and the hole attract each other and may form a hydrogen-like bound state called an exciton which could be characterised by a Bohr radius and a biding energy [70, 71]. Depending on their size, two types of excitons can be distinguished: Frenkel excitons have a small Bohr radius with respect to lattice constant whereas Wannier excitons have a Bohr radius much higher than the lattice constant. In inorganic semiconductors, excitons are typically Wannier-excitons. It is convenient to describe exciton as a quasi-particle characterised by its effective mass M, its wave vector $\vec{K}$ and its reduced mass μ_X being defined as follows:

$$M = m_e + m_h \tag{1.43}$$

$$\vec{K} = \vec{k_e} + \vec{k_h} \tag{1.44}$$

$$\mu_X = \frac{m_e m_h}{m_e + m_h} \tag{1.45}$$

where m_e, m_h, $\vec{k_e}$ and $\vec{k_h}$ are the respective effective mass and the wave vector of the electron and the hole forming the exciton. It can be shown that the exciton energy can be expressed as:

$$E_X = E_g + \frac{\hbar^2 K^2}{2M} - E_b \tag{1.46}$$

The two former terms represent the band-gap energy and the kinetic energy of the electron-hole pair. The latter, E_b, is the exciton binding energy, usually denoted $E_b = Ry^*/n^2$ (where n is an integer greater than or equal to one) in reference to the hydrogen atom textbook case. The difference with the hydrogen atom - the mass and the dielectric background - leads to the following expression:

$$Ry^* = \frac{\hbar^2}{2\mu_X a_0^2} \tag{1.47}$$

Here again, the reference to the hydrogen atom is resounding, allowing the definition of the exciton Bohr radius a_0 defined by:

$$a_0 = \frac{\epsilon_b \hbar^2}{e^2 \mu_X} \tag{1.48}$$

An exciton could be seen as an elementary electrical excitation of the semiconductor. Because the semiconductor must return in its ground state, exciton has - in contrast with the hydrogen atom - a finite lifetime.

Effect of confinement In quantum wells, the confinement strongly affects the energy of exciton. Both the electron and the hole acquire a confinement energy E_c defined by:

$$E_c^{e,h} = \frac{\hbar^2 n^2 \pi^2}{2 m_{e,h} L^2} \tag{1.49}$$

where L is the width of the well and $m_{e,h}$ is the effective mass of the involved particle. Confinement also lifts the degeneracy between light and heavy holes. The energy of hh-based exciton is lower than lh-based excitons.
The binding energy is also affected by the confinement. In the ideal 2D limit case of an infinite barrier of zero thickness, this term tends to $E_b \to \frac{Ry^*}{(n-\frac{1}{2})^2}$ leading to the enhancement of the binding energy by up a factor four for $n = 1$.
In other cases, the calculation of confined exciton energies is more complicated, especially under an electrical field. An accurate calculation of the ground and excited states in coupled quantum wells is presented in [72].

Life cycle of excitons The life cycle of an exciton consists in three stages. First, it is created by an electrical or optical excitation by promoting an electron from the valence band to the conduction band. In this work, it is a result of the absorption of a photon either resonant or not. Depending on its kinetic energy, the exciton can be localised or mobile. In the second case, its motion is straight-lined and punctuated by scattering events (collision with phonons, impurities, free carriers or

between excitons). Non-elastic scattering allows for the dissipation of the exciton energy which can reach its lowest energy state. Finally, the electron and the hole recombine. In high quality samples, non-radiative recombination can be neglected and the recombination is accompanied by a photon emission. This whirlwind life is very short, and is characterised by the exciton lifetime which strongly depends on the overlap of the electron and the hole wavefunctions. In GaAs quantum wells, this time is in the order of tens of ps [73, 74], much shorter than in bulk GaAs [75].

Spin properties

Spin properties of exciton depends on its constituents. hh-excitons being composed of an electron with $S_e^z = \pm 1/2$ and a hole with $S_h^z = \pm 3/2$, their fine structure presents four states with $S_e^z = \pm 1$ or $S_{exc}^z = \pm 2$. Due to the conservation of the angular momentum, in dipolar approximation, only excitons with $S_{exc}^z = \pm 1$ can interact with photons, thus are optically active. They are referred to as bright excitons while excitons with $S_{exc}^z = \pm 2$ are referred to as dark excitons.
Figure 1.12 presents different pathways for the exciton to change its spin.

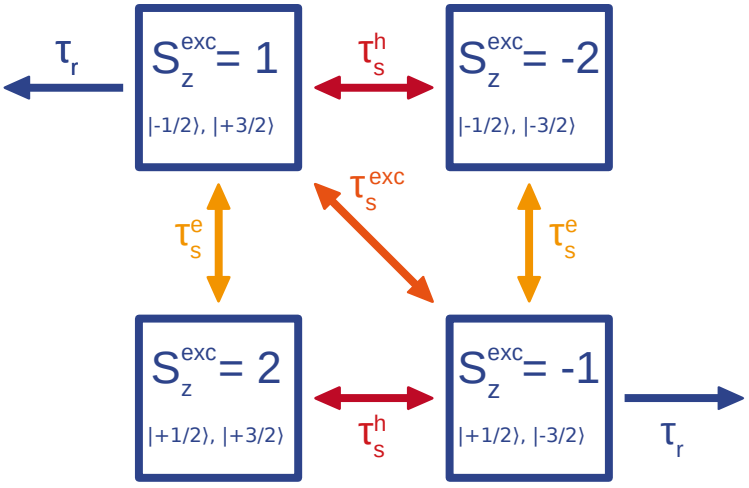

Figure 1.12: The four different exciton states (denoted S_{exc}^z). Notations $|\pm 1/2>$, $|\pm 3/2>$ spell out the spin state of the electron and the hole in each cases. The different spin relaxation mechanisms within an exciton are represented by double arrows. Radiative recombination of bright states is represented by blue arrows.

The spin-state of the exciton may change either due to a spin flip of the electron, a spin flip of the hole or a spin flip of the exciton as a whole, that means a simultaneous spin flip of both the electron and the hole. Each of these mechanisms is characterised by a time denoted as τ_s^e, τ_s^h and τ_s^{exc} respectively.
The spin flip of the electron changes the exciton spin from $S_{exc}^z = \pm 1$ states to

$S^z_{exc} = \pm 2$ states (and vice versa) while the spin flip of the hole changes the exciton spin from $S^z_{exc} = \pm 1$ to $S^z_{exc} = \mp 2$ (and vice versa). These mechanims are discussed in section 1.1.2.

A spin flip of the whole exciton could also occur, between the two bright states. Here, the fluctuating effective magnetic field originates from the long range exchange interaction between the electron and the hole. This field depends on the wave vector $\vec{K}$ of the exciton center of mass. As in the case of DP, these fluctuations gives rise to a spin relaxation mechanism of the type of motional narrowing. Thus, the spin relaxation time is given by:

$$\frac{1}{{\tau_s}^{exc}} \sim \Omega^2_{LT}\tau_c \tag{1.50}$$

where the correlation time of the field τ_c is the scattering time and Ω_{LT} is the precession angular frequency in the effective field (see below). This mechanism was discorvered by Maille, Andrada e Silva and Sham and has been theoretically and experimentally studied in [76] and [73] .

The exchange interaction energy is difficult to calculate and contains two contributions denoted as direct and exchange integral and given by:

$$D_{1,2} = \int \phi_1(r_e, r_h)\frac{e^2}{\epsilon_b \mid r_e - r_h \mid}\phi_2(r_e, r_h)dr_e dr_h \tag{1.51}$$

$$E_{1,2} = \int \phi_1(r_e, r_h)\frac{e^2}{\epsilon_b \mid r_e - r_h \mid}\phi_2(r_h, r_e)dr_e dr_h \tag{1.52}$$

where ϵ_b is the dielectric constant and ϕ_i $i = 1, 2$ is the exciton wave function in a state i (given by the wave vector, the electron and hole masses, the relative position of electron and hole) and r_e, r_h are the position of electron and hole.

Calculation of these integrals have been perfomed in [76]. The result can be represented as the sum of two contributions corresponding to a short range and a long range term. The short range term introduces a splitting Δ_0 between bright and dark states. It does not depend on $\vec{K}$.

The long range term results in a splitting between two exciton states referred to as longitudinal and transverse states. These states correspond respectively to component of $\vec{K}$ which is parallel and perpendicular to the electric dipole of the exciton. Thus, this splitting Δ_{LT} depends on the wave vector of the exciton and we have:

$$\Omega_{LT}(\vec{K}) = \Delta_{LT}(\vec{K})/\hbar \tag{1.53}$$

When the exchange interaction is strong [77, 78], this is the whole exciton spin which precesses and the Maille, Andrada e Silva and Sham mechanism dominate over individual electron or hole relaxation. In the opposite case ($\tau_{exc} >> \tau_e, \tau_h$), electron

and hole spins precess independently. Holes undergo very fast DP relaxation so that the longest time is τ_e which is governed either by spin-orbit or hyperfine interaction. This will be in particular the case for indirect excitons (see section 1.3.1) for which the overlap of electron and hole is weak and thus, the relaxation channel provided by the Maille, Andrada e Silva and Sham mechanism is wiped out.

Bosonic nature of exciton and collective states

As we have seen in the previous paragraph, the total angular momentum of excitons has an integer value. Thus, excitons are composite bosons and are expected to demonstrate collective states including the so-called Bose-Einstein condensation [79]. This paragraph will briefly introduce this quantum state of matter and then specifies its main features in the cases of excitons and spatially indirect excitons (IX).

Bose-Einstein condensation Particles with an integer spin are bosons and obey the Bose-Einstein statistics which gives the probability for a particle to have an energy E at a given temperature T. This statistics is described as:

$$f_{BE}(E,T) = \frac{1}{\exp(\frac{E-\mu}{k_B T}) - 1} \tag{1.54}$$

where μ is the chemical potential and k_B is the Boltzmann constant. This quantity allows one to link the number of bosons in the system N to the density of states $g(E)$ that is $g(E)dE$ is the number of state with an energy between E and $E + dE$. This relation can be written as:

$$N = \int_0^\infty g(E) f_{BE}(E) dE \tag{1.55}$$

Here, $E - \mu$ has to be positive or null to ensure the positivity of the probability. Considering the 3D case ($g(E) \propto V\sqrt{(E)}$ where V is the volume of the system) and low temperatures (μ tends to 0), this integral leads to:

$$N \propto V \left(\frac{m k_B T}{2\pi\hbar^2} \right)^{3/2} \tag{1.56}$$

which matches a critical density $n_C = N/V$ to a fixed value T. If more particles are present, they have to be in the ground state: this is the Bose-Einstein condensation (BEC). The repartition of particles is not described by the Bose-Einstein satistics

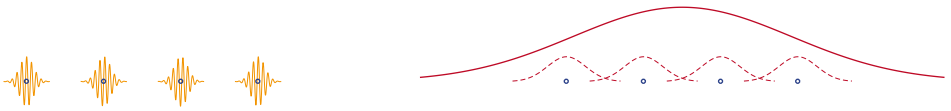

(a) $T > T_C$ (b) $T < T_C$

Figure 1.13: Qualitative approach of Bose-Einstein condensation. Above T_C (left panel), the de Broglie wavelength is shorter than typical inter-particle distance while it is longer below T_C. In this situation (left panel), the whole assembly of particles experiences a collective state and could be described by a unique wave function.

anymore and we can writen:

$$N = N_0 + \int_0^\infty g(E) f_{BE}(E) dE \tag{1.57}$$

where N_0 is the number of particles which are in the lowest energy state independently to the Bose-Einstein statistics.
Conversely, at a fixed value of N, their is a critical temperature T_C under which the condensation occurs. From equation 1.56 it comes:

$$T_C \propto \frac{2\pi\hbar^2}{m k_B} n_C^{2/3} \tag{1.58}$$

A more qualitative approach leading to this result consists in comparing the thermal wavelength of bosons and their typical separation (see figure 1.13). The Bose-Einstein condensation occurs when these two characteristic distances are comparable: wavefunctions of particles see each other, the system of bosons in ground state has a unique wavefunction and exhibits a collective state characterised by a long-range spatial coherence. At a fixed temperature T, the thermal de Broglie wavelength is

$$\lambda_T \propto \frac{h}{\sqrt{m k_B T}} \tag{1.59}$$

In the 3D case, at a density of particles n, the typical interparticle distance is given by $n^{-1/3}$. Equalising the two distances and extracting T_C, we obtain, in accordance with equation 1.58:

$$T_C \propto \frac{h^2}{m k_B} n_C^{2/3} \tag{1.60}$$

Such a collective state has been predicted by Einstein in 1925 after the work of Bose and should be distinguished from the situation where all particles follow the Bose-Einstein statistics and are in the ground state due to a very low temperature,

much lower than T_C.

Features of an excitons BEC The first experimental observations of a Bose-Einstein condensate have been realised in cold alkali atom gases since 1995 leading to the 2001 Nobel prize which was shared by Ketterle [80, 81], Cornell and Wieman [82, 83]. Due to the atomic mass and to the gases densities (Rubidium gas at $\approx 10^{11}\text{cm}^{-3}$ and Sodium gas at $\approx 10^{14}\text{cm}^{-3}$ in [82] and [80] respectively), the BEC occurs at ultra-low temperatures (20 nK and 2 μK respectively) which imply the use of very complex experimental techniques (such as optical cooling, optical evaporation and magneto-optical trapping of cold atoms).
In 1968, Keldysh and Kozlov have suggested that excitons, as bosonic quasi-particle, may also exhibit Bose-Einstein condensation [79]. Because of their effective mass (six order of magnitude lower than typical atom mass) and their size (densities of $\approx 10^{10}\text{cm}^{-3}$ are reasonably accessible), the critical temperature is expected to be in the order of a few Kelvin which is much easier reachable with cryogenic techniques. Nevertheless, the pursuit of the observation of an exciton Bose-Einstein condensate has been full of surprises. Indeed, several conditions must be fulfilled to allow for the formation of such a condensate.

First of all, excitons being optically generated, they are hot and have to thermalise with the lattice to actually reach the cryogenic temperature. This thermalisation occurs on the time scale of ns which is more than excitons lifetime and excitons can not cool down under T_C.
The second consideration which is worth our attention is the validity of the assumption of the bosonic nature of excitons: being composite bosons, the bosonic behaviour of exciton is guaranteed as long as the fundamentally fermionic nature of its constituents does not come into play. A coarse analysis leads to considering the following criterion: the interparticle distance has to be longer than their Bohr radius. This is an upper limit for the density and thus for the quantum degeneracy temperature.
Finally, the spin structure of excitons plays a crucial role. As mentioned in section 1.3.1, excitons have four spin states among which two are dark and two are bright. The role of the energy splitting Δ_0 between dark and bright states on exciton BEC has been highlighted recently [84, 85] : dark states being the lowest in energy, such a condensate should be characterised by an optical inactivity making its observation difficult. Experimental observation of the darkening of excitons have actually been reported [86, 87].

Dipolar indirect excitons

Different systems have been investigated in the context of high exciton lifetimes. Dipolar forbidden transition para-excitons in bulk Cu_2O for instance are expected to have a high T_C (cryogenic temperature ≈ 2 K at high density $n \approx 10^{17}$ cm^{-3}) and a low radiative recombination rate [88, 89]. However, these densities have not been reached due to exciton Auger recombination [90–92]. Excitons in indirect gap semiconductor have also been considered. However, the lowest in energy excited state in such material - such as Si or Ge - is not excitonic but is an electron-hole liquid [93]. More recently, it have been suggested to increase the exciton lifetime suppressing their recombination [94]. This can be achieved in a quantum well embedded into an photonic cavity.

In this work, we focus on an other way to increase the lifetime of excitons. As early as 1976, it have been suggested to spatially separate their two constituents, the electron and the hole [95]. This results in a decrease of the overlap of their wavefunctions and therefore in an increase of the exciton lifetime [96–100].
Such excitons are referred to as dipolar excitons or spatially indirect excitons. One should make the difference with excitons indirect in k-space for which the optical channel of recombination is frozen because the hole and the electron have different wave vector.
This separation may be provided in a wide biased quantum well or in biased coupled quantum wells structure. In the latter case, the electric field pushes electrons and holes to be confined in different quantum wells. The lifetime can be enhanced by several orders of magnitude allowing the thermalisation of excitons with the lattice [100]. This separation implies also a permanent dipole moment aligned in the growth direction.

For dipolar excitons in quantum wells, the quantum degeneracy temperature differs from the 3D case. In 2D systems, this temperature is given by [101]:

$$T_C^{2D} = 2\pi\hbar^2 n/M \tag{1.61}$$

where n is the density of excitons and M is their mass. It is therefore important to reach a sufficient density (in coupled QWs GaAs, this temperature is about 3 K for a density of 10^{10} cm^{-2}).
However, indirect excitons repeal each other due to their permanent dipolar moment. For a given T_C, the critical density for condensation can therefore be reached provided

a confinement of excitons in the plane of the wells. This in plane confinement of indirect excitons may be achieved using an electrostatic trap: if the top-electrode providing the bias of the coupled quantum wells (CQW) structure is localised in space, indirect excitons could exist only is this region [102].
This electric dipole moment prevents also the formation of biexcitons that could otherwise form the ground state of the system [103–105]. As a result, it is possible to study exciton condensation and ignore biexciton formation up to the destruction of excitons and the formation of electron-hole plasma at high carrier densities (Mott transition) [106–109].
Finally, a very important property of IX is their very long spin relaxation time. Indeed, because of the reduced overlap of electron and hole, the exchange interaction is drastically decreased and the associated Maille, Andrada e Silva and Sham mechanism is warded off [73, 76]. This allows very rich phenomena including long-range spin currents and spin textures [96, 100, 110]. Such pattern formation suggests the possibility of ballistic transport in the exciton gases on a micron-scale [111, 112].

* *
*

This section has designed indirect excitons as a very promising system to study various collective states and spin phenomena. It has also evidenced challenges facing the community, including the optical inactivity of the lower in energy states. The next section introduces possible directions to overcome this problem.

1.3.2 How to detect dark states?

Knowing the dark nature of indirect excitons in their ground state [86, 87, 98, 110, 113, 114]. , the question of their detection plays a crucial role in the study of excitonic condensates. Linear optics methods, such as photoluminescence, have been widely used to study indirect excitons allowing the observation of many of their quantum properties [97]. Nevertheless, the direct observation of a dark indirect excitons condensate seems to be impractical. A macroscopic condensation of indirect exciton in their dark ground state would result in a variation of the PL intensity. However, so much different potential causes of this variation should occur and will be hard to unravel.
Combescot *et al.* [84, 85, 98] have highlighted a coupling between the two subpopulations of dark and bright excitons under certain specific density conditions. Taking advantage of this coupling, an experimental evidence of such a "grey" condensate has been provided via the detection of the coherence of its bright component [87, 98].
Nevertheless, the detection of dark excitonic BEC in the regime where there is

no coupling between dark and bright states is impossible via photoluminescence experiments, preventing the exploration of the phase diagram of the excitonic states.

Non linear optics as a probe of IX

To circumvent this issue, an alternative approach based on non-linear optics has been proposed in [115] to address dark states. In quantum wells, resonant optical pumping of direct exciton (DX) transition with circularly polarised light and delayed detection of the induced dispersive response is widely used to study density and spin dynamics of electrons, holes and excitons [116–119]. In reflection geometry, a modification of the intensity (photodinduced reflectivity) or a rotation of the polarisation plane (Kerr rotation) of the reflected lineraly polarised probe are measured (see section 1.1.3). The intensity of the signal is sharply resonant and proportional to the square of the oscillator strength of the probed transition. Thus, such pump-probe methods are a priori not suited for the study of IX which have low oscillator strength. In [115], Nalitov *et al.* have suggested a subtle way to reach IX through the DX transition despite their vanishing oscillator strength. This method should also provide a differentiation between dark and bright state in adequate CQW structure.
Let's consider the biased CQW represented in figure 1.14. Electron and hole are confined in different wells and we can denote the two DX transitions as DX_e and DX_h. The suggested approach relies on the coupling between DX and IX. This coupling originates from the sharing of the electrons population between IX and DX_e and the sharing of the holes population between IX and DX_h. Because this coupling is spin dependent (see below), this method requires the electronic spin coherence conservation during tunnelling which is a reasonable assumption for thin GaAs barrier [120].
In such a structure, the amplitude reflection coefficient r depends on the amplitude reflection coefficient of the QW r_{QW} which is given by:

$$r_{QW}(\omega) = \frac{i\Gamma_0}{\omega_0 - \omega - i(\Gamma_0 + \Gamma)} \tag{1.62}$$

where Γ_0 is the radiative decay rate , Γ the non radiative broadening and ω_0 is the frequency of the exciton transition. Due to spin-dependent Coulomb interaction or scattering process between IX and DX, the IX population can alter either Γ, Γ_0 or ω_0 of a DX transition.
These modifications are spin-dependent and modification of the amplitude reflection

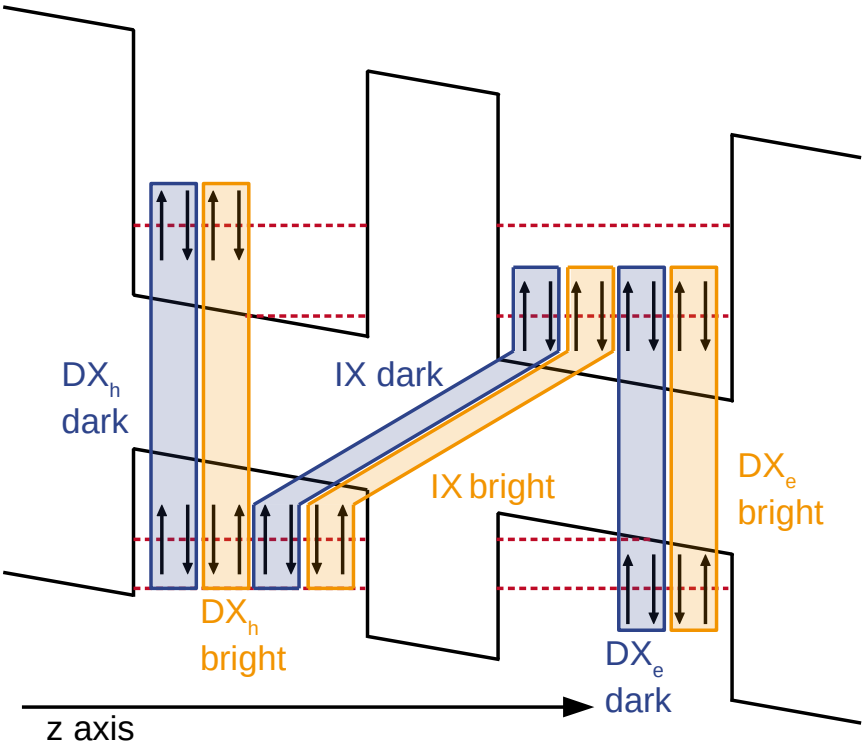

Figure 1.14: Different exciton states in a biased CQW structure. There are four different direct states in each QW and four indirect states with electron in one well and hole in the other well. These four states correspond to two bright and two dark states (see section 1.3.1). Here, indirect states with both electron and hole in the less favourable well are not represented.

coefficient r of the sample (which depends on r_{QW}) can be expressed as:

$$\delta r^{\pm} = \frac{\partial r}{\partial \omega_0}\delta\omega_0^{\pm} + \frac{\partial r}{\partial \Gamma_0}\delta\Gamma_0^{\pm} + \frac{\partial r}{\partial \Gamma}\delta\Gamma^{\pm} \tag{1.63}$$

where $\pm$ denotes the circular polarisation. For a linearly polarised normal incident wave $\vec{E_i} = E_0 e^{i(kz-\omega t)}\vec{e_x}$, the reflected beam can be written in the basis of two circularly polarised states $\vec{e_{\pm}} = \dfrac{\vec{e_x} \pm i\vec{e_y}}{\sqrt{2}}$:

$$\vec{E_r} = \frac{E_0}{\sqrt{2}}[(r+\delta_r^+)\vec{e_+} + (r+\delta_r^-)\vec{e_-}] \tag{1.64}$$

Thus, photo-induced reflectivity and Kerr rotation signals are given by:

$$\delta R_i = |r|^2 \mathcal{R}e\{\frac{\delta r^+ + \delta r^-}{r}\} \qquad \text{and} \qquad \delta\theta_i = -\mathit{Im}\{\frac{\delta r^+ - \delta r^-}{2r}\} \tag{1.65}$$

and can be probed at each direct transitions.Indeed, the interaction between DX and IX being controlled by the density and spin of the shared electron or hole, the

contributions of the signal are different for the two DX transitions. The situation is depicted in figure 1.14 and table 1.1 summarises the possible interactions. For example, the +1 DX_h state shares its hole with the +1 IX state. This is indicated by a check mark on the third line and the fourth column. Assuming that the

	$DX_e \downarrow\Uparrow$ (+1)	$DX_e \uparrow\Downarrow$ (−1)	$DX_h \downarrow\Uparrow$ (+1)	$DX_h \uparrow\Downarrow$ (−1)
IX $\uparrow\Uparrow$ (+2)		✓	✓	
IX $\downarrow\Uparrow$ (+1)	✓		✓	
IX $\uparrow\Downarrow$ (−1)		✓		✓
IX $\downarrow\downarrow$ (−2)	✓			✓

Table 1.1: Interaction between four indirect exciton states and all the bright direct exciton states. Check marks identify situations for which one of the indirect exciton states shares one particle with one of the bright exciton states.

$\delta\omega_0$ contribution is the main source of non linearity, Nalitov et al, have expressed the signal obtained from both DX_i resonances ($i = e, h$) in Kerr rotation ($\delta\theta_i$) and in photo-induced reflectivity (δR_i) as a function of the different IX subpopulation densities. It is shown that polarisation of bright and dark states are related to the Kerr rotation detected on electron and hole QW:

$$n_1^+ - n_1^- \sim \delta\theta_e + \delta\theta_h \tag{1.66}$$

$$n_2^+ - n_2^- \sim \delta\theta_e - \delta\theta_h \tag{1.67}$$

and the total IX density is related to the photo-induced reflectivity:

$$n_1^+ + n_1^- + n_2^+ + n_2^- \sim \delta R_e \sim \delta R_h \tag{1.68}$$

Dark and bright subpopulations densities can therefore be unravelled performing both photoreflectivity and photoluminescence. Their respective spin polarisation can be obtained separately provided non degenerate DX transitions, that means from different width QW for instance.

Proof-of-concept of this promising method have been achieved by Andreakou *et al.* [121]. In this work, lifetime of DX and IX are addressed. Spin relaxation time of IX, DX and also free electrons are detected on a wide range of electric field. However, the studied CQW was symmetric and dark and bright states were not distinguished.

* *
*

This section has introduced indirect excitons in CQW as an exciting, albeit difficult, playground for the study of quantum states. Main features of the expected BEC - including its optical inactivity - has been highlighted. In this context, a specific structure has been proposed as providing a solution to reach dynamics of dark IX states.

1.4 Summary

This chapter has introduced the background concepts used in this thesis:

- spin dynamics in semiconductors (optical orientation of spin carriers in semiconductors and spin relaxation)
- optical technics used to address spin dynamics: photoluminescence, pump-probe and spin noise spectroscopy

A special emphasis is given on specific features of indirect excitons and on spin noise spectroscopy which will be discussed in what follows.

Bibliography

[1] Georges Lampel. Nuclear dynamic polarization by optical electronic saturation and optical pumping in semiconductors. *Physical Review Letters*, 20(10):491, 1968. [1.1]

[2] RR Parsons. Band-to-band optical pumping in solids and polarized photoluminescence. *Physical Review Letters*, 23(20):1152, 1969. [1.1]

[3] Felix Meier and Boris Petrovich Zakharchenya. *Optical orientation*. Elsevier, 2012. [1.1]

[4] Michel I Dyakonov and AV Khaetskii. *Spin physics in semiconductors*, volume 1. Springer, 2017. [1.1, 1.1.2]

[5] MW Wu, JH Jiang, and MQ Weng. Spin dynamics in semiconductors. *Physics Reports*, 493(2-4):61–236, 2010. [1.1]

[6] Igor Žutić, Jaroslav Fabian, and S Das Sarma. Spintronics: Fundamentals and applications. *Reviews of modern physics*, 76(2):323, 2004. []

[7] Georg M Müller, Michael Oestreich, Michael Römer, and Jens Hübner. Semiconductor spin noise spectroscopy: Fundamentals, accomplishments, and challenges. *Physica E: Low-dimensional Systems and Nanostructures*, 43(2):569–587, 2010. [1.1]

[8] David Pines and Charles P Slichter. Relaxation times in magnetic resonance. *Physical Review*, 100(4):1014, 1955. [1.1.2]

[9] Charles P Slichter. *Principles of magnetic resonance*, volume 1. Springer Science & Business Media, 2013. [1.1.2]

[10] Guy Fishman and Georges Lampel. Spin relaxation of photoelectrons in p-type gallium arsenide. *Physical Review B*, 16(2):820, 1977. [1.1.2]

[11] R _ J Elliott. Theory of the effect of spin-orbit coupling on magnetic resonance in some semiconductors. *Physical Review*, 96(2):266, 1954. [1.1.2]

[12] AG Aronov, GE Pikus, and AN Titkov. Spin relaxation of conduction electrons in p-type iii-v compounds. *Sov. Phys. JETP*, 57:680, 1983. [1.1.2]

[13] GL Bir, AG Aronov, and GE Pikus. Spin relaxation of electrons due to scattering by holes. *Zh. Eksp. Teor. Fiz*, 69(4):1382, 1975. [1.1.2]

[14] MI D'yakonov. Spin orientation of electrons associated with the interband absorption of light in semiconductors. *Sov. Phys. JETP*, 33(5):1053–1059, 1971. [1.1.2]

[15] Leon C Camenzind, Liuqi Yu, Peter Stano, Jeramy D Zimmerman, Arthur C Gossard, Daniel Loss, and Dominik M Zumbühl. Hyperfine-phonon spin relaxation in a single-electron gaas quantum dot. *Nature communications*, 9(1):3454, 2018. [1.1.2]

[16] I. A. Merkulov, Al. L. Efros, and M. Rosen. Electron spin relaxation by nuclei in semiconductor quantum dots. *Phys. Rev. B*, 65:205309, 2002. [1.1.2]

[17] K_V Kavokin. Anisotropic exchange interaction of localized conduction-band electrons in semiconductors. *Physical Review B*, 64(7):075305, 2001. [1.1.2]

[18] BI Shklovskii. Dyakonov-perel spin relaxation near the metal-insulator transition and in hopping transport. *Physical Review B*, 73(19):193201, 2006. [1.1.2]

[19] KV Kavokin. Spin relaxation of localized electrons in n-type semiconductors. *Semiconductor Science and Technology*, 23(11):114009, 2008. [1.1.2]

[20] RI Dzhioev, KV Kavokin, VL Korenev, MV Lazarev, B Ya Meltser, MN Stepanova, BP Zakharchenya, D Gammon, and DS Katzer. Low-temperature spin relaxation in n-type gaas. *Physical Review B*, 66(24):245204, 2002. [1.1.2, 1.5]

[21] Jan G Lonnemann, Eddy P Rugeramigabo, Michael Oestreich, and Jens Hübner. Closing the gap between spatial and spin dynamics of electrons at the metal-to-insulator transition. *Physical Review B*, 96(4):045201, 2017. [1.1.2]

[22] VV Belykh, A Yu Kuntsevich, MM Glazov, KV Kavokin, DR Yakovlev, and M Bayer. Quantum interference controls the electron spin dynamics in n-gaas. *Physical Review X*, 8(3):031021, 2018. [1.1.2]

[23] DJ Hilton and Chung L Tang. Optical orientation and femtosecond relaxation of spin-polarized holes in gaas. *Physical review letters*, 89(14):146601, 2002. [1.1.3]

[24] Anatole Abragam and Anatole Abragam. *The principles of nuclear magnetism*. Number 32. Oxford university press, 1961. [1.1.3]

[25] A Greilich, DR Yakovlev, A Shabaev, Al L Efros, IA Yugova, R Oulton, V Stavarache, D Reuter, A Wieck, and M Bayer. Mode locking of electron spin coherences in singly charged quantum dots. *Science*, 313(5785):341–345, 2006. [1.1.3]

[26] Lars Onsager. Reciprocal relations in irreversible processes. i. *Physical review*, 37(4):405, 1931. [1.2]

[27] Lars Onsager. Reciprocal relations in irreversible processes. ii. *Physical review*, 38(12):2265, 1931. []

[28] Rep Kubo. The fluctuation-dissipation theorem. *Reports on progress in physics*, 29(1):255, 1966. [1.2]

[29] Herbert B Callen and Theodore A Welton. Irreversibility and generalized noise. *Physical Review*, 83(1):34, 1951. [1.2]

[30] John Bertrand Johnson. Thermal agitation of electricity in conductors. *Physical review*, 32(1):97, 1928. [1.2]

[31] Harry Nyquist. Thermal agitation of electric charge in conductors. *Physical review*, 32(1):110, 1928. [1.2]

[32] Dibyendu Roy, Luyi Yang, Scott A Crooker, and Nikolai A Sinitsyn. Cross-correlation spin noise spectroscopy of heterogeneous interacting spin systems. *Scientific reports*, 5:9573, 2015. [1.2.1, 1.2.2]

[33] AT Dellis, M Loulakis, and IK Kominis. Spin-noise correlations and spin-noise exchange driven by low-field spin-exchange collisions. *Physical Review A*, 90(3):032705, 2014. [1.2.1]

[34] Fuxiang Li, SA Crooker, and NA Sinitsyn. Higher-order spin-noise spectroscopy of atomic spins in fluctuating external fields. *Physical Review A*, 93(3):033814, 2016. [1.2.1, 1.2.2]

[35] Nina Fröhling, Natalie Jäschke, and Frithjof B Anders. Fourth-order spin correlation function in the extended central spin model. *Physical Review B*, 99(15):155305, 2019. [1.2.1]

[36] Lev Davidovich Landau, JS Bell, MJ Kearsley, LP Pitaevskii, EM Lifshitz, and JB Sykes. *Electrodynamics of continuous media*, volume 8. elsevier, 2013. [1.2.1]

[37] PS Pershan, JP Van der Ziel, and LD Malmstrom. Theoretical discussion of the inverse faraday effect, raman scattering, and related phenomena. *Physical Review*, 143(2):574, 1966. [1.2.1]

[38] R Romestain, S Geschwind, and GE Devlin. Measurement of spin-flip-raman-scattering cross section and exchange effects for donors in cds by faraday rotation. *Physical Review Letters*, 35(12):803, 1975. []

[39] BM Gorbovitsky and VI Perel. Aleksandrov and zapassky experiment and raman effect. *OPTIKA I SPEKTROSKOPIYA*, 54(3):388–390, 1983. [1.2.1]

[40] BM Gorbovitskii and VI Perel. Aleksandrov and zapasskii experiment and the raman effect. *Optics and Spectroscopy*, 54:229–230, 1983. [1.2.1]

[41] MM Glazov and VS Zapasskii. Linear optics, raman scattering, and spin noise spectroscopy. *Optics express*, 23(9):11713–11723, 2015. [1.2.1]

[42] Valerii S Zapasskii, Alex Greilich, Scott A Crooker, Yan Li, Gleb G Kozlov, Dmitri R Yakovlev, Dirk Reuter, Andreas D Wieck, and Manfred Bayer. Optical spectroscopy of spin noise. *Physical review letters*, 110(17):176601, 2013. [1.2.1, 1.2.2]

[43] Luyi Yang, P Glasenapp, A Greilich, D Reuter, AD Wieck, DR Yakovlev, M Bayer, and SA Crooker. Two-colour spin noise spectroscopy and fluctuation correlations reveal homogeneous linewidths within quantum-dot ensembles. *Nature communications*, 5:4949, 2014. [1.2.1, 1.2.2]

[44] M Römer, J Hübner, and M Oestreich. Spatially resolved doping concentration measurement in semiconductors via spin noise spectroscopy. *Applied Physics Letters*, 94(11):112105, 2009. [1.2.1]

[45] EB Aleksandrov and VS Zapasskii. Magnetic resonance in the faraday-rotation noise spectrum. *Zh. Eksp. Teor. Fiz*, 81:132–138, 1981. [1.2.2, 1.2.2]

[46] SA Crooker, DG Rickel, AV Balatsky, and DL Smith. Spectroscopy of spontaneous spin noise as a probe of spin dynamics and magnetic resonance. *Nature*, 431(7004):49, 2004. [1.2.2, 1.2.2]

[47] M Römer, J Hübner, and M Oestreich. Spin noise spectroscopy in semiconductors. *Review of Scientific Instruments*, 78(10):103903, 2007. [1.2.2]

[48] Sebastian Starosielec and Daniel Hägele. Ultrafast spin noise spectroscopy. *Applied Physics Letters*, 93(5):051116, 2008. [1.2.2]

[49] Georg M Müller, Michael Römer, Jens Hübner, and Michael Oestreich. Gigahertz spin noise spectroscopy in n-doped bulk gaas. *Physical Review B*, 81(12):121202, 2010. [1.2.2]

[50] Fabian Berski, Hendrik Kuhn, Jan G Lonnemann, Jens Hübner, and Michael Oestreich. Ultrahigh bandwidth spin noise spectroscopy: Detection of large g-factor fluctuations in highly-n-doped gaas. *Physical review letters*, 111(18):186602, 2013. [1.2.2]

[51] Jens Hübner, Jan Gerrit Lonnemann, Petrissa Zell, Hendrik Kuhn, Fabian Berski, and Michael Oestreich. Rapid scanning of spin noise with two free running ultrafast oscillators. *Optics express*, 21(5):5872–5878, 2013. [1.2.2]

[52] G Sucha, ME Fermann, DJ Harter, and M Hofer. Rapid temporal scanning of ultrafast lasers. In *Ultrafast Electronics and Optoelectronics*, page UE5. Optical Society of America, 1997. [1.2.2]

[53] Steeve Cronenberger and Denis Scalbert. Quantum limited heterodyne detection of spin noise. *Review of Scientific Instruments*, 87(9):093111, 2016. [1.2.2]

[54] Pavel Sterin, Julia Wiegand, Jens Hübner, and Michael Oestreich. Optical amplification of spin noise spectroscopy via homodyne detection. *Physical Review Applied*, 9(3):034003, 2018. [1.2.2]

[55] M Yu Petrov, AN Kamenskii, VS Zapasskii, M Bayer, and A Greilich. Increased sensitivity of spin noise spectroscopy using homodyne detection in n-doped gaas. *Physical Review B*, 97(12):125202, 2018. [1.2.2]

[56] Fuxiang Li, Avadh Saxena, Darryl Smith, and Nikolai A Sinitsyn. Higher-order spin noise statistics. *New Journal of Physics*, 15(11):113038, 2013. [1.2.2]

[57] Yuriy V Pershin, Valeriy A Slipko, Dibyendu Roy, and Nikolai A Sinitsyn. Two-beam spin noise spectroscopy. *Applied Physics Letters*, 102(20):202405, 2013. [1.2.2]

[58] GG Kozlov, II Ryzhov, and VS Zapasskii. Light scattering in a medium with fluctuating gyrotropy: Application to spin-noise spectroscopy. *Physical Review A*, 95(4):043810, 2017. [1.2.2, 1.2.3]

[59] GG Kozlov, II Ryzhov, and VS Zapasskii. Spin-noise spectroscopy of randomly moving spins in the model of light scattering: Two-beam arrangement. *Physical Review A*, 97(1):013848, 2018. [1.2.2, 1.2.3]

[60] Michael Oestreich, M Römer, Rolf J Haug, and D Hägele. Spin noise spectroscopy in gaas. *Physical review letters*, 95(21):216603, 2005. [1.2.2]

[61] Georg M Müller, Michael Römer, Dieter Schuh, Werner Wegscheider, Jens Hübner, and Michael Oestreich. Spin noise spectroscopy in gaas (110) quantum wells: Access to intrinsic spin lifetimes and equilibrium electron dynamics. *Physical review letters*, 101(20):206601, 2008. [1.2.2]

[62] SA Crooker, J Brandt, C Sandfort, A Greilich, DR Yakovlev, D Reuter, AD Wieck, and M Bayer. Spin noise of electrons and holes in self-assembled quantum dots. *Physical review letters*, 104(3):036601, 2010. [1.2.2]

[63] Ramin Dahbashi, Jens Hübner, Fabian Berski, Klaus Pierz, and Michael Oestreich. Optical spin noise of a single hole spin localized in an (inga) as quantum dot. *Physical review letters*, 112(15):156601, 2014. [1.2.2]

[64] Steeve Cronenberger, Denis Scalbert, David Ferrand, Hervé Boukari, and Joël Cibert. Atomic-like spin noise in solid-state demonstrated with manganese in cadmium telluride. *Nature communications*, 6:8121, 2015. [1.2.2]

[65] MM Glazov, MA Semina, E Ya Sherman, and AV Kavokin. Spin noise of exciton polaritons in microcavities. *Physical Review B*, 88(4):041309, 2013. [1.2.2]

[66] SV Poltavtsev, II Ryzhov, MM Glazov, GG Kozlov, VS Zapasskii, AV Kavokin, PG Lagoudakis, DS Smirnov, and EL Ivchenko. Spin noise spectroscopy of a single quantum well microcavity. *Physical Review B*, 89(8):081304, 2014. [1.2.2]

[67] Andreas V Kuhlmann, Julien Houel, Arne Ludwig, Lukas Greuter, Dirk Reuter, Andreas D Wieck, Martino Poggio, and Richard J Warburton. Charge noise and spin noise in a semiconductor quantum device. *Nature Physics*, 9(9):570, 2013. [1.2.2]

[68] Ivan I Ryzhov, Gleb G Kozlov, Dmitrii S Smirnov, Mikhail M Glazov, Yurii P Efimov, Sergei A Eliseev, Viacheslav A Lovtcius, Vladimir V Petrov, Kirill V Kavokin, Alexey V Kavokin, et al. Spin noise explores local magnetic fields in a semiconductor. *Scientific reports*, 6:21062, 2016. [1.2.2]

[69] Maria Vladimirova, Steeve Cronenberger, Denis Scalbert, M Kotur, RI Dzhioev, II Ryzhov, GG Kozlov, VS Zapasskii, A Lemaître, and KV Kavokin. Nuclear spin relaxation in n-gaas: From insulating to metallic regime. *Physical Review B*, 95(12):125312, 2017. [1.2.2]

[70] Gregory H. Wannier. The structure of electronic excitation levels in insulating crystals. *Phys. Rev.*, 52:191–197, 1937. [1.3.1]

[71] E F Gross and N. A Karryjew. The optical spectrum of the exciton. *Dokl. Akad. Nauk SSSR*, 84:471–474, 1952. [1.3.1]

[72] K. Sivalertporn, L. Mouchliadis, A. L. Ivanov, R. Philp, and E. A. Muljarov. Direct and indirect excitons in semiconductor coupled quantum wells in an applied electric field. *Phys. Rev. B*, 85:045207, 2012. [1.3.1]

[73] A Vinattieri, Jagdeep Shah, T C Damen, D S Kim, L N Pfeiffer, M Z Maialle, and L J Sham. Exciton dynamics in GaAs quantum wells under resonant excitation. *Phys. Rev. B*, 50(15):10868–10879, October 1994. [1.3.1, 1.3.1, 1.3.1]

[74] B Deveaud, F Clérot, N Roy, K Satzke, B Sermage, and DS Katzer. Enhanced radiative recombination of free excitons in gaas quantum wells. *Physical review letters*, 67(17):2355, 1991. [1.3.1]

[75] WAJA van der Poel, LW Molenkamp, CT Foxon, et al. Giant oscillator strength of free excitons in gaas. *Physical Review B*, 35(15):8281, 1987. [1.3.1]

[76] MZ Maialle. Mz maialle, ea de andrada e silva, and lj sham, phys. rev. b 47, 15776 (1993). *Phys. Rev. B*, 47:15776, 1993. [1.3.1, 1.3.1, 1.3.1]

[77] T Amand, X Marie, P Le Jeune, M Brousseau, D Robart, J Barrau, and R Planel. Spin quantum beats of 2d excitons. *Physical review letters*, 78(7):1355, 1997. [1.3.1]

[78] M Dyakonov, X Marie, T Amand, P Le Jeune, D Robart, M Brousseau, and J Barrau. Coherent spin dynamics of excitons in quantum wells. *Physical Review B*, 56(16):10412, 1997. [1.3.1]

[79] L V Keldysh and A N Kozlov. Collective properties of excitons in semiconductors. *Soviet Physics JETP*, 27:521, May 1968. [1.3.1, 1.3.1]

[80] Kendall B Davis, M-O Mewes, Michael R Andrews, Nicolaas J van Druten, Dallin S Durfee, DM Kurn, and Wolfgang Ketterle. Bose-einstein condensation in a gas of sodium atoms. *Physical review letters*, 75(22):3969, 1995. [1.3.1]

[81] Wolfgang Ketterle. Nobel lecture: When atoms behave as waves: Bose-einstein condensation and the atom laser. *Reviews of Modern Physics*, 74(4):1131, 2002. [1.3.1]

[82] Mike H Anderson, Jason R Ensher, Michael R Matthews, Carl E Wieman, and Eric A Cornell. Observation of bose-einstein condensation in a dilute atomic vapor. *science*, pages 198–201, 1995. [1.3.1]

[83] JR Ensher, Deborah S Jin, MR Matthews, CE Wieman, and Eric A Cornell. Bose-einstein condensation in a dilute gas: Measurement of energy and ground-state occupation. *Physical Review Letters*, 77(25):4984, 1996. [1.3.1]

[84] Monique Combescot, Odile Betbeder-Matibet, and Roland Combescot. Bose-einstein condensation in semiconductors: The key role of dark excitons. *Physical review letters*, 99(17):176403, 2007. [1.3.1, 1.3.2]

[85] M Combescot and M N Leuenberger. General argument supporting Bose–Einstein condensate of dark excitons in single and double quantum wells. *Solid State Communications*, 149(13-14):567–571, April 2009. [1.3.1, 1.3.2]

[86] Yehiel Shilo, Kobi Cohen, Boris Laikhtman, Ken West, Loren Pfeiffer, and Ronen Rapaport. Particle correlations and evidence for dark state condensation in a cold dipolar exciton fluid. *Nat Commun*, 4:2325, 2013. [1.3.1, 1.3.2]

[87] Mathieu Alloing, Mussie Beian, Maciej Lewenstein, David Fuster, Yolanda González, Luisa González, Roland Combescot, Monique Combescot, and François Dubin. Evidence for a Bose-Einstein condensate of excitons. *EPL*, 107(1):10012, July 2014. [1.3.1, 1.3.2]

[88] D Wolfe Snoke, JP Wolfe, and A Mysyrowicz. Evidence for bose-einstein condensation of excitons in cu 2 o. *Physical Review B*, 41(16):11171, 1990. [1.3.1]

[89] Jia Ling Lin and JP Wolfe. Bose-einstein condensation of paraexcitons in stressed cu 2 o. *Physical review letters*, 71(8):1222, 1993. [1.3.1]

[90] KE O'Hara, L Ó Súilleabháin, and JP Wolfe. Strong nonradiative recombination of excitons in cu 2 o and its impact on bose-einstein statistics. *Physical Review B*, 60(15):10565, 1999. [1.3.1]

[91] DW Snoke, Jia Ling Lin, and JP Wolfe. Coexistence of bose-einstein paraexcitons with maxwell-boltzmann orthoexcitons in cu 2 o. *Physical Review B*, 43(1):1226, 1991. []

[92] DW Snoke, JP Wolfe, and ande A Mysyrowicz. Evidence for bose-einstein condensation of a two-component exciton gas. *Physical review letters*, 64(21):2543, 1990. [1.3.1]

[93] LV Keldysh. The electron-hole liquid in semiconductors. *Contemporary physics*, 27(5):395–428, 1986. [1.3.1]

[94] NS Voronova, IL Kurbakov, and Yu E Lozovik. Bose condensation of long-living direct excitons in an off-resonant cavity. *Physical review letters*, 121(23):235702, 2018. [1.3.1]

[95] Yu E Lozovik and VI Yudson. A new mechanism for superconductivity: pairing between spatially separated electrons and holes. *Zh. Eksp. i Teor. Fiz*, 71:738–753, 1976. [1.3.1]

[96] L. V. Butov, L. S. Levitov, A. V. Mintsev, B. D. Simons, A. C. Gossard, and D. S. Chemla. Formation mechanism and low-temperature instability of exciton rings. *Phys. Rev. Lett.*, 92:117404, 2004. [1.3.1, 1.3.1]

[97] L V Butov. Collective phenomena in cold indirect excitons. *J. Exp. Theor. Phys.*, 149(3):505, 2016. [1.3.2]

[98] Monique Combescot, Roland Combescot, and François Dubin. Bose–Einstein condensation and indirect excitons: a review. *Rep. Prog. Phys.*, 80(6):066501, June 2017. [1.3.2]

[99] L. V. Butov, A. Imamoglu, A. V. Mintsev, K. L. Campman, and A. C. Gossard. Photoluminescence kinetics of indirect excitons in GaAs/$Al_xGa_{1-x}As$ coupled quantum wells. *Phys. Rev. B*, 59:1625–1628, 1999. []

[100] L V Butov. Condensation and pattern formation in cold exciton gases in coupled quantum wells. *J. Phys.: Condens. Matter*, 16(50):R1577–R1613, December 2004. [1.3.1, 1.3.1]

[101] LV Butov, CW Lai, AL Ivanov, AC Gossard, and DS Chemla. Towards bose-einstein condensation of excitons in potential traps. *Nature*, 417(6884):47, 2002. [1.3.1]

[102] AT Hammack, NA Gippius, Sen Yang, GO Andreev, LV Butov, M Hanson, and AC Gossard. Excitons in electrostatic traps, 2006. [1.3.1]

[103] Christoph Schindler and Roland Zimmermann. Analysis of the exciton-exciton interaction in semiconductor quantum wells. *Phys. Rev. B*, 78:045313, 2008. [1.3.1]

[104] S Ben-Tabou de Leon and B Laikhtman. Mott transition, biexciton crossover, and spin ordering in the exciton gas in quantum wells. *Phys. Rev. B*, 67(23):235315, June 2003. []

[105] B Laikhtman and Ronen Rapaport. Correlations in a two-dimensional Bose gas with long-range interaction. *EPL*, 87(2):27010, July 2009. [1.3.1]

[106] N F Mott. Metal-Insulator Transition. *Rev. Mod. Phys.*, 40(4):677–683, October 1968. [1.3.1]

[107] V V Nikolaev and M E Portnoi. Theory of excitonic Mott transition in double quantum wells. *phys. stat. sol. (c)*, 1(6):1357–1362, April 2004. []

[108] V V Nikolaev and M E Portnoi. Theory of the excitonic Mott transition in quasi-two-dimensional systems. *Superlattices and Microstructures*, 43(5-6):460–464, May 2008. []

[109] M Stern, V Garmider, V Umansky, and I Bar-Joseph. Mott Transition of Excitons in Coupled Quantum Wells. *Phys. Rev. Lett.*, 100(25):256402, June 2008. [1.3.1]

[110] L. V. Butov, A. C. Gossard, and D. S. Chemla. Spontaneous coherence in a cold exciton gas. *Nature*, 418:751–754, 2002. [1.3.1, 1.3.2]

[111] Ran Finkelstein, Kobi Cohen, Benoit Jouault, Ken West, Loren N Pfeiffer, Masha Vladimirova, and Ronen Rapaport. Transition from spin-orbit to hyperfine interaction dominated spin relaxation in a cold fluid of dipolar excitons. *Phys. Rev. B*, 96(8):085404, August 2017. [1.3.1]

[112] AV Kavokin, Maria Vladimirova, Benoit Jouault, Timothy Chi Hin Liew, JR Leonard, and LV Butov. Ballistic spin transport in exciton gases. *Physical Review B*, 88(19):195309, 2013. [1.3.1]

[113] A. A. High, J. R. Leonard, A. T. Hammack, M. M. Fogler, L. V. Butov, A. V. Kavokin, K. L. Campman, and A. C. Gossard. Spontaneous coherence in a cold exciton gas. *Nature*, 483:584–588, 2012. [1.3.2]

[114] Kobi Cohen, Yehiel Shilo, Ken West, Loren Pfeiffer, and Ronen Rapaport. Dark High Density Dipolar Liquid of Excitons. *Nano Lett.*, 16(6):3726–3731, May 2016. [1.3.2]

[115] AV Nalitov, Maria Vladimirova, AV Kavokin, LV Butov, and NA Gippius. Nonlinear optical probe of indirect excitons. *Physical Review B*, 89(15):155309, 2014. [1.3.2]

[116] JJ Baumberg, DD Awschalom, Nitin Samarth, H Luo, and JK Furdyna. Spin beats and dynamical magnetization in quantum structures. *Physical review letters*, 72(5):717, 1994. [1.3.2]

[117] JJ Baumberg, SA Crooker, DD Awschalom, Nitin Samarth, H Luo, and JK Furdyna. Ultrafast faraday spectroscopy in magnetic semiconductor quantum structures. *Physical Review B*, 50(11):7689, 1994. []

[118] A Malinowski, RS Britton, T Grevatt, RT Harley, DA Ritchie, and MY Simmons. Spin relaxation in g a a s/a l x ga 1- x as quantum wells. *Physical Review B*, 62(19):13034, 2000. []

[119] RT Harley, OZ Karimov, and M Henini. Optical control of spins in semiconductors. *Journal of Physics D: Applied Physics*, 36(18):2198, 2003. [1.3.2]

[120] M Poggio, GM Steeves, RC Myers, NP Stern, AC Gossard, and DD Awschalom. Spin transfer and coherence in coupled quantum wells. *Physical Review B*, 70(12):121305, 2004. [1.3.2]

[121] Peristera Andreakou, Steeve Cronenberger, Denis Scalbert, A Nalitov, NA Gippius, AV Kavokin, Michal Nawrocki, JR Leonard, LV Butov, KL Campman, et al. Nonlinear optical spectroscopy of indirect excitons in coupled quantum wells. *Physical Review B*, 91(12):125437, 2015. [1.3.2]

Chapter 2

Spin noise spectroscopy in CdTe

Contents

This chapter is dedicated to the study of spin dynamics in n-CdTe thin layers via SNS. The first section will introduce the scientific context underlying our approach. The unexpected observation of the electron precession in the nuclear field is presented and discussed in the second section. Finally, we provide a first attempt to explain this observation.

2.1 Context

Electron spin relaxation at low temperature is considered to be well understood in n-GaAs on the whole range of doping densities [1–3]. Below the metal-to-insulator

transition, two spin relaxation mechanisms compete. The spin precession of the electrons localized on donors in the random local nuclear fields [4], and the spin rotation which occurs as the spin jumps between donors in presence of anisotropic exchange interaction [5]. At the other end of the doping range, in the metallic regime, spin-orbit interaction reigns and electron spin relaxation is due to the Dyakonov-Perel mechanism. At the metal-to-insulator transition, interplay between spin relaxation and spin transport has also been studied providing a complete understanding of the full dynamics of electron spins [6].

CdTe is a model II-VI material with a zinc-blende crystal structure and is expected to demonstrate similar behaviour to GaAs. However, spin physics in CdTe has been less studied and it is of great interest to check if our knowledge in GaAs could be transposed in CdTe.
In contrast to GaAs, nuclear field in CdTe is much lower because not all isotopes carry an angular momentum [7]. Moreover, their angular momentum is 1/2 that means there is no quadrupolar effect which is interesting for optical pumping.

Until the beginning of this work, no investigation on CdTe by SNS has been reported. An old-established collaboration between our team and Hervé Boukari from Nano-Physique et Semi-Conducteurs team at Institut Néel in Grenoble provided a good opportunity to start a study of high quality n-doped CdTe layers.

2.1.1 Samples

We initially defined a set of six samples for systematic measurements of spin noise and to explore the effect of doping density on the satellite line (see section 2.2.2) already observed in old samples (see table 3.1). This set includes five Al:CdTe thin layers (13.3 μm) with different doping densities and a thinner one (500 nm) planned for doping characterisation via Hall measurement. The width of these five samples is a compromise between the optimal width and the growth time, the SN signal increasing linearly with the sample width until the Rayleigh length. In our configuration, this length is of the order of $30\mu m$ which corresponds to an unwise growth time. All these layers have been grown on a 350 nm CdTe(100) substrate. Given the Al effusion temperature, we can expect different doping densities from 10^{15} to 10^{19} cm^{-3} covering the full range from insulator to metallic regime. Tab 2.1.1 summarises the characteristics of these samples.

Sample	Thickness	T(Al) ^{o}C	Expected doping density (cm^{-3})
M3403	13.3 μm	750	1.35×10^{19}
M3404	13.3 μm	690	2×10^{18}
M3405	13.3 μm	630	3×10^{17}
M3406	13.3 μm	580	$\sim10^{16}$
M3407	13.3 μm	520	$\sim10^{15}$
M3408	500 nm	630	For check

2.1.2 Experimental setup

At the wavelength used for spin noise detection, these samples are not transparent. That means that we had to work in backscattering configuration. Moreover, a particular attention has been paid to what happens at low frequencies. We then used a setup allowing optical heterodyning providing a better sensitivity at low probe power.

Optical setup of SNS in heterodyne and backscattering configuration

Figure 2.1 depicts the setup we used. First of all, the beam from a tunable continuous wave (CW) laser (we used a single-mode external cavity diode laser) is split by a polarisation beam splitter to provide both the probe and the local oscillator. A half-wave plate is set between the laser and the PBS to control their relative intensities.

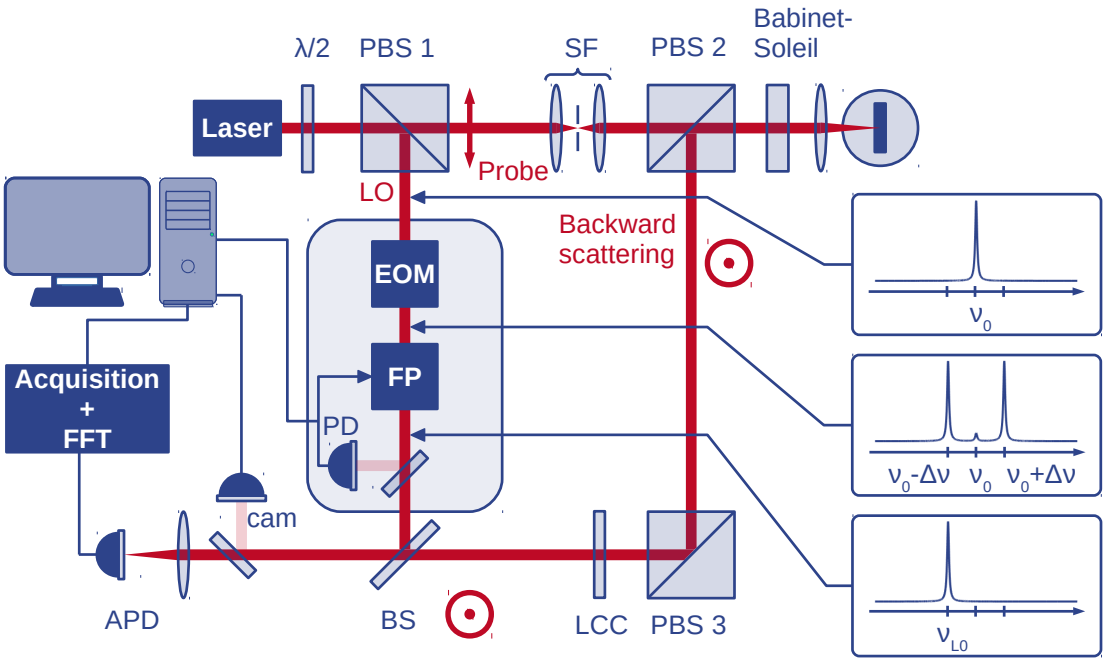

Figure 2.1: Schematics of the backscattering heterodyne spin noise setup.

The transmitted beam (with horizontal linear polarisation) is used as the probe and passes through a spatial filter made of two objectives and a pin hole. It is then focused with a long working distance Mitutoyo objective and sent to the sample which is in a cold-finger optical cryostat. The signal originates from the vertical linearly polarised component of the back-scattered light. This light is collected by the same objective and also passes through the Babinet-Soleil which is used to compensate the birefringence of the sample. A polarised beam splitter is introduced on the probe path : it does not affect the probe but it selects the vertically polarised component of the light. Then, the signal beam is sent to the amplified photodiode.
The vertically polarised beam from the first PBS is used as the local oscillator. For heterodyne measurements, a fiber coupled electro-optic intensity modulator is used to modulate the laser beam. This results in the apparition of two satellites peaks at $\nu_0 \pm \Delta\nu$ in the LO spectrum where ν_0 is the CW laser frequency and $\Delta\nu$ is the EOM frequency. Here we work at $\Delta\nu = 500$ MHz. The LO passes through an active Fabry-Perot (FP) resonator in order to filter out one of the satellite peak and the tiny peak centred on ν_0. A beam splitter picks a weak part of the LO which is sent to a photodiode for active stabilisation of the FP on the satellite peak.
Finally, the LO and the signal beam are recombined by a beam splitter and focused onto the Avalanche photodiode (APD) where they interfere. A switchable beam splitter is introduced in their path and then sends them to a camera in order to check their superposition which is guaranteed by fluctuations of intensity due to their interferences.

Suppression of additional noise

Resulting noise spectra contain not only spin noise but also noise from other sources such as photon noise or electronic noise. These undesired noises do not depend on the applied magnetic field. They can be removed by subtracting two measurements performed at different transverse fields (the corresponding difference of Larmor frequencies should be greater than the width of the peak). In this case, the obtained signal normalised to the photon noise - divided by the frequency response of the detector - is flat and contains two peaks of opposite sign.
In homodyne or heterodyne configuration, the spin noise signal exists only if the LO and the scattered light have the same polarisation. Thus, changing the polarisation of the back scattered light allows to remove the spin noise and to isolate other noises. Modulation of the polarisation of the back scattered light is provided by the liquid crystal compensator (LCC) after the PBS 3 and spin noise is extracted subtracting two consecutive spectra.

2.2 Spin dynamics in CdTe by SNS

In this section, we report the observation of the electron precession in the randomly fluctuating nuclear field in the thinner layer (sample M3408). Because of its Al effusion temperature, its doping density is expected to be near to the metal to insulator transition.

2.2.1 Characterisation of the sample

Both the evolution of the signal with the probe wavelength and the reflectivity spectrum for M3408 are shown in Figure 2.2. The inflexion point in the reflectivity spectrum is attributed to the free exciton. The bound to donor exciton D^0X is expected to be 3 meV below in CdTe.

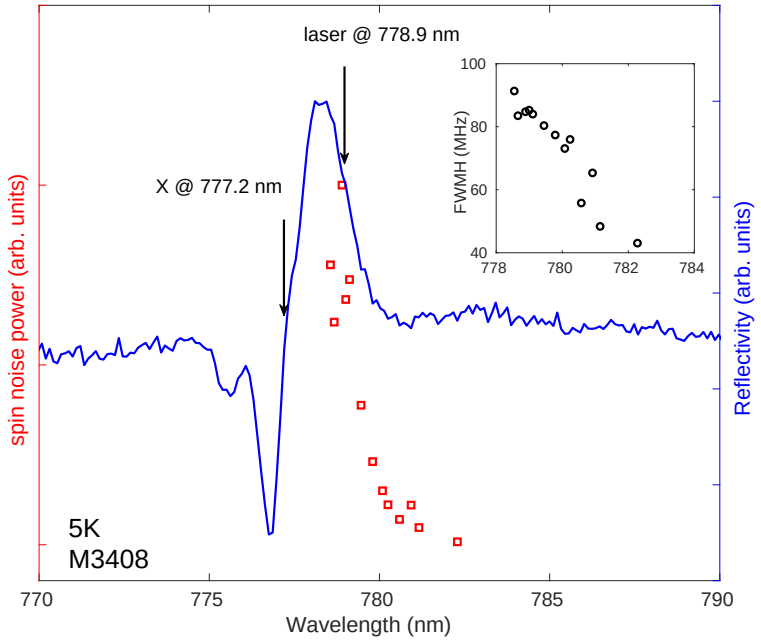

Figure 2.2: Squares: integrated spin noise power measured by the homodyne detection technique as a function of laser wavelength. Solid curve: reflectivity spectrum. The arrow at 778.9 nm indicates the wavelength of the laser at which spin noise measurements reported in the main text have been performed. The position of the free exciton is also shown (X). Inset shows the dependence of the FWHM of SN peak with the wavelength.

Figure 2.2 indicates that the SNS signal is resonant with the D^0X transition. We can also notice that the width of the peak increases strongly at the resonance (see inset). In these conditions ($P_{probe} = 0.73$ mW and probe focused on the sample), the probe clearly disturbs the system via carriers creation or heating for instance. We should work at lower power or off resonance in order to minimize this undesired

perturbation.

2.2.2 Evidence of hyperfine spin-splitting of electrons in zero magnetic field

Observation of a spin-splitting in zero field

As detailed in section 1.2.1, there could be two contributions in a SN spectrum: one comes from the projection of the spin fluctuation in the direction of the applied field, the second one comes from the projection of the spin fluctuation in transverse direction with respect to the applied field.
The longitudinal fluctuation decays with a characteristic time given by the longitudinal spin relaxation time T_1 and its contribution to the SN spectrum is a zero-centred peak whose width is given by $FWHM = 1/\pi T_1$. The transverse fluctuation decays with a characteristic time given by the transverse spin relaxation time T_2 and is also modulated at the Larmor frequency ν_L, leading to a peak centred on ν_L whose width is given by $FWHM = 1/\pi T_2$. In heterodyne configuration, the former is centred on the LO frequency ν_{LO} and the latter is split at $\nu_{LO} \pm \nu_L$.

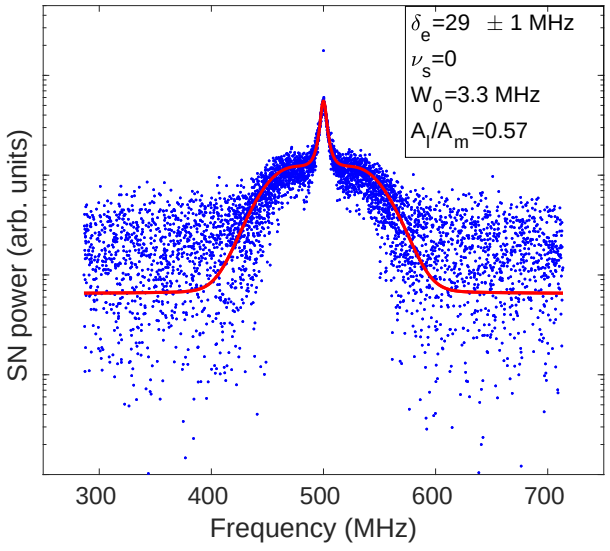

Figure 2.3: Spin noise spectrum measured at zero magnetic field (blue dots, log scale). The red solid curve is the fit with the sum of one lorentzian and two maxwellian distributions. The lorentzian line is centered on 500 MHz because of optical heterodyning. Experimental conditions: $T = 5.5$ K and $P_{probe} = 150$ μW

The first striking observation is the presence, at low power and low temperature, of two satellite peaks in absence of applied transverse magnetic field. Figure 2.3

depicts this unexpected structure. These two peaks being near to the ν_{LO} peak, they correspond to a very weak Larmor frequency and thus a weak magnetic field. Using a three-axis coil does not allow to compensate this field in any direction. This indicates that spin carriers experience an effective random magnetic field. Conversely, applying a transverse magnetic field gradually shifts these peaks at higher Larmor frequencies as expected.

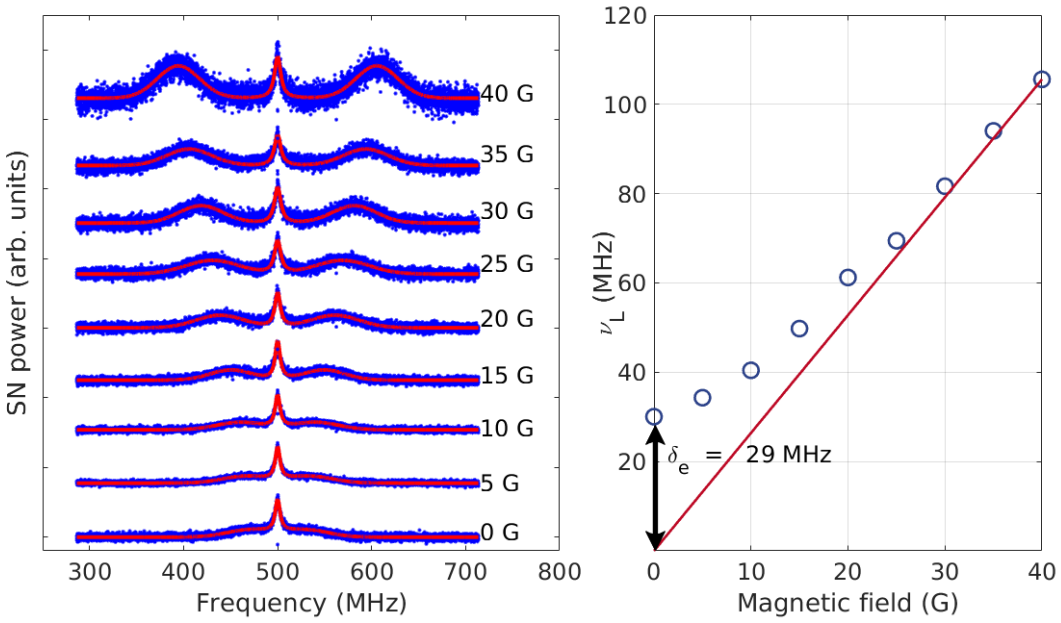

Figure 2.4: Left panel: Evolution of the SN spectrum with transverse magnetic field (blue dots). Red solid lines shows fits with one lorentzian and two gaussian distributions. Right panel: Exctracted Larmor frequencies (blue rings) and expected linear dependance (red solid line). The splitting at $B = 0$ T is $\delta_e = 29$ MHz. Experimental conditions: $T = 5.5$ K and $P_{probe} = 150$ μW

Left panel of figure 2.4 shows the evolution of SN spectra with increasing applied transverse magnetic field. Varying ν_L, we can fit these spectra with a Lorentzian centred on ν_{LO} and two Gaussian centred on $\nu_{LO} \pm \nu_L$. Right panel of figure 2.4 shows ν_L versus the applied transverse magnetic field. This evolution deviates from its expected linear behaviour at low magnetic field. At $B = 0$ T, the splitting is approximatively 29 MHz which corresponds to a field of 1.2 mT.

Modelisation of SN spectra

Such a structure has already been observed in SN spectra in GaAs [8] and has been attributed to the precession of localised electrons in the quasi-static random nuclear field [9, 10]. This experienced field is the result of randomly distributed Overhauser fields of nuclei covered by localised electrons around their donor site.

We can consider two different limit cases, depending on the correlation time of electrons on their donor site τ_c and the spin precession frequency δ_e in this field.
If $\tau_c\delta_e \gg 1$, electrons precess in the static fields of nuclear fluctuations and the SN spectrum contains two contributions: one at $\nu = 0$ corresponding to the electron spin projection along nuclear fields and one centred on δ_e corresponding to the precession. Their respective shapes are described in [9]. The peak centred on 0 has a Lorentzian shape while the peak centred on δ_e has a Maxwellian shape.
In the other case, if $\tau_c\delta_e \ll 1$, electrons do not precess and the static fields of nuclear fluctuations are dynamically averaged. Thus, the SN spectrum contains only one contribution centred on 0.

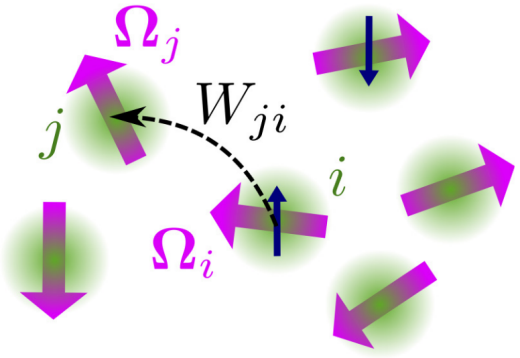

Figure 2.5: Framework of the Glazov's model. Electrons precess in the random nuclear field Ω_i of a donor i and can hop from donor i to donor j with a hopping rate W_0 independent of i and j. Figure taken in [10].

Of course, intermediate values of τ_c could be taken into account. In [10], M. Glazov provides a model which takes into account the interplay between hopping of the electrons among donors and precession in the frozen local nuclear fluctuation.
Figure 2.5 depicts the system: electrons precess in the quasi-static random field on their donor site and hop from one donor site to an other with a hopping rate W_0. The correlation time of electrons is considered to be only due to hopping from a donor to an other and is given by:

$$\tau_c = W_0^{-1} \tag{2.1}$$

Finally, spin relaxation due to other mechanisms (neither hyperfine interaction nor hopping) is supposed to be described by the spin relaxation rate ν_s. Thus, the three main parameters of this model are δ_e, W_0 and ν_s.

This model covers the transition between the two limit regimes which are given by the following equations. The $\tau_c\delta_e \ll 1$ limit case is given by:

$$S(\nu) = A\frac{\Gamma}{\pi(\nu^2+\Gamma^2)} \qquad \text{with} \qquad \Gamma = \frac{\delta_e^2}{W_0} + \nu_s \tag{2.2}$$

which is the expression of a motional narrowing regime for the spin relaxation due to hyperfine interaction.
The two contributions of the $\tau_c\delta_e \gg 1$ limit case are given by:

$$S_M(\nu) = \frac{2A_M}{\sqrt{\pi}\delta_e^3}\nu^2\exp(-\frac{\nu^2}{\delta_e^2}) \tag{2.3}$$

and

$$S_L(\nu) = A_L\frac{\gamma_e}{\pi(\nu^2+\gamma_e^2)} \qquad \text{with} \qquad \gamma_e = \nu_s + \frac{2}{3}W_0 \tag{2.4}$$

for the peaks corresponding respectively to the precession and to the longitudinal contribution. The effective longitudinal relaxation time $T_1 = \gamma_e^{-1}$ is limited either by the hopping - because different donors have different nuclear field orientations - or by other relaxation mechanisms.

The two peaks structure in figure 2.3 is very well described by this model. We found $W_0 = 2\pi \times 3.3$ MHz, $\delta_e = 2\pi \times 29$ MHz and $\nu_s = 0$ MHz, hence the two peaks structure can also be approximated by the limit case $\tau_c\delta_e \gg 1$, with the ratio $A_L/A_M = 0.57$ close to the expected 1/2 theoretical value [10]. However, the model taking into account the hopping between donors reproduces better the shape of dip between the Lorentz and Maxwell lines. Note also that only the value of γ_e is strongly constrained by the width of the Lorentz line, while the values of ν_s and W_0 are more loosely defined.

Determination of the nuclear field at saturation

The observed precession frequency in the quasi-static nuclear field δ_e provides interesting informations about the environment experienced by electrons. We can consider the randomly distributed magnitude and direction of this field are described by a Gaussian density probability distribution given by [11]:

$$W(B_N) = \frac{1}{\pi^{3/2}\Delta_B^3}\exp(-\frac{B_N^2}{\Delta_B^2}) \tag{2.5}$$

where Δ_B is the dispersion of the nuclear hyperfine field distribution given by [4]:

$$\Delta_B^2 = \frac{16I(I+1)}{3N(g_e\mu_B)^2}\sum_\alpha A_\alpha^2\rho_\alpha, \tag{2.6}$$

where g_e is the electron g-factor, μ_B is the Bohr magneton, $N = 64\pi a_B^3/v_0$ is the effective number of nuclei within the Bohr radius of the donor, a_B is the donor Bohr radius, v_0 is the volume of the (non-primitive) unit cell, I is the nuclei spin, A_α is the hyperfine constant for the isotope α (given for the non-primitive unit cell), and ρ_α is the correspondent isotopic abundance. The hyperfine constant is given by

$$A_\alpha = \frac{2}{3}g_0\mu_0\mu_B\mu_\alpha|\psi_\alpha(0)|^2/I, \tag{2.7}$$

where μ_α are the nuclear magnetic moments, and $|\psi_\alpha(0)|^2$ are the electronic densities at the positions of the nuclei.
The precession frequency in the quasi-static nuclear field δ_e and the dispersion of the nuclear hyperfine field distribution are linked as:

$$2\pi\hbar\delta_e = g_e\mu_B\Delta_B \tag{2.8}$$

It leads to:

$$\delta_e = \frac{1}{2\pi\hbar}\sqrt{\frac{I(I+1)}{12\pi a_B^3}v_0\sum_\alpha A_\alpha^2\rho_\alpha}, \tag{2.9}$$

All parameters entering Eqs. (2.9-2.7) are known (see Table 2.1), except $|\psi_{\mathrm{Te}}(0)|^2$ that we treat as a fitting parameter in order to reproduce $\delta_e = 2\pi \times 29 \pm 1\mathrm{MHz}$. It allows for the determination of the hyperfine constant for Te.

α	μ_α (in nuclear magneton)	ρ_α	$\lvert\psi_\alpha(0)\rvert^2$ (m^{-3})	A_α (μeV)
^{111}Cd	-0.59	0.12	5.3×10^{31} [7]	-31
^{113}Cd	-0.62	0.12	5.3×10^{31}	-32
^{125}Te	-0.888	0.08	$\mathbf{14.5 \times 10^{31}}$	**−96**

Table 2.1: Parameters used for the calculation of δ_e, with $a_B = 5.2$nm, and $g_e = -1.65$. The bold values are extracted from our results.

As a by-product we deduce the nuclear field at saturation $B_S = I\sum_\alpha A_\alpha\rho_\alpha/(g_e\mu_B) \simeq 0.094$ T. It is interesting to note that although B_S is about 50 times larger in GaAs than in CdTe, δ_e has almost the same value [8]. This is a consequence of the combined effect of smaller Bohr radius, and larger electron g-factor in CdTe compared to GaAs.

2.2.3 Evolution of the two-peaks structure with experimental conditions

The observation of the electron spin precession in the local quasi-static nuclear fields is quite surprising for a large donor concentration. In order to observe this effect, the electron spin correlation time at a given donor site must actually be longer than the Larmor period in the nuclear field. In other words $\delta_e > W_0$, which corresponds to $\tau_c > 30$ ns. This long correlation time is not expected at this doping level due to rapid spin exchange between neighbouring donors [1]. Thus, the assumption of a correlation time limited by the hopping is not supposed to be valid. In what follows, we therefore focus on what may govern the correlation time.

Influence of the probe power on W_0

Increasing the probe power broadens the central peak and the structure is less and less resolved. At high probe power, the presence of the satellite peaks is indicated by a slight distortion of the lorentzian shape of the central peak. Figure 2.6 depicts the evolution of SN spectra with the probe power.

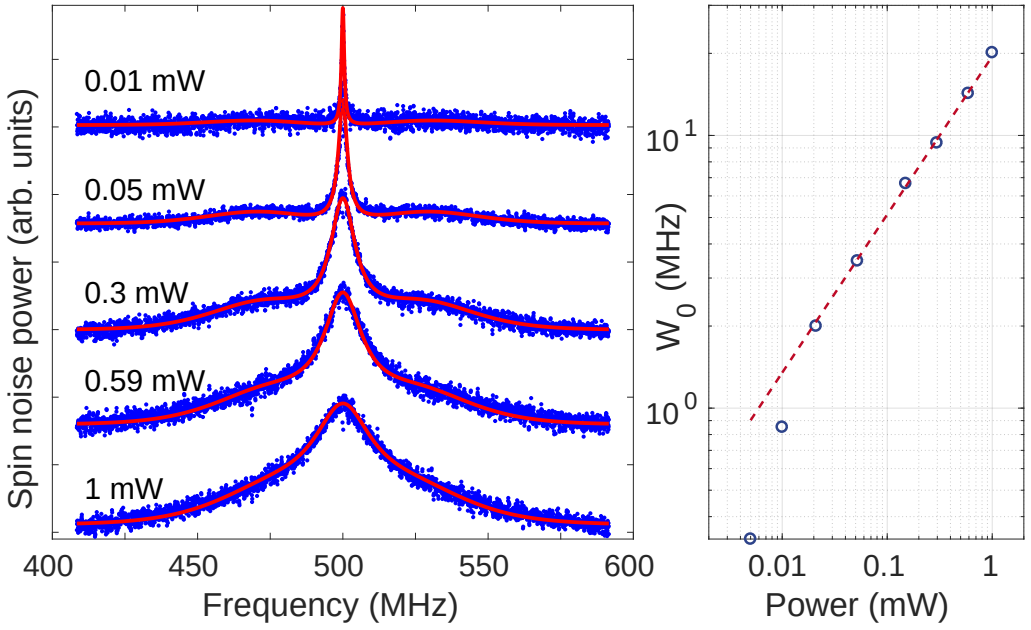

Figure 2.6: Left panel: Evolution of the SN with excitation power at $B = 0$ T (blue dots). Spectra are vertically shifted for clarity. Fit of the data with Glazov's model are shown in red solid lines. δ_e and ν_s are fixed and only W_0 varies. Experimental conditions: $T = 5.5$ K. Right panel: Evolution of extracted W_0 with P_{laser} (blue circles, log scale). Red dashed line has a slope of 0.6 to compare the power evolution of W_0 with P_{laser}.

This evolution is very well described by the model which takes into account both the

hyperfine interaction and the hopping. The only varying parameter is the hopping rate. Its increase with the probe power may be due to the laser heating and follows a power dependence ($W_0 \propto {P_{probe}}^{0.6}$).

Influence of the temperature on W_0

Increasing the temperature also broadens the central peak. Left panel of figure 2.7 depicts the evolution of SN spectra with temperature for $P_{probe} = 5$ μW.

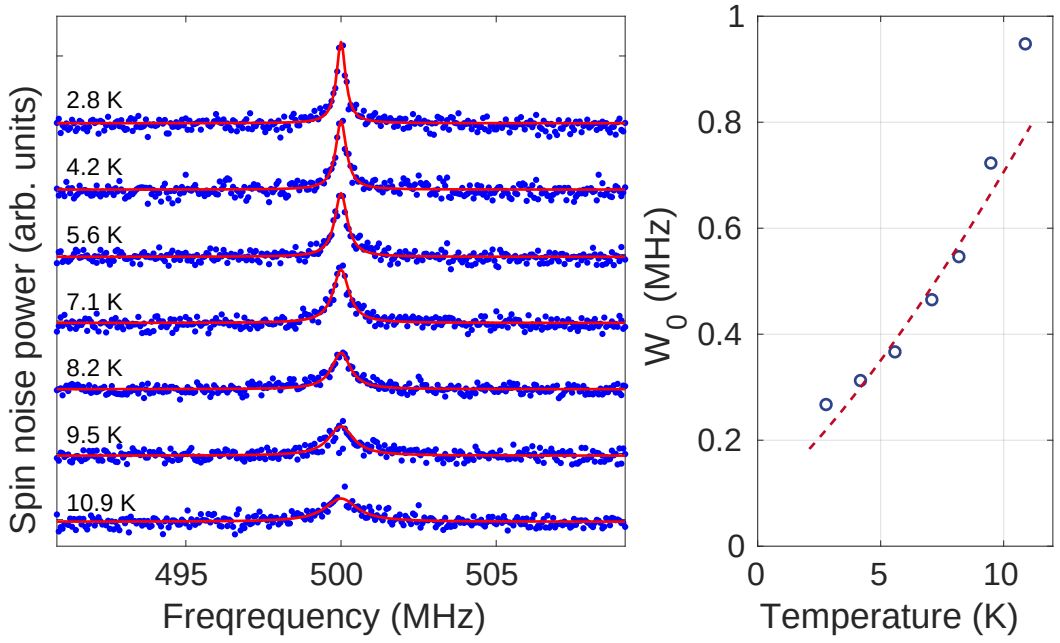

Figure 2.7: Left panel: Evolution of the SN with temperature at $B = 0$ T and low power excitation (blue dots). Spectra are vertically shifted for clarity. In these conditions, satellite peaks are indistinguishable and data are fit with a Lorentzian (red solid lines). W_0 is extracted from the width of the peak, considering $W_0 = 2/3\gamma_e$ (from equation 2.4 with $\nu_s = 0$). Experimental conditions: $P_{laser} = 5$ μW. Right panel: Evolution of extracted W_0 with temperature (blue circles, log scale). Red dashed line is a fit with the VRH model from euqation 2.10 corresponding to $N_D = 10^{17}$ cm^{-3}, $a = 250$nm and $T_0 = 270$ K. For the fit, T has been offseted by 2 K which is not surprising for a cold-finger cryostat.

At this very low probe power, the two-peaks structure is not visible because satellites are much broader than the zero-frequency line and therefore have a much weaker amplitude. The linewidth of the central peak is determined by the relaxation of the spin component in the direction of the local nuclear field. At the lowest temperature, we obtained the spin relaxation time $T_1 = (2\pi\gamma_e)^{-1} = 0.8$ μs.

Interpretation in the framework of the VRH model

Due to its small thickness, our layer is presumably largely depleted. This can inhibit the spin exchange mechanism. The spin correlation time in this case could be limited by the hopping of the electron from an occupied donor to an unoccupied one. This situation is, in principle, described by the variable range hopping mechanism.
Assuming the linewidth is limited by W_0 ($\nu_s = 0$), we can follow the evolution of the hopping rate with the temperature. In the variable range hopping model, $\tau_{\text{hop}} = W_0^{-1}$ can be estimated from the optimal hopping distance R_{opt} and from the diffusion coefficient D_{hop} by using $\tau_{\text{hop}} = R_{\text{opt}}^2/6D_{\text{hop}}$. A lower bound for D_{hop} can be estimated by using the Einstein relation $D_{\text{hop}} = k_B T \sigma_{\text{hop}}/N_D e^2$, where σ_{hop} is the hopping conductivity, and one assumes that the maximum carrier density given by N_D participates to the conductivity. Using the Mott formula for the conductivity one finds

$$\tau_{\text{hop}}^{-1} = \frac{\nu_H}{9\pi a^3 N_D} \left(\frac{T}{T_0}\right) e^{-(T_0/T)^{1/4}} \tag{2.10}$$

where a is the localization length and ν_H is the characteristic frequency of longitudinal optical phonon. Far from the Mott transition a tends towards the effective Bohr radius of the donor, while close to the MIT a diverges due to the weakening of the carriers localization.
The right panel of figure 2.7 displays the experimentally measured hopping rate W_0 fitted to equation 2.10. The main unknowns are T_0, and a, which vary rapidly with N_D close to the MIT (other parameters are $\nu_H = 5\text{THz}$, and $N_D \sim 10^{17}\text{cm}^{-3}$).
The best fit yields the combination of parameters $a = 250$ nm and $T_0 = 270$ K, which agrees reasonably well with the values determined by conductivity and magnetotransport experiments [12]. However, the obtained localisation length is not compatible with the observation of the nuclear field.

2.3 Conclusion

In the end, we observed spin noise in CdTe for the first time. At low temperature and low excitation power, we measured longitudinal electron spin relaxation time up to $T_1 = 0.8$ μs which is not an absolute limit since longer relaxation time up to ≈ 1 ms have been measured in CdTe at lower doping density, and lower temperatures [13]. We have also been able to report the observation of the electron precession in the random nuclear field. We obtained spin relaxation time $\tau_s = 1/\delta_e \approx 5.5$ ns which correspond to the precession in a quasi-frozen nuclear field. In their work, Merkulov et al. have also predicted a second time scale for the spin relaxation due to the slow

precession of the nuclei in the knight field of electrons [4]. This longer time $\tau_{s,N}$ can be estimated as $\tau_{s,N} \approx \sqrt{N}\tau_s = 4\ \mu$s which is comparable to the measured T_1 time.

However, the observation of this precession in the ramdom nuclear field is quite intriguing and the signal is attributed to localised electrons with long correlation time. This is in direct contradiction with our expectations. An analogy with the observation of such an effective field in GaAs leads us to consider two different contributions to the conduction [6]. A first channel comes from creation of filament via percolation. This leads to a metallic conduction characterised by a high diffusion coefficient. The second conduction channel comes from the hopping between donors and is characterised by a small diffusion coefficient.

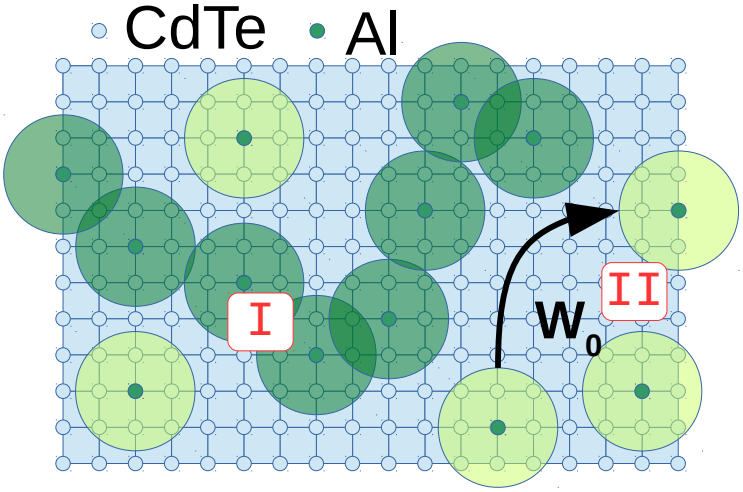

Figure 2.8: Two different conduction channels. I: electrons have a metallic behaviour in randomly arranged conducting filaments. II: electrons hop from one donor to an other and have a weaker diffusion coefficient.

This interesting idea implicates that signal comes only from localised electrons. Therefore, the following question remains an outstanding issue: why metallic electrons do not contribute to the signal?

At this stage of our analysis, this issue echoes another question. We actually knew that SNS should be able to probe spatial spin dynamics and that spin diffusion is expected to affect the signal in a particular configuration [14, 15] which implies to probe SN at non-zero wave vectors. Besides, if this assumption is confirmed, our backscattering configuration seems to correspond to the more sensitive configuration.

* *
*

It clearly appears that a complete understanding of the link between the spatial spin dynamics and spin noise spectra is necessary. We therefore focus our efforts to make it clear. The next chapter is dedicated to the experimental development of a wave vector sensitive spin noise setup, the demonstration of our abilities to reach both spatial and temporal spin correlations and to a deeper study of SN in n-CdTe.

Bibliography

[1] RI Dzhioev, KV Kavokin, VL Korenev, MV Lazarev, B Ya Meltser, MN Stepanova, BP Zakharchenya, D Gammon, and DS Katzer. Low-temperature spin relaxation in n-type gaas. *Physical Review B*, 66(24):245204, 2002. [2.1, 2.2.3]

[2] KV Kavokin. Spin relaxation of localized electrons in n-type semiconductors. *Semiconductor Science and Technology*, 23(11):114009, 2008. []

[3] VV Belykh, KV Kavokin, DR Yakovlev, and M Bayer. Electron charge and spin delocalization revealed in the optically probed longitudinal and transverse spin dynamics in n-gaas. *Physical Review B*, 96(24):241201, 2017. [2.1]

[4] I. A. Merkulov, Al. L. Efros, and M. Rosen. Electron spin relaxation by nuclei in semiconductor quantum dots. *Phys. Rev. B*, 65:205309, 2002. [2.1, 2.2.2, 2.3]

[5] K_V Kavokin. Anisotropic exchange interaction of localized conduction-band electrons in semiconductors. *Physical Review B*, 64(7):075305, 2001. [2.1]

[6] Jan G Lonnemann, Eddy P Rugeramigabo, Michael Oestreich, and Jens Hübner. Closing the gap between spatial and spin dynamics of electrons at the metal-to-insulator transition. *Physical Review B*, 96(4):045201, 2017. [2.1, 2.3]

[7] A Nakamura, D Paget, C Hermann, C Weisbuch, G Lampel, and BC Cavenett. Optical detection of electron spin resonance in cdte. *Solid State Communications*, 30(7):411–414, 1979. [2.1, 2.2.2]

[8] Fabian Berski, Jens Hübner, Michael Oestreich, Arne Ludwig, AD Wieck, and Mikhail Glazov. Interplay of electron and nuclear spin noise in n-type gaas. *Physical review letters*, 115(17):176601, 2015. [2.2.2, 2.2.2]

[9] DS Smirnov, MM Glazov, and EL Ivchenko. Effect of exchange interaction on the spin fluctuations of localized electrons. *Physics of the Solid State*, 56(2):254–262, 2014. [2.2.2]

[10] MM Glazov. Spin noise of localized electrons: Interplay of hopping and hyperfine interaction. *Physical Review B*, 91(19):195301, 2015. [2.2.2, 2.5, 2.2.2, 2.2.2]

[11] Anatole Abragam and Anatole Abragam. *The principles of nuclear magnetism*. Number 32. Oxford university press, 1961. [2.2.2]

[12] NV Agrinskaya. Low temperature variable range hopping conductivity in doped cdte crystals. *Journal of crystal growth*, 138(1-4):493–498, 1994. [2.2.3]

[13] Xiayu Linpeng, Todd Karin, MV Durnev, Russell Barbour, MM Glazov, E Ya Sherman, SP Watkins, Satoru Seto, and Kai-Mei C Fu. Longitudinal spin relaxation of donor-bound electrons in direct band-gap semiconductors. *Physical Review B*, 94(12):125401, 2016. [2.3]

[14] GG Kozlov, II Ryzhov, and VS Zapasskii. Light scattering in a medium with fluctuating gyrotropy: Application to spin-noise spectroscopy. *Physical Review A*, 95(4):043810, 2017. [2.3]

[15] GG Kozlov, II Ryzhov, and VS Zapasskii. Spin-noise spectroscopy of randomly moving spins in the model of light scattering: Two-beam arrangement. *Physical Review A*, 97(1):013848, 2018. [2.3]

Chapter 3

Experimental development of q-sensitive SNS

Contents

This chapter is dedicated to the experimental development of a q-sensitive spin noise setup enabling to reach both spatial and temporal spin correlations. The first section reminds the scientific context in which we pursued this objective, the physical principles on which this idea relies and our general motivation. Then, the technical implementation of such a setup is introduced and the setup is validated with proof-of-concept measurement of spin diffusion in n-CdTe. Finally, we come back to the investigation of the spin dynamics in n-CdTe thin layers with this brand new tools.

3.1 Scientific context and motivations

The experimental development of a q-sensitive SNS setup presented in this chapter comes after a long process which finds its source in the very stimulating scientific context surrounding the research about spin noise spectroscopy. This first section is dedicated to set the scene of this process.

Context

As discussed in section 1.2.1, there are two possible interpretations of the origin of the SN signal, the spin Faraday rotation and the spin flip Raman scattering being two sides of the same coin [1–3].

The spin Faraday rotation being proportional to the average spin density below the spot, all spatial information is usually lost. Some experimental works have considered spatial spin dynamics in the interpretation of SN measurements [4, 5], but a direct access to spatial information via SN has only been theoretically investigated. In 2013, Pershin *et al.* have proposed a two-beams setup providing spin transport information through the correlations between SN probed at different space locations [6] but no experimental implementation have been realised since then.

The SFRS vision opens up great opportunities to access spatial information. In SFRS, information carried by the scattered light actually depends on its wave vector and this should be transposable to SNS.
In this regard, a two-beams configuration has recently been proposed to introduce a wave vector difference q between the probe and the LO [7, 8]. In this proposal, the q-selectivity is provided by means of a slight tilt between the probe beam and an LO passing through the sample. Thus, interferences are only allowed between the LO and the q-component of the scattered light.
This work predicts a broadening of the SN with increasing q in presence of spin diffusion. Indeed, the complete picture of the spatio-temporal spin dynamics is given by the Bloch-Torrey equation [9, 10]:

$$\frac{\partial \vec{\mathcal{S}}}{\partial t} = \vec{\mathcal{S}} \wedge \vec{\omega_L} - \gamma_s \vec{\mathcal{S}} + D_s \Delta \vec{\mathcal{S}} \tag{3.1}$$

and we can express the generalised spin susceptibility as

$$\chi(\omega, q) \propto \frac{1}{2\pi(\omega - \omega_L) + i(\gamma_s + D_s q^2)} \tag{3.2}$$

Because the fluctuation-dissipation theorem ensures the ω and q dependent spin noise is proportional to the imaginary part of the generalised spin susceptibility $\chi(\omega, q)$, we can expect a broadening of the SN with q:

$$\gamma(q) = \gamma_s + D_s q^2 \tag{3.3}$$

where γ is the width of the SN measured at a wave vector difference q between the probe beam and the LO.

Emergence of the idea

From the very beginning of spin noise spectroscopy, the origin of the signal has been understood as the interference between the incident and the scattered fields [11]. Such interferences could occur in the sample and then be imaged onto the detector. They can also occur directly onto the detector. In this case, an LO is sent directly to the detector to interfere with the scattered light. This distinguishes the *self-homodyne* and the *homodyne* detection and provides very interesting opportunities. Optical properties of the LO can actually be changed. For instance, its power can be adjusted to exceed the noise equivalent power of the dectector [12–14]. Its wavelength as well can be modified providing optical heterodyning and thus improving the bandwidth of the setup [12]. Here we propose to take advantage of this configuration to modify the wave vector of the LO onto the detector. This should allow for a wave vector selectivity in the interference with the scattered light.

Motivations

This very recent investigation on spatial information via SNS had strongly impacted our scientific approach. On the one hand, we usually work in backscattering configuration so the problem of diffusion may occur in its most glaring face: this configuration seems to correspond to the highest value of q, thus the largest broadening due to spin diffusion. However, there are still no clues of this broadening in any of our measurements.

On the other hand, our intriguing results on CdTe have led us to consider the influence of diffusion on the SN signal. As a matter of fact, a broadening due to diffusion could explain why we detect only localised electrons and not free electrons with high diffusion coefficient.

With this in mind, we also modified our setup to perform measurements in forward geometry and received three new samples. They differ from other samples by their width but especially by their substrate. They are grown onto a $Cd_{0.96}Zn_{0.04}Te$ sub-

strate which is transparent at working wavelength (see table 3.1).

Besides these immediate considerations, two more distant motivations encourage us to follow this direction. First, it is an old goal in our team to perform SNS measurement with light scattered at ninety degrees. In analogy with SFRS, it is actually expected to allow for reaching independently the two spin subpopulations. However, a potential broadening proportional to q^2 does not augur well.
Then, the possibility of detecting spatial correlations is quite interesting for the study of collective states. The observation of spin noise of indirect excitons and even more detection of their potential condensation (which are also in the scope of this work) should be a remarkable breakthrough. Spatial spin correlations in 2DEG have also been predicted [15], especially in the regime of persistent spin helix, and could be studied with our technique.

* *
*

It was only natural to focus our research on the detection of SN at non-zero wave vector. It should allow us to better understand what we measured, to check the influence of the diffusion on SN and to considerably extend the opportunities of SNS. The next section is dedicated to the experimental development of a q-sensitive SNS setup allowing such a scientific investigation.

3.2 Implementation of a spatio-temporal SNS setup

3.2.1 Setup

The experimental development presented here has required a remarkable versatility which led us to modify the setup used in the last chapter.
The first significant modification consists in adding the possibility to perform spin noise measurements in transmission geometry. We therefore added a second collection objective on the other side of the cryostat. The two objectives are identical (long working distance Mitutoyo objectives with NA=0.28). The two different paths merge at the PBS2 providing the preservation of the detection scheme when switching from one configuration to the other. The linear polarisation of the scattered light being vertical, the forward scattered light must pass through a $\lambda/2$ plate to get across the PBS2. The LCM1 is positioned just after the PBS2. It allows for adjusting the polarisation of the scattered light: the LO being vertically polarised, the LCM1 is used in forward scattering while it is not in backward scattering. It is also used to modulate the polarisation which provides an alternative to remove the background

noise.

The second modification concerns the path of the LO. We disabled the possibility to change its frequency. We are therefore restricted to the (self-)homodyne detection. The LO is picked from the initial laser beam at the PBS1. It goes through a prism which determines its position ρ_0 providing the q-selectivity.

Finally, an active phase stabilisation has been introduced to control the relative phase ϕ between the LO and the probe. It consists in a regulation scheme controlling a piezo-actuator on which the prism is mounted. This abilities to tune ϕ will be necessary to test our understanding of how the setup operates.

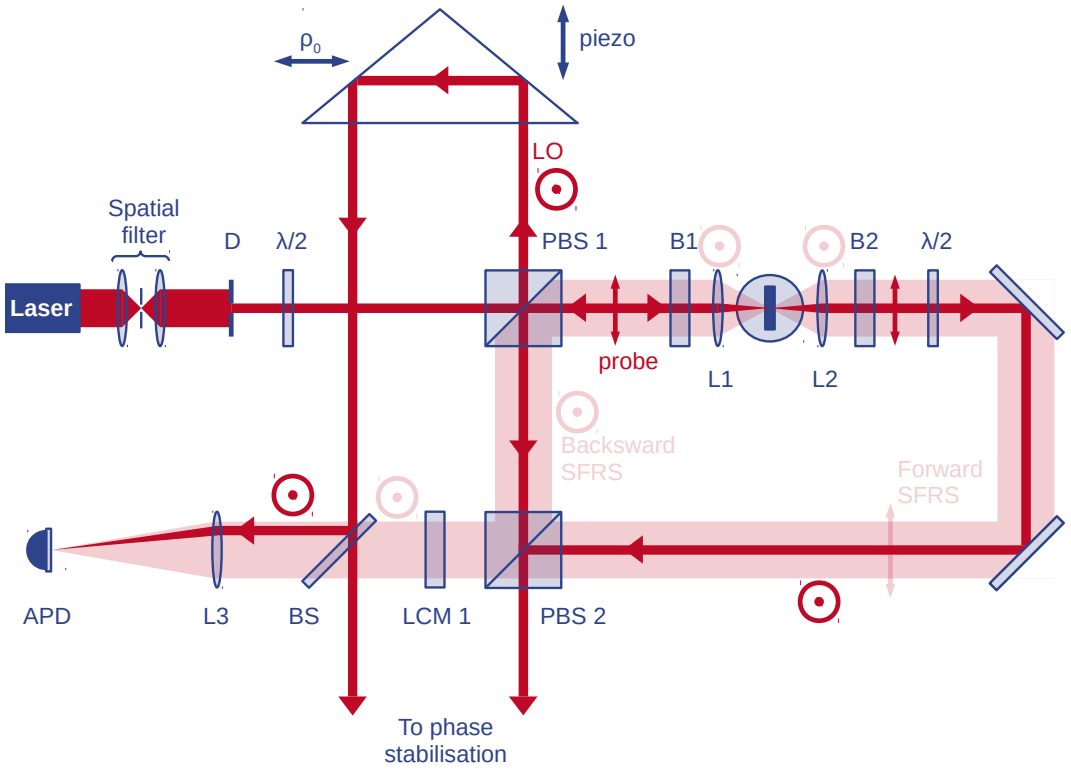

Figure 3.1: Schematics of our modified spin noise setup. Both backward and forward scattered light can be collected. The wave vector of the LO is controlled through the position of the prism. The position of this prism controls also its relative phase with respect to the probe which is actively stabilised.

The LO and the scattered light are then recombined at the beam splitter BS (which reflects 10% of the incident light) and are focused on the detector by the imaging lens L3. An important feature of this setup is that the beam paths of the LO and the probe are adjusted to cancel the quadratic phase shifts due to the propagation. In this configuration, undesirable background noise can be removed either by measuring the noise spectra at two different magnetic fields, or by changing the polarisation of the scattered light with LCM1.

3.2.2 Optical transfer function of the setup

Using this setup, we performed preliminary spin noise measurements varying the position ρ_0 of the LO. Contrary to our initial expectations, the signal does not differ only by its width but its integrated intensity also decreases when the LO is shifted (see figure 3.3). Different potential causes could explain this behaviour. We have considered for instance a wave-front distortion or interferences into the detector. Among them, we first incriminated the optical response of our setup and decided to characterise it.

We temporarily introduced a mirror in the path of the LO and the scattered light to redirect them to a CCD. This enables us to observe the evolution of their interference patterns. Figure 3.2 displays such interference pattern for different offsets up to $\rho_0 = 5.3$ mm and their corresponding spatially integrated intensity. We still observe a very good contrast even at the highest offset which indicates that there is no unwanted wavefront distorsions induced by the setup or the sample itself.

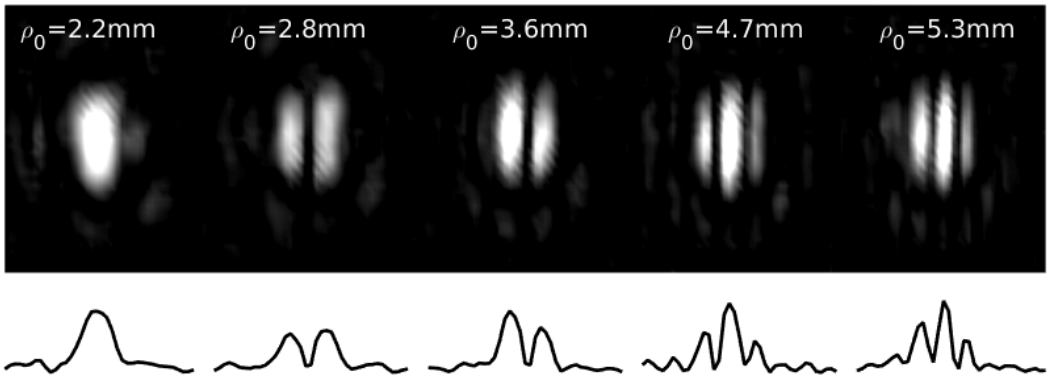

Figure 3.2: Interference patterns for different offsets ρ_0v recorded with a CCD camera and their spatially integrated intensity.

A more quantitative approach consists in using the APD to measure the variation of the amplitude of these interferences with ρ_0. To do this, we use a probe beam as broad as the objective aperture and we translate the narrow LO. The detector follows the LO movement. The relative phase ϕ is modulated in order to observe the intensity of the oscillations of the interference. We then measure the amplitude of these oscillations.

Figure 3.3 shows the variation of the measured amplitude with ρ_0. Contrary to the evolution of the SN signal, we observe a flat response on a wide range of ρ_0. The abrupt cut-off around $\rho_0 = 5.5$ mm is due to the objective aperture. The edges of this function are smoothed due to the LO finite size. The dashed line represents an ideal coherent optical transfer function on a finite ρ_0-range (corresponding to the objective aperture) convolved with a simplistic beam shape (uniform disk of 2.4 mm

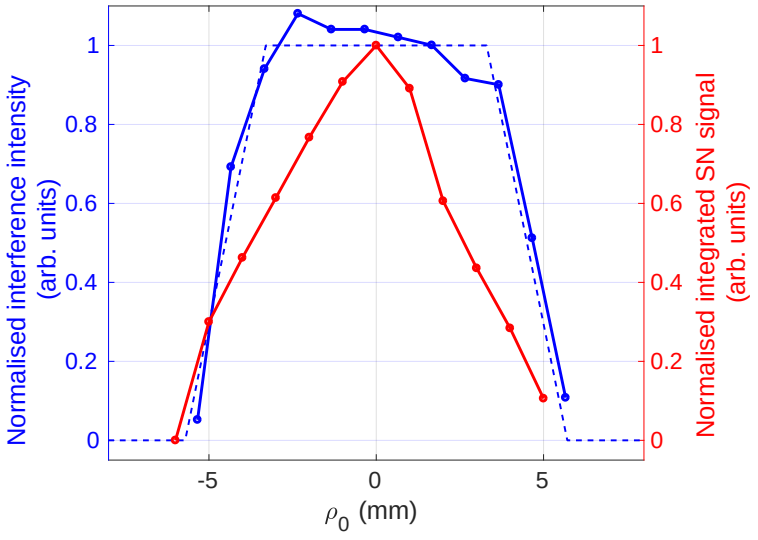

Figure 3.3: Normalised integrated SN signal (red line) and amplitude of the interferences between the LO and the probe beam (blue line) for different LO positions. The dashed line represents a rectangular function convolved with the finite size of the beam.

diameter).

This observation definitively exonerates the quality of the setup. The decrease of the integrated spin noise power with q is actually intrinsically linked with the limited spatial resolution of our optical setup which is considered in the next section.

3.2.3 How spatial correlations can be detected by SNS

In what follows, we clarify the origin of the SN signal and demonstrate that we can probe the Fourier component of the scattered light. It allows for a more thoughtful consideration of what modifies the SN signal when we change ρ_0.

Imaging of the scattered light onto the detector

Let's consider the following situation: the scattered light is collected by a short focal length objective and sent to the detector where it is focused by a longer focal length imaging lens. This field comes from the interaction between the probe field E_0 and spin fluctuations which are described by the spatially dependent gyrotropy G. It can be expressed as:

$$E_s(\boldsymbol{r}) = E_0(\boldsymbol{r})G(\boldsymbol{r}) \tag{3.4}$$

where $\boldsymbol{r}$ determines the position in the sample plane. We now follow the evolution of this field from the sample to the detector. In the image focal plane of the collection

objective, the scattered field is the Fourier transform of $E_s(\boldsymbol{r})$:

$$\hat{E}_s(\boldsymbol{\rho}) = \int E_0(\boldsymbol{r})G(\boldsymbol{r})e^{i\frac{k}{f}\boldsymbol{r}\cdot\boldsymbol{\rho}}d^2\boldsymbol{r} \tag{3.5}$$

where k is the wave number of this field, f is the focal length of the objective and $\boldsymbol{\rho}$ is the position in the image focal plane of the objective.
The propagation of the collimated scattered field from the objective image focal plane to the object focal plane of the imaging lens is governed by the Fresnel propagator. There, the field is:

$$\hat{E}_s^d(\boldsymbol{\rho}') = (\hat{E}_s \otimes \hat{H}_d)(\boldsymbol{\rho}') = \int \hat{H}_d(\boldsymbol{\rho}' - \boldsymbol{\rho})\hat{E}_s(\boldsymbol{\rho})d^2\boldsymbol{\rho} \tag{3.6}$$

where $\boldsymbol{\rho}'$ is the position in the object focal plane of the imaging lens. $\hat{H}_d(\boldsymbol{\rho})$ is the Fresnel propagator over the distance d between the two focal planes and is given by:

$$\hat{H}_d(\boldsymbol{\rho}) = \frac{e^{ikd}}{i\lambda d}e^{i\frac{k}{2d}\boldsymbol{\rho}^2} \tag{3.7}$$

Finally, the scattered field onto the detector - in the image focal plane of the imaging lens - is given by the Fourier transform of this field:

$$\mathcal{E}_s(\boldsymbol{r}') = \int (\hat{E}_s \otimes \hat{H}_d)(\boldsymbol{\rho}')e^{i\frac{k}{f'}\boldsymbol{\rho}'.\boldsymbol{r}'}d^2\boldsymbol{\rho}' = H_d(\boldsymbol{r}')E_s(-\frac{f}{f'}\boldsymbol{r}') \tag{3.8}$$

where $\boldsymbol{r}'$ is the position in the image focal plane of the imaging lens that means onto the detector. Here, f' is the focal length of the imaging lens and $H_d(\boldsymbol{r}')$ is given by:

$$H_d(\boldsymbol{r}') = \int \hat{H}_d(\boldsymbol{\rho})e^{i\frac{k}{f'}\boldsymbol{\rho}.\boldsymbol{r}'}d^2\boldsymbol{\rho} = -e^{ikd}e^{i\frac{kd}{2f'^2}|\boldsymbol{r}'|^2} \tag{3.9}$$

The spatial distribution of the field from the sample is therefore imaged onto the detector with a magnification $-f'/f$ and an additional radial phase due to the propagation.

Origin of the spin noise signal

Before the mixing of the LO and the scattered field in the beam splitter, the LO beam can be adjusted in order to have the same radial phase at the object focal plane of the lens. This situation could be guaranteed by obtaining a flat interference pattern (one can use a CCD for instance). It can therefore be expressed as the

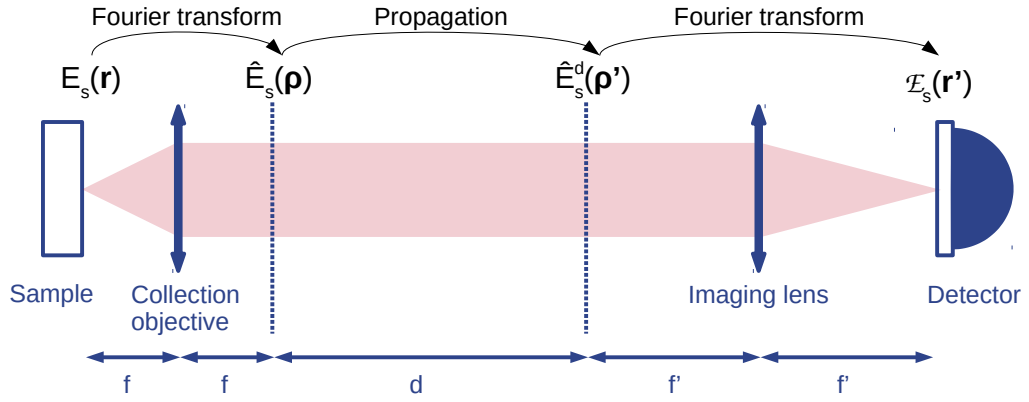

Figure 3.4: Imaging scheme of the scattered field onto the detector. It is first Fourier transformed by the collection objective, it then propagates up to the imaging lens where it is again Fourier transformed.

scattered light in equation 3.6:

$$\hat{E}^d_{LO}(\boldsymbol{\rho}') = (\hat{E}_{LO} \otimes \hat{H}_d)(\boldsymbol{\rho}') = \int \hat{H}_d(\boldsymbol{\rho}' - \boldsymbol{\rho})\hat{E}_{LO}(\boldsymbol{\rho})d^2\boldsymbol{\rho} \tag{3.10}$$

and the same reasoning gives its expression onto the detector:

$$\mathcal{E}_{LO}(\boldsymbol{r}') = H_d(\boldsymbol{r}')E_{LO}(-\frac{f}{f'}\boldsymbol{r}') \tag{3.11}$$

Finally, the total light intensity is spatially integrated by the detector which delivers an electrical signal:

$$I_D = \int \left(|\mathcal{E}_s(\boldsymbol{r}')|^2 + |\mathcal{E}_{LO}(\boldsymbol{r}')|^2 + 2\mathcal{R}e\{\mathcal{E}_s(\boldsymbol{r}')\mathcal{E}^*_{LO}(\boldsymbol{r}')\}\right)\ d^2\boldsymbol{r}' \tag{3.12}$$

The first term is negligible and the informative signal S_D comes from the third term:

$$S_D = \mathcal{R}e\{\int \mathcal{E}_s(\boldsymbol{r}')\mathcal{E}^*_{LO}(\boldsymbol{r}')\ d^2\boldsymbol{r}'\} = (\frac{f}{f'})^2\mathcal{R}e\{\int E_0(\boldsymbol{r})E^*_{LO}(\boldsymbol{r})G(\boldsymbol{r})d^2\boldsymbol{r}\} \tag{3.13}$$

Here, we precisely understand how powerful the use of LO really is: everything happens as if the LO interacts with the sample. If $E_0(\boldsymbol{r})$ and $E_{LO}(\boldsymbol{r})$ are identical, the measured spin noise corresponds to the homodyne detection. If the $\boldsymbol{r}$-dependence of the LO amplitude is sharper than the one of $E_0(\boldsymbol{r})$, it is possible to use the LO as a spatial probe of spin fluctuations. But what we are concerned with here is the access to Fourier components of these spin fluctuations.

LO as a wave vector selector

Let's now consider an LO with the same phase and amplitude as the incident beam (for instance they can be picked from the same laser beam and have the same propagation length). It is possible to introduce a spatial offset between the LO and the scattered light:

$$\hat{E}^d_{LO}(\boldsymbol{\rho}') = \hat{E}^d_{LO}(\boldsymbol{\rho}' - \boldsymbol{\rho_0}) \tag{3.14}$$

We can follow the same reasoning as earlier and finally obtain:

$$\mathcal{E}_{LO}(\boldsymbol{r}') = H_d(\boldsymbol{r}')E_{LO}(-\frac{f}{f'}\boldsymbol{r}')e^{-i\frac{k}{f}\boldsymbol{\rho_0}.\frac{f}{f'}\boldsymbol{r}'} \tag{3.15}$$

for the LO field in the detector field and the expression of the signal from the detector:

$$S_D = (\frac{f}{f'})^2\mathcal{R}e\{\int I_0(\boldsymbol{r})G(\boldsymbol{r})e^{-i\boldsymbol{q}\boldsymbol{r}}d^2\boldsymbol{r}\} \tag{3.16}$$

where $\boldsymbol{q} = \frac{k}{f}\boldsymbol{\rho_0}$. It is important to note that S_D varies because of the time dependence of G which is our interest.

We now focus on the correlation function of the measured signal $C_D(\tau) = \langle S_D(t)S_D(t+\tau)\rangle$.

$$C_D(\tau) = \langle(\frac{f}{f'})^2\int I_0(\boldsymbol{r})G(\boldsymbol{r},t)cos(\boldsymbol{q}\boldsymbol{r})d^2\boldsymbol{r} \times (\frac{f}{f'})^2\int I_0(\boldsymbol{r}')G(\boldsymbol{r}',t+\tau)cos(\boldsymbol{q}\boldsymbol{r})d^2\boldsymbol{r}'\rangle \tag{3.17}$$

Rearranging the terms and performing the average only on time dependent terms, we obtain:

$$C_D(\tau) = (\frac{f}{f'})^4\int I_0(\boldsymbol{r})cos(\boldsymbol{q}\boldsymbol{r})\int I_0(\boldsymbol{r}')cos(\boldsymbol{q}\boldsymbol{r}')\left\langle G(\boldsymbol{r},t)G(\boldsymbol{r}',t+\tau)\right\rangle d^2\boldsymbol{r}d^2\boldsymbol{r}' \tag{3.18}$$

If we note $K(\boldsymbol{r},\tau) = \langle G(\boldsymbol{r}',t')G(\boldsymbol{r}'+\boldsymbol{r},t'+\tau)\rangle$ the correlation function of the gyrotropy, the last equation becomes:

$$C_D(\tau) \propto \int I_0(\boldsymbol{r})cos(\boldsymbol{q}\boldsymbol{r})\left[\int I_0(\boldsymbol{r}')cos(\boldsymbol{q}\boldsymbol{r}')K(\boldsymbol{r}-\boldsymbol{r}',\tau)d^2\boldsymbol{r}'\right]d^2\boldsymbol{r} \tag{3.19}$$

The bracketed integrals is the Fourier transform of the product $I_0(\boldsymbol{r}')K(\boldsymbol{r}'-\boldsymbol{r})$ thus it is proportionnal to the convolution product of the Fourier transform of $I_0(r')$ and $K(\boldsymbol{r}'-\boldsymbol{r})$, denoted respectively as $\hat{I}_0(\boldsymbol{q}')$ and $cos(\boldsymbol{q}.\boldsymbol{r})\hat{K}(\boldsymbol{q}')$, taken for $\boldsymbol{q}' = \boldsymbol{q}$. The factor $cos(\boldsymbol{q}\boldsymbol{r})$ appears due to the translation of $\hat{K}(\boldsymbol{r}')$ by the vector $\boldsymbol{r}$. We thus

have:

$$C_D(\tau) \propto \int I_0(\boldsymbol{r}) cos(\boldsymbol{qr}) \left[\int \hat{I}_0(\boldsymbol{q'}) cos((\boldsymbol{q}-\boldsymbol{q'})\boldsymbol{r}) \hat{K}(\boldsymbol{q}-\boldsymbol{q'},\tau) d^2\boldsymbol{q'} \right] d^2\boldsymbol{r} \tag{3.20}$$

or equivalently:

$$C_D(\tau) \propto \int I_0(\boldsymbol{r}) cos(\boldsymbol{qr}) \left[\int \hat{I}_0(\boldsymbol{q}-\boldsymbol{q'}) cos(\boldsymbol{q'r}) \hat{K}(\boldsymbol{q'},\tau) d^2\boldsymbol{q'} \right] d^2\boldsymbol{r} \tag{3.21}$$

Inverting the integrals in real and reciprocal spaces, one gets:

$$C_D(\tau) \propto \int \hat{K}(\boldsymbol{q'},\tau) \hat{I}_0(\boldsymbol{q}-\boldsymbol{q'}) \left[\int \hat{I}_0(\boldsymbol{r}) cos(\boldsymbol{qr}) cos(\boldsymbol{q'r}) d^2\boldsymbol{r} \right] d^2\boldsymbol{q'} \tag{3.22}$$

$$\propto \int \hat{K}(\boldsymbol{q'},\tau) \hat{I}_0(\boldsymbol{q}-\boldsymbol{q'}) \left[\int \hat{I}_0(\boldsymbol{r}) cos((\boldsymbol{q}+\boldsymbol{q'})\boldsymbol{r}) cos((\boldsymbol{q}-\boldsymbol{q'})\boldsymbol{r}) d^2\boldsymbol{r} \right] d^2\boldsymbol{q'} \tag{3.23}$$

$$\propto \int \hat{K}(\boldsymbol{q'},\tau) \hat{I}_0(\boldsymbol{q}-\boldsymbol{q'}) \left[\hat{I}_0(\boldsymbol{q}-\boldsymbol{q'}) + \hat{I}_0(\boldsymbol{q}+\boldsymbol{q'}) \right] d^2\boldsymbol{q'} \tag{3.24}$$

Developing this equation, it comes:

$$C_D(\tau) \propto \int \hat{K}(\boldsymbol{q'},\tau) \hat{I}_0^2(\boldsymbol{q}-\boldsymbol{q'}) d^2\boldsymbol{q'} + \int \hat{K}(\boldsymbol{q'},\tau) \hat{I}_0(\boldsymbol{q}-\boldsymbol{q'}) \hat{I}_0(\boldsymbol{q}+\boldsymbol{q'}) d^2\boldsymbol{q'} \tag{3.25}$$

which we can factorise by $(\hat{K} \otimes \hat{I}_0^2)(\boldsymbol{q},\tau)$ and express as:

$$C_D(\tau) = (\hat{K} \otimes \hat{I}_0^2)(\boldsymbol{q},\tau)(1 + V_\tau(\boldsymbol{q})) \tag{3.26}$$

where

$$V_\tau(\boldsymbol{q}) = \frac{\int \hat{K}(\boldsymbol{q'},\tau) \hat{I}_0(\boldsymbol{q}-\boldsymbol{q'}) \hat{I}_0(\boldsymbol{q}+\boldsymbol{q'}) d^2\boldsymbol{q'}}{\int \hat{K}(\boldsymbol{q'},\tau) \hat{I}_0^2(\boldsymbol{q}-\boldsymbol{q'}) d^2\boldsymbol{q'}} \tag{3.27}$$

For gaussian beams $\hat{I}_0(\boldsymbol{q}-\boldsymbol{q'})\hat{I}_0(\boldsymbol{q}+\boldsymbol{q'})$ becomes $\hat{I}_0^2(\boldsymbol{q'})\hat{I}_0^2(\boldsymbol{q})$ and we can express $C_D(\tau)$ as:

$$C_D(\tau) = (\hat{K} \otimes \hat{I}_0^2)(\boldsymbol{q},\tau) + \hat{I}_0^2(\boldsymbol{q})(\hat{K} \otimes \hat{I}_0^2)(\boldsymbol{0},\tau) \tag{3.28}$$

This notation allows for the identification of two contributions. The first one is $\boldsymbol{q}$-dependent and contains all the information we are interested in. Excluding the $\hat{I}_0^2(\boldsymbol{q}$, the second term corresponds to $\boldsymbol{q} = 0$ and is non null as long as the LO and the probe overlap. Thus it could inform on the shape of the beam.
It is also interesting to consider an arbitrary phase ϕ between the LO and the probe. In this case, the second term in equations 3.26 and 3.28 are affected by a factor $cos(2\phi)$. It provides the opportunity to remove this $\boldsymbol{q} = 0$ contribution if we stabilise the relative phase at $\phi = \pi/4$ or if we average at 0 this term with a randomly fluctuating phase.

Inclusion of the optical transfer function of the setup

An ultimate step is needed to completely understand the evolution of the measured spin noise signal when the wave vector varies. We need to take into account the finite size of the lens performing the Fourier transformations of the scattered light. Because of their respective size, we will only take into account the collection objective.
It is common to use the pupil function $\hat{P}(\boldsymbol{\rho})$ to describe this effect and to multiply it with the field in the image focal plane of the objective $\hat{E}_s(\boldsymbol{q})$.
This modifies the expression of the scattered field onto the detector:

$$\mathcal{E}_s(\boldsymbol{r}') = H_d(\boldsymbol{r}')(E_s \otimes P)(-\frac{f}{f'}\boldsymbol{r}') \tag{3.29}$$

with

$$\hat{P}(\boldsymbol{\rho}) = \int P(\boldsymbol{r}) e^{i\frac{k}{f}\boldsymbol{\rho}.\boldsymbol{r}} d^2\boldsymbol{r} \tag{3.30}$$

The field onto the detector is therefore the convolution of the scattered field from the sample and the point spread function $P(\boldsymbol{r})$.
Following the same reasoning than earlier, equation 3.26 remains valid if we replace $\hat{K}(\boldsymbol{\rho})$ with $\hat{\kappa}(\boldsymbol{\rho})$ which is the Fourier transform of $\kappa(\boldsymbol{r}-\boldsymbol{r}') = \langle GG\rangle \otimes [PP]$.

$$C_D(\tau) = (\hat{\kappa} \otimes \hat{I}_0^2)(\boldsymbol{q},\tau)(1 + cos(2\phi)V_\tau(\boldsymbol{q})) \tag{3.31}$$

This equation is the general expression of the measured signal when we take into account the finite resolution of the imaging setup via the OTF.

With the benefit of hindsight, we understand that $\hat{\kappa}(\boldsymbol{q},\tau)$ is the product between $\hat{K}(\boldsymbol{q},\tau)$ and the optical transfer function (OTF) of the setup $h(\boldsymbol{q})$:

$$\hat{\kappa}(\boldsymbol{q},\tau) = \hat{K}(\boldsymbol{q},\tau)h(\boldsymbol{q}) \tag{3.32}$$

This explains the observed difference evidenced in figure 3.3 between the q-dependence of the integrated SN signal and the q-dependence of the intensity of the interference. A well known result of Fourier optics actually specifies that $h(\boldsymbol{q})$ is different for a coherent or incoherent illumination. This is because, in the case of coherent illumination (blue line figure 3.3), it is the field falling onto the detector which is the convolution of the scattered field and the point spread function (PSF). On the contrary, under incoherent illumination, it is the intensity which is the convolution of the intensity of the scattered field and - this time - of the square modulus of the PSF. In this case, the q-dependence of the integrated SN signal is modulated by this

incoherent OTF (red line in figure 3.3).

Spatio-temporal SN in a nutshell

Let's summarise the main results of this calculation and illustrate the different contributions we identified. Figure 3.5 depicts the evolution of the expected $\boldsymbol{q}$-dependence of the integrated SN signal during our reasoning.

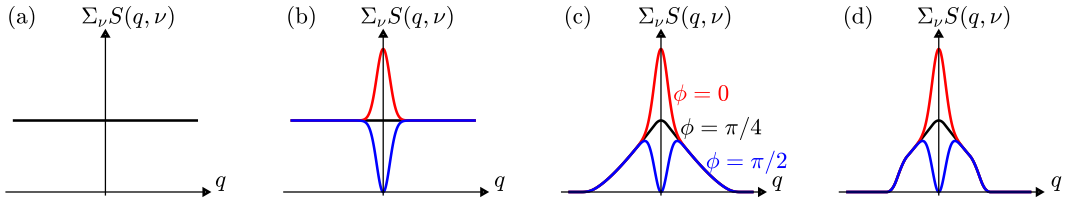

Figure 3.5: Different contributions to the $\boldsymbol{q}$-dependence of the integrated SN signal. (a): A naive forecast. (b): The coherent term adds up to the SN signal. (c): Both the coherent and the incoherent terms are weighted by the OTF. (d) The OTF takes into account the wave vector cut-off (see section 3.2.4). Colors differentiate three relative phase values.

First, equation 3.28 evidenced the presence of two contributions in the detected signal: an incoherent one and a coherent one. The former contains the spin spatial information while the latter could inform about the spatial shape of the beams. This second term is also weighted by a ϕ-dependent modulation (figure 3.5 (b)).
Here, the situation is given by:

$$C_D(\tau) = (\hat{K} \otimes \hat{I}_0^2)(\boldsymbol{q}, \tau) + cos(2\phi)\hat{I}_0^2(\boldsymbol{q})(\hat{K} \otimes \hat{I}_0^2)(\boldsymbol{0}, \tau) \tag{3.33}$$

The optical transfer function $h(\boldsymbol{q})$ is then taken into account, modifying the flat $\boldsymbol{q}$-dependence of both coherent and incoherent terms. The concrete influence of this OTF is highlighted in figure 3.5 (c) and can be described as follows:

$$C_D(\tau) = ((h\hat{K}) \otimes \hat{I}_0^2)(\boldsymbol{q}, \tau) + cos(2\phi)\hat{I}_0^2(\boldsymbol{q})((h\hat{K}) \otimes \hat{I}_0^2)(\boldsymbol{0}, \tau) \tag{3.34}$$

Finally, a more technical issue presented in the next section leads to a modification of the OTF which becomes $h'(q)$(see figure 3.5 (d)). The situation is now described by:

$$C_D(\tau) = ((h'\hat{K}) \otimes \hat{I}_0^2)(\boldsymbol{q}, \tau) + cos(2\phi)\hat{I}_0^2(\boldsymbol{q})((h'\hat{K}) \otimes \hat{I}_0^2)(\boldsymbol{0}, \tau) \tag{3.35}$$

3.2.4 Validation and characterisation of the setup

We now confront our comprehension to the experimental measurement. As we have seen in the last section, probing the spatial spin correlation through the $\boldsymbol{q}$-selectivity does not only affect the width of the SN spectra but it also modifies its intensity. This modulation of the SN signal is due to the optical transfer function of the setup and can include many information. Here we perform different tests in order to validate our comprehension and to characterise our setup. Depending if phase stabilisation is required, we work on two different samples: the M3408 studied in the previous chapter or the M3460. The latter allows for transmission geometry (SN is detected 10 meV below the resonance, see figure 3.6) which is better suited to control the relative phase ϕ.

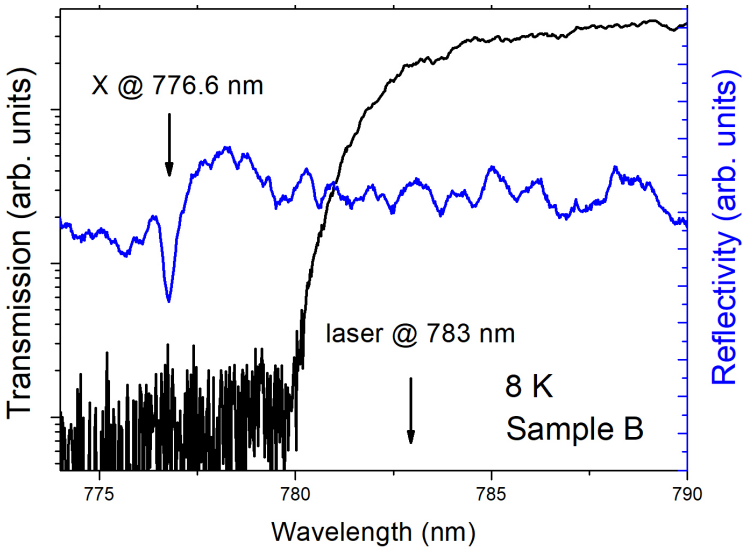

Figure 3.6: Reflectivity and transmission (in semi-logarithmic scale) spectra measured on sample B. The free exciton resonance is marked as X. The laser wavelength which was used for spin noise experiments is also shown.

Evolution of the integrated SN signal

First of all, we test the first term of equation 3.31 comparing the $\boldsymbol{q}$-dependent integrated SN and the estimated optical transfer function convolved with $\hat{I}_0(\boldsymbol{q})$.
SN spectra are measured on sample M3408 under transverse magnetic field and for different $\boldsymbol{q}$. We average to 0 the second term in equation 3.31 by leaving the relative phase free, hence random. We also match the phase of the LO and the scattered light. Figure 3.7 depicts the obtained SN spectra.

Calculation of the optical transfer function is performed under some assumptions.

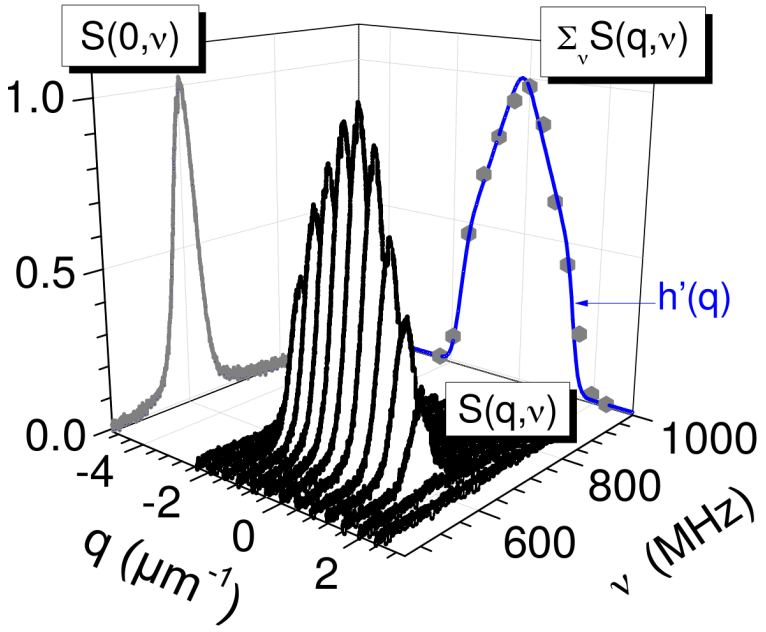

Figure 3.7: Waterfall plot of the SN spectra for different $\boldsymbol{q}$. Both the SN spectrum at $q = 0$ and the $\boldsymbol{q}$-dependence of the integrated signal are also shown. Experimental conditions : $T = 5.2$ K, $P_{laser} = 1$ mW, reflection geometry, sample M3408.

First, we consider there is no spatial correlations. That means $K(\boldsymbol{r}) = \delta(\boldsymbol{r})$ and $\hat{K}(\boldsymbol{q})$ is constant. Hence the first term of equation 3.31 becomes:

$$(\hat{\kappa} \otimes \hat{I}_0^2)(\boldsymbol{q}) = ((\hat{K} \times h) \otimes \hat{I}_0^2)(\boldsymbol{q}) \propto (h \otimes \hat{I}_0^2)(\boldsymbol{q}) \tag{3.36}$$

Then, the spatial distribution of the field is taken as $\hat{I}_0^2(q) = e^{-q^2/Q^2}$ where $Q = 355000$ m^{-1} is determined from the LO spot measured with a CCD and the optical transfer function is taken as:

$$h(\boldsymbol{q}) = \frac{2}{\pi}[\arccos(\frac{\boldsymbol{q}}{q_c}) - |\frac{\boldsymbol{q}}{q_c}|(1 - \frac{\boldsymbol{q}^2}{q_c})^{1/2}] \tag{3.37}$$

which is the convolution of the circular aperture (the pupil function) of the objective with itself. Here, $q_c = \frac{2\pi D}{\lambda f}$ is the cut-off frequency of the pupil, f is the focal length of the objective and D is the diameter of the objective.

Finally we can calculate the $(h \otimes \hat{I}_0^2)(\boldsymbol{q})$ term the integrated signal is expected to follow. Figure 3.8 compares the measured integrated SN signal variation with the calculated one for two different objective apertures. As it stands, our model (dashed lines) describes very well the behaviour at low values of $\boldsymbol{q}$. The observed abrupt decay is due to the maximum ρ_0 allowed by the finite size of the objective. Because the illuminating beam is centred on the objective, the maximum ρ_0 is the diameter

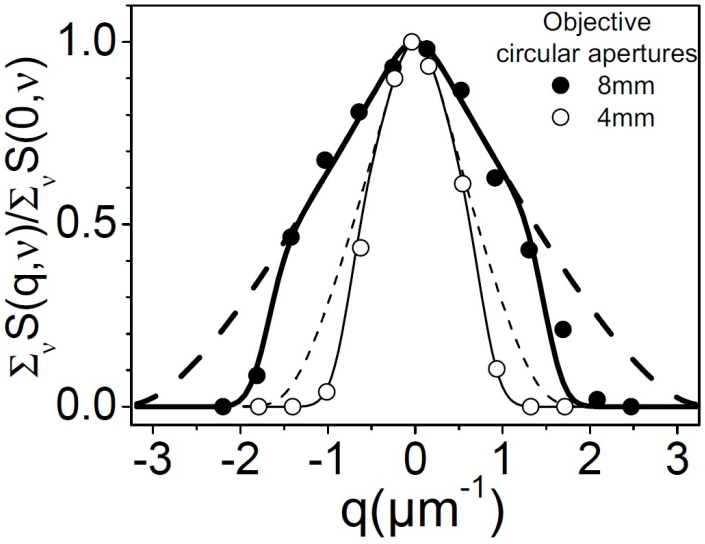

Figure 3.8: Comparison between the integrated SN signal (symbols) and the convolution of the OTF with $\hat{I}_0^2(q)$ (lines). Solid and dashed lines correspond respectively to the model with and without the cut-off due to the maximum allowed ρ_0. Experimental conditions : $T = 5.2$ K, $P_{laser} = 1$ mW, reflection geometry, sample M3408.

aperture divided by 2. This cut-off effect is taken into account by multiplying $h(\boldsymbol{q})$ with the corresponding heavyside function. Corresponding calculated optical transfer functions fit very well all the measured points in the two cases.

Sensitivity to spatial correlations

The calculation presented in the last paragraph has been performed under the assumption that there is no spatial correlation. This assumption is relevant in our system of electron in CdTe layers. However, it is interesting to characterise the sensitivity of our setup to spatial correlations.

Let's consider spatial correlations of the form of $K(\boldsymbol{r}) = e^{-|\boldsymbol{r}|/\xi}$ and calculate the corresponding variation of the integrated signal.

Figure 3.9 allows the comparison of the calculated evolution of the integrated SN signal for different correlation lengths. Spatial correlations exacerbate the decreases of the SN signal with $\boldsymbol{q}$ but smooth the cut-off effect. It enables one to identify their presence. A spatial correlation characterised by a length equals to the inverse of q_c the wave vector cut-off of the objective, $q_c^{-1} = \frac{\lambda f}{2\pi D} = 0.313$ μm can be identified. On the contrary, a spatial correlation characterised by half of this value can not be resolved with this setup.

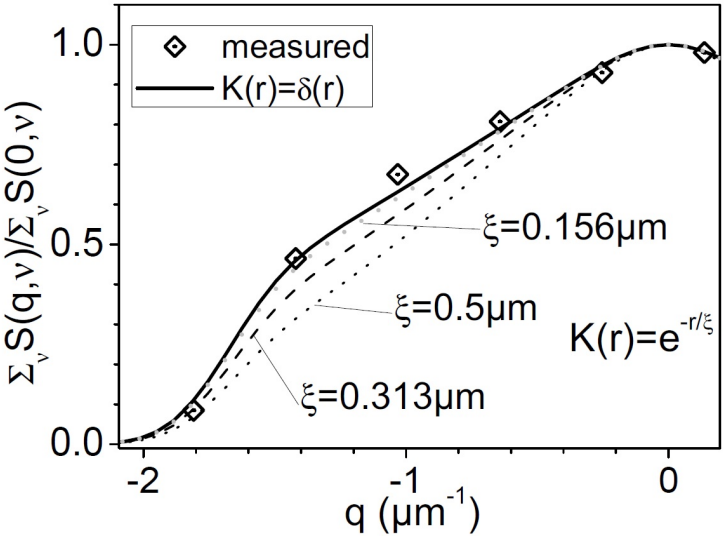

Figure 3.9: Comparison of the calculated $\boldsymbol{q}$-dependance of the integrated spin noise signal in the absence (solid line) of spatial correlations and in the presence of spatial correlations for different correlation lengths (dashed and dotted lines). Symbols are mesured data form figure 3.8.

ϕ-dependence of the $q = 0$ term

Let's come back to equation 3.31. Controlling the relative phase ϕ and monitoring the variation of the integrated SN signal provides a test of its second term. Here, the phase stabilisation is required. We therefore use sample M3460.

At a fixed $\boldsymbol{q}$, varying ϕ leads to oscillations of the integrated SN signal. Such oscillations are shown in figure 3.10. They are characterised by a mean value and an amplitude which are respectively given by the first and the second term of equation 3.31. Both of them are $\boldsymbol{q}$ dependent. Their mean values have already been verified in the last paragraph. Here, we focus on their normalised amplitude $V_\tau(\boldsymbol{q})$ which correspond to their observed amplitudes divided by their mean values (see equation 3.31).

Figure 3.10 shows also the $\boldsymbol{q}$ dependence of the normalised integrated SN signal for particular ϕ. Here, normalised means divided by $(\hat{\kappa} \otimes \hat{I}_0^2)(\boldsymbol{q}, \tau)$, the prefactor of equation 3.31. It therefore represents the measured values of $1 + cos(2\phi)V_\tau(\boldsymbol{q})$ for particular ϕ. Solid lines are calculated from equation 3.31 and show a very satisfying match reflecting our strong comprehension of what happens at non null $\boldsymbol{q}$. It is noteworthy that $V_\tau(\boldsymbol{q})$ inform on the shape of $I_0(\boldsymbol{r})$.

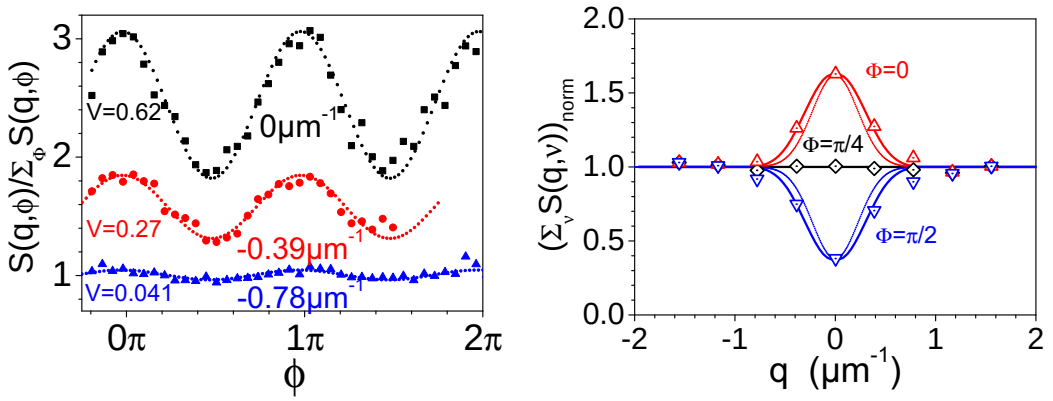

Figure 3.10: Left panel: integrated SN signal versus ϕ for different $\boldsymbol{q}$ (symbols). Data are vertically shifted. Dotted lines represent the corresponding $cos(2\phi)$ fits. Right panel: normalised integrated SN signal versus q for different ϕ (symbols). Wide solid lines are calculated from equation 3.31. Thin dotted lines are calculated under the assumption of large spot. In this case, we can approximate equation 3.31 as $C_D(\tau)/\hat{\kappa}(\boldsymbol{q},\tau) = 1 + cos(2\phi)\hat{I}_0^2(2\boldsymbol{q})/\hat{I}_0^2(\boldsymbol{0})$ Experimental conditions : $T = 4.1$ K, $P_{laser} = 1.1$ mW, transmission geometry, sample M3460.

Broadening of the SN spectra

At this stage, we can consider the issue of the $\boldsymbol{q}$ dependence of the integrated SN signal is a settled matter. Nevertheless, the $\boldsymbol{q}$ dependence of the measured width remains unclear. In what follows we demonstrate how our comprehension of the setup explains the observed variation of the width of the signal.
Figure 3.11 shows SN spectra on sample M3460 under a transverse magnetic field and for different $\boldsymbol{q}$. We observe lorentzian peaks centred on the corresponding Larmor frequency. Here, the coherent term is removed. The inset denotes the measured FWHM as a function of $\boldsymbol{q}$. We notice that the FWHM first increases quadratically and then levels off. Let's try to explain this behaviour.

Here we expect no spatial correlation but only spin diffusion characterised by a diffusion coefficient D_s. In this situation, the spin correlator is given by:

$$\hat{K}(\boldsymbol{q},\tau) = e^{-\boldsymbol{q}^2 D_s \tau} \tag{3.38}$$

We first consider an ideal OTF $h(\boldsymbol{q}) = 1$ and take $I_0^2(\boldsymbol{q}) = e^{-\boldsymbol{q}^2/Q^2}$. It leads to:

$$C_D(\tau) = \frac{2}{2 + Q^2 D_s \tau} e^{-\boldsymbol{q}^2 D_s \tau \left(\frac{2}{2+Q^2 D_s \tau}\right)} \tag{3.39}$$

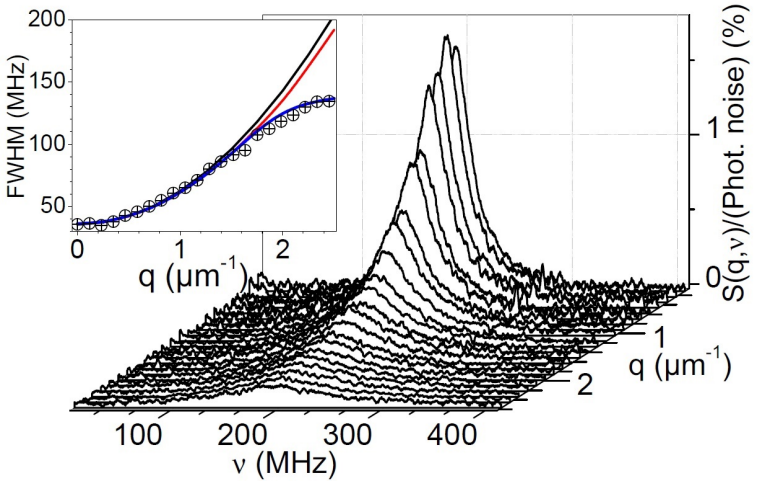

Figure 3.11: Waterfall plot of spin noise spectra measured for a series of $\boldsymbol{q}$ vectors. The inset shows the FWHM (symbols) deduced from Lorentzian fits to the noise spectra. Solid lines shows the calculated FWHM($\boldsymbol{q}$) taking into account the time of flight dynamics (black), the wave vector resolution (red) and the wave vector cutoff (blue). Experimental conditions : $T = 4.1$ K, $P_{laser} = 1.1$ mW, transmission geometry, sample M3460.

Here, we can understand that the measured width undergoes two different effects. Due to the finite size of the spot, spins leaving the probed area do not contribute anymore. This appears as a relaxation and leads to a broadening of the SN spectrum. This is the first effect. It comes from the prefactor of the previous equation and does not depend on $\boldsymbol{q}$. Thus, it adds an offset to the quadratic $\boldsymbol{q}$ dependence of the measured width. From numerical simulations, this offset can be approximated by $\pi Q^2 D_s/9$. If we denote the real spin relaxation rate as γ_s^*, the measured relaxation rate is therefore given by:

$$\gamma(q) = \gamma_s^* + \frac{\pi}{9} Q^2 D_s + D_s q^2 \tag{3.40}$$

which still has a quadratic dependence. The black curve in the inset of figure 3.11 displays such a quadratic fit of the obtained widths for small $\boldsymbol{q}$. In these conditions, the $Q^2 D_s$ offset term remains weak and the determination of γ_s^* is not affected.

The wave vector resolution is the origin of the second effect. It is $\boldsymbol{q}$-dependent and appears in the argument of the exponential in equation 3.39. The measured $D_s q^2$ broadening is actually averaged on the wave vector distribution of the LO and hence, is smoothed. Such an effect has been calculated and is shown by the red solid line (inset of figure 3.11).
A non-ideal OTF could amplify this effect favouring low $\boldsymbol{q}$ contributions over high $\boldsymbol{q}$

contributions. Here, however, the typical width of $h(\boldsymbol{q})$ is about 2.10^6 m^{-1} which is much more than Q. $h(\boldsymbol{q})$ is therefore seen relatively flat by the LO. To be convinced of this, we can roughly model the OTF with a gaussian $h(\boldsymbol{q}) = e^{-q^2/\beta^2}$. It does not correspond to figure 3.8 but it provides an analytical expression for $C_D(\tau)$:

$$C_D(\tau) = \frac{2 + \frac{Q^2}{\beta^2}}{2 + \frac{Q^2}{\beta^2} + Q^2 D_s \tau} e^{-2q^2\left(\frac{D_s\tau + \frac{1}{\beta^2}}{2 + \frac{Q^2}{\beta^2} + Q^2 D_s \tau}\right)} \tag{3.41}$$

Considering $Q^2/\beta^2 \ll 2$, this equation reduces to equation 3.39 and in doing so, persuades us the OTF dynamics is flat enough to have no noticeable effect.

Finally, the stabilisation at high $\boldsymbol{q}$ can be understood considering the wave vector cut-off q_c due to the objective aperture and the wave vector distribution of the LO. Indeed, when the LO beam approaches q_c, the high $\boldsymbol{q}$ components can not interfere with the scattered field anymore because its corresponding high $\boldsymbol{q}$ components have been stopped by the objective. Therefore, the measured width becomes $\boldsymbol{q}$ independent. This behaviour can be reproduced multiplying $C_D(\tau)$ with two appropriate error functions (blue solid line in the inset of figure 3.11).

* *
*

We finally can rely on a robust implementation of a $\boldsymbol{q}$-sensitive SNS setup. In addition to spin relaxation rate, we are also able to optically study spin diffusion as in the transient spin grating technique [16, 17], without necessarily perturb the spin system. It is important to note that using a LO enables to maintain constant the illumination conditions of the sample. In the next section, we come back to electrons gas in CdTe whose spatio-temporal dynamics is now addressed.

3.3 Spatio-temporal spin dynamics in CdTe

Let's first establish an overall picture of the situation. We have studied electron spin dynamics via SNS in n-CdTe thin layers in backscattering configuration and have observed a two-peak structure due to the precession of electrons in the randomly fluctuating nuclear magnetic field. This structure appears in old samples but also in some recent ones and for different doping levels. In addition, we have implemented a q-sensitive SNS which gives access to spin diffusion coefficient. On this occasion, we have received newer samples with transparent substrate allowing for transmission configuration measurements. Satellite line have also been observed in one of this new

sample. Table 3.1 summarises this situation and gives the main characteristics of the samples.

sample	n_D (cm^{-3})	thickness (μm)	substrate	satellite
M1409	6×10^{18}	0.58	$Cd_{0.96}Zn_{0.04}Te$	yes (B)
M896	6×10^{16}	0.6	$Cd_{0.96}Zn_{0.04}Te$	yes (B)
M1371	6×10^{15}	0.52	$Cd_{0.96}Zn_{0.04}Te$	yes (B)
M1559	3×10^{16}	2.5	$Cd_{0.96}Zn_{0.04}Te$	yes (B+F)
M3405	3×10^{17}	13.3	CdTe	yes (B)
M3406	$\sim 10^{16}$	13.3	CdTe	no (2.6 mW)
M3407	$\sim 10^{15}$	13.3	CdTe	yes (B)
M3408	2×10^{17}	0.5	CdTe	yes (B)
M3416	$\sim 10^{17}$	13.5	$Cd_{0.96}Zn_{0.04}Te$	no (B+F)
M3459	10^{17}	10	$Cd_{0.96}Zn_{0.04}Te$	no (F)
M3460	2×10^{16}	10	$Cd_{0.96}Zn_{0.04}Te$	yes (F)

Table 3.1: Main characteristics of the studied samples. The last column indicates if the satellite has been detected, and for which configuration (B for backscattering, F for forward scattering).

All samples are Al-doped CdTe layers grown on top of a CdTe buffer layer, and a (100) CdTe or $Cd_{0.96}Zn_{0.04}Te$ substrate.
The four first samples are old samples in which the satellite line has been first observed. The substrate of sample M1559 has been mechanically polished to allow for measurements in forward scattering configuration. Note that in these samples, SIMS measurements revealed the presence of Zn in the doped CdTe layers (probably up to 2% in sample M1371 revealed by a shift of the excitonic resonance of about 20 meV). In the case of sample M1559 clusters of Al were also detected.
The other samples are new samples grown specifically for the study of the two-peak structure. The donor density has been estimated from Hall measurements on the metallic sample M1409, which served as a reference for the determination of the concentration of the other samples by SIMS. The three last samples have been grown on mechanically polished $Cd_{0.96}Zn_{0.04}Te$ substrates for measurements of spin noise in forward scattering. The last column of the Table indicates whether the satellite line has been detected or not.

The satellite line has been observed in most of the studied samples, including insulating samples with density below the Mott transition (about 1.2×10^{17} cm^{-3} in CdTe), samples close to the Mott transition, and even one metallic sample.
The satellite could be observed both in reflection and transmission geometry (samples

M1559 and M3460). In sample M3406 the satellite could not be observed, but a relatively high probe power (2.6 mW) was required to detect the spin noise in this sample. At this high excitation power, we did not observe the satellite in any sample.

3.3.1 Temperature and power dependence

Influence on the SN shape

Increasing the temperature and/or the probe power modifies the spin noise spectrum. At $B = 0$ T, the satellite peak disappears progressively and merges with the central peak whose width increases. Such a temperature dependence is shown in figure 3.12 for two different excitation powers. We can see that increasing the power acts as increasing the temperature. It should indicate a laser heating.

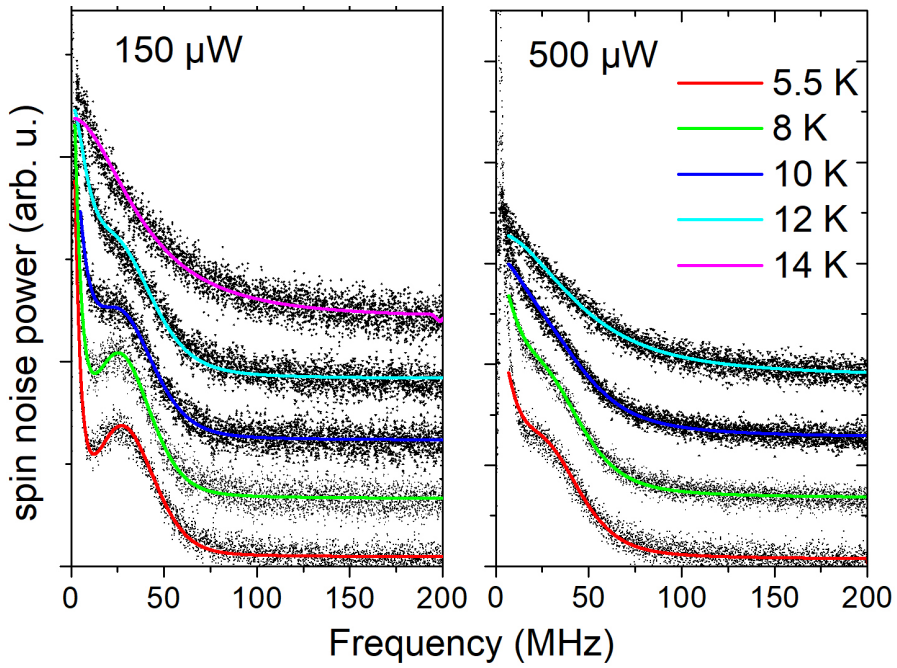

Figure 3.12: Influence of temperature and power on the two peaks structure of spin noise spectra at $B = 0$ T. Experimental conditions: sample M3408, homodyne configuration, $q = 0$. Colored solid lines correspond to fit with the Glazov's model (see chapter 2)

Under transverse magnetic field, increasing the temperature or the probe power changes the lineshape of the SN spectra. At low temperature and for a low excitation power, the SN spectrum is gaussian. At higher temperature or higher probe power, SN spectra become lorentzian. They are also broader.
Such a transition is illustrated in figure 3.13 which depicts one SN spectrum of each

shape and evidences the broadening. It will be discussed below, in the light of the knowledge of the spin diffusion coefficient.

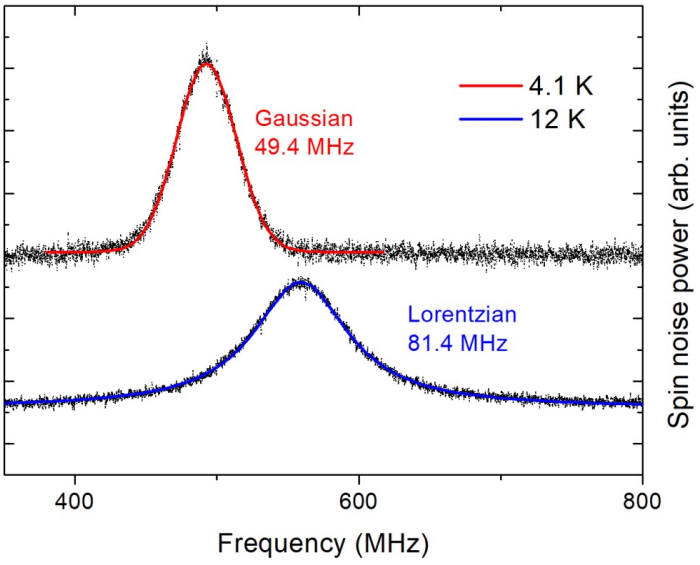

Figure 3.13: Examples of spin noise spectra measured in the regime of long and short correlation time on sample M3408.

Influence on the spin dynamics

Spin diffusion can be extracted from the SNS width dependence on q. We now focus on spin noise spectra detected on sample M3408 in backward, homodyne and q-sensitive configuration under a transverse magnetic field. Other noise sources are removed modulating the magnetic field between 0 and either 22 or 24.4 mT. Spectra are therefore flat and contain two peaks of opposite signs and centered on corresponding Larmor frequencies. These peaks are fit with a gaussian or a lorentzian distribution depending on the experimental conditions.

Figure 3.14 displays the measured transverse spin relaxation rate γ_2 dependence on q at different temperatures. As expected, γ_2 varies quadratically with q at high enough temperatures:

$$\gamma_2(q) = \gamma_s + D_s q^2 \tag{3.42}$$

At low temperatures, the dependence is flat on the whole accessible range of wave vectors and the spin diffusion coefficient can not be extracted. Fitting these measurements provides both the spin diffusion coefficient and the spin relaxation time. From extracted values of D_s and γ_s, we have checked that the $\pi Q^2 D_s/9$ term never exceed 5% of the measured γ_s (here $Q \approx 425000\text{m}^{-1}$).

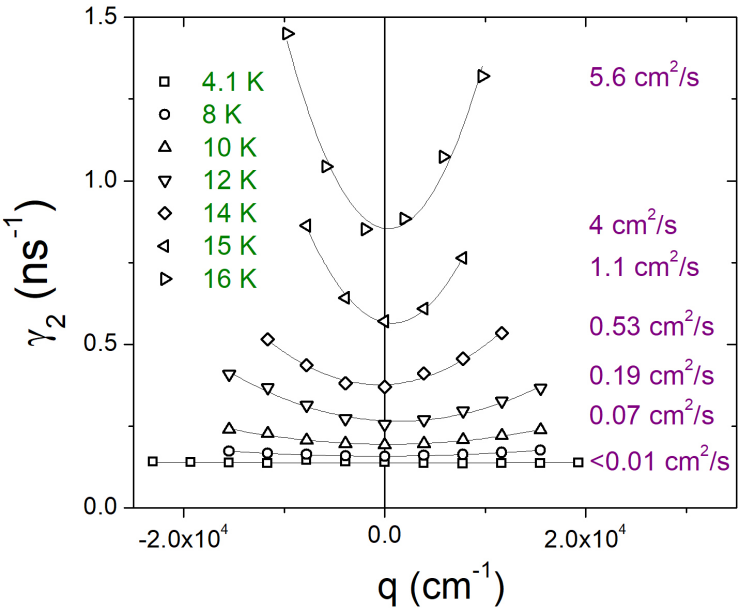

Figure 3.14: Measured spin relaxation rate versus q for a series of temperature (open symbols), and quadratic fits (continuous lines) from which the spin relaxation rates and spin diffusion coefficients are deduced. Experimental conditions: $P_{laser} = 500\ \mu$W, sample M3408

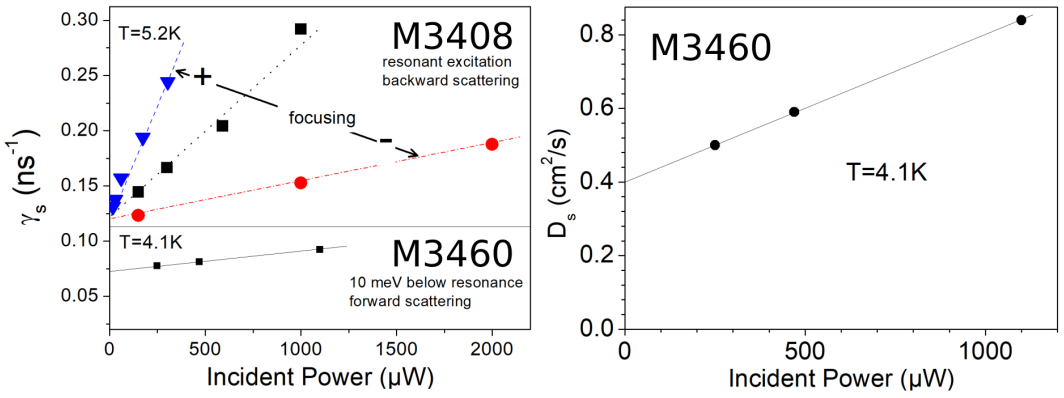

Figure 3.15: Linear power dependence of γ_s and D_s for sample M3408 and M3460.

We have also checked the power dependence of the spin dynamics characteristic parameters. Both γ_s and D_s increase linearly with the probe power. The slope changes for different focusing but the y-intersect is the same, confirming the possibility to determine the unperturbed values by extrapolation to zero incident power. The previously presented extracted parameters have not been obtained with this extrapolation procedure. However, they may be close to the unperturbed values because the probe was not extremely focused.

Identification of two different regimes

The observation of both the two-peak structure and the broadening due to spin diffusion coefficient are not possible simultaneously in all conditions. At low temperatures -and not too high power - the satellite line is clearly visible while the quadratic broadening due to spin diffusion is negligible. At high temperature, the spin diffusion coefficient can be easily extracted but the two-peak structure vanishes. The transition corresponds more or less to the previously identified transition from an inhomogeneous to an homogeneous broadening. It leads us to interpret this transition as the evidence of two different regimes characterised by the product of the correlation time of the effective random fields acting on the electrons and the precession frequency. Here, the correlation time corresponds to the electron spin correlation time on a given donor site τ_c.
In the long correlation time regime, that means when $W_0 \ll \delta_e$ or in equivalent term $\tau_c \gg 1/\delta_e \approx 5.5$ ns, we can observe the two-peak structure in zero-field. The spin diffusion constant is smaller than 0.5 cm^2/s. In a transverse magnetic fields larger than the local nuclear field, the SN spectrum is gaussian and its FWHM tends to about 40 MHz for long τ_c.
On the contrary in the short correlation time regime, when $W_0 \gg \delta_e$, the two-peak structure disappears, the line becomes lorentzian, and the spin diffusion coefficient is higher.

3.3.2 Spatio-temporal spin dynamics in CdTe

Overview

Let's try to synthesise all our measurements in such a way they are comparable. For this purpose we suggest to study the spin dynamics as a function of the correlation time which governs the transition between the two identified regimes.

We focus on samples for which the two-peak structure has been detected. For these samples, $\tau_c = W_0^{-1}$ is extracted from the fit of the SN spectra at $B = 0$ with the Glazov's model (see section 2.2.2). Corresponding γ_s are obtained under a transverse magnetic field in identical experimental conditions. The experimental points which correspond to the long correlation time regime can therefore be placed on figure 3.16 (open symbols).
For sample M3408 we have also measured the spin diffusion coefficient and reported the corresponding values on figure 3.16 (closed triangles). We can see that D_s is inversely proportional to τ_c. This behaviour is expected if the diffusion is due to spin

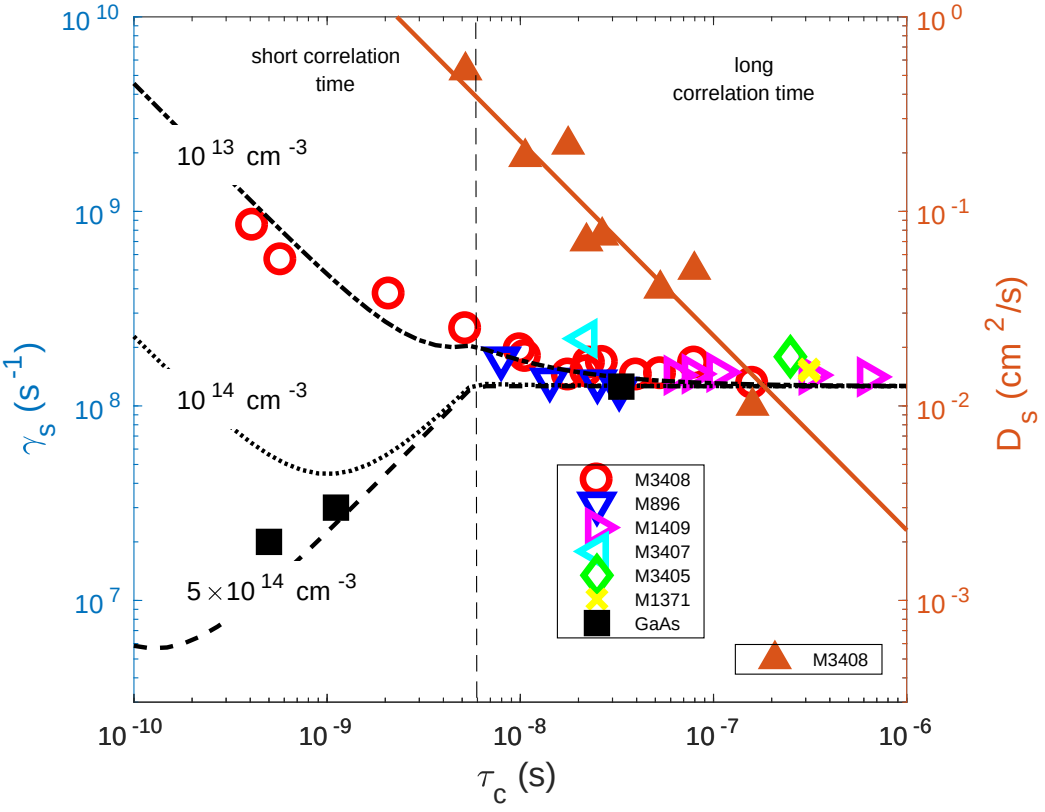

Figure 3.16: Comparison between measured (symbols) and calculated (lines) γ_s and D_s versus τ_c. The black lines are the calculated spin relaxation rates for different donor concentrations for CdTe (dotted, dashed-dotted), and for GaAs (dashed). The solid brown line is the calculated spin diffusion constant D_s. The open, colored symbols are the measured spin relaxation rates for different samples, and the closed triangles are the measured spin diffusion coefficients for sample M3408. The black filled squares are taken from literature [18, 19] and correspond to GaAs.

exchange between donors and if the correlation time is limited by this mechanisms ($\tau_c = \tau_{\text{hop}}$). In this case, in the model of diffusion due to hopping the diffusion constant is actually given by:

$$D_s = \frac{r_c^2}{6\tau_c} \tag{3.43}$$

where r_c is the characteristic distance between interacting donors.
In the short correlation time regime, the satellite line is no longer visible and the extraction of τ_c is not possible. Assuming the τ_c^{-1} dependence of D_s remains valid in this regime, we are able to place the three last experimental points (the three leftmost red circles).

Results on GaAs from the literature [18, 19] are shown in closed black squares. In these works, τ_c is extracted from either the longitudinal field dependence of the

polarisation of the PL [19] or from transport measurement [18].
All these experimental points are compared to theoretical calculations presented in the next paragraph.

Calculation of γ_s as a function of τ_c

In what follows, we model the evolution of the spin relaxation time with the spin correlation time taking into account the two mechanisms which govern the spin relaxation of localised electrons. They are respectively due to the hyperfine interaction [19] and to the anisotropic exchange interaction between donors [20]. In this context the spin relaxation is driven by hopping of the localized electron from an occupied to an unoccupied donor, or by hopping of the spin alone by exchange between two occupied donors. We ignore the Dyakonov-Perel relaxation mechanism for delocalised electrons, because it is hardly compatible with the long spin correlation times we are dealing with.

The spin relaxation rate for the AEI is given by

$$\gamma_{\mathrm{AEI}} = \frac{2}{3}\frac{\theta^2}{\tau_{\mathrm{hop}}}, \tag{3.44}$$

where τ_{hop} is the hopping time, and

$$\theta = \frac{\gamma_D}{E_b a_B^3}\left(0.323 + 0.436r + 0.014r^2\right) \tag{3.45}$$

is the rotation angle of the spin due to hopping between donors [19, 20]. Here γ_D is the Dresselhaus coefficient, E_b the donor binding energy, a_B is the Bohr radius, and $r = r_c/a_B$. r_c is the characteristic distance between interacting donors and is given by $r_c = \beta n_d^{-1/3}$, with $0.54 \leq \beta \leq 0.8$.

The spin relaxation rate due to hyperfine interaction is given by

$$\gamma_{\mathrm{HI}} = \frac{2}{3}\langle\omega_N^2\rangle\tau_c = \frac{2}{3}\delta_e^2\tau_c \tag{3.46}$$

in the motional narrowing regime where the spin correlation time $\tau_c \ll \delta_e^{-1}$. In the opposite case the line is inhomogeneously broadened by the distribution of nuclear fields and the spin relaxation rate, defined as the FWHM divided by π, is given by:

$$\gamma_s = \sqrt{\log(2)}\delta_e \tag{3.47}$$

We are therefore able to calculate the resulting spin relaxation time as a function of τ_c. The needed parameters are E_b, a_B, γ_D and δ_e. Their respective values for CdTe and GaAs are listed on table 3.2. We also need r_c which depends on the doping level. We will vary this parameters in order to exhibit the influence of the doping level on the spin relaxation evolution.

	GaAs	CdTe
E_b (meV)	5	10
a_B (nm)	10	5.2
γ_D (μeVÅ^3)	19	12*
δ_e (MHz)	$2\pi \times 29$	$2\pi \times 29$

Table 3.2: GaAs and CdTe parameters used in the calculation of γ_s as a function of τ_c. The star indicates this value comes from our fit.

Here, γ_D in CdTe is determined from our experimental measurements. Equations 3.44 and 3.43 actually link the Dresselhaus coefficient to D_s and γ_s as follows:

$$\gamma_D^2 \propto \frac{\gamma_s}{D_s} \tag{3.48}$$

We can therefore exctract γ_D from the experimental points where the AEI predomines. The obtained value $\gamma_D = 12$ μeVÅ^3 falls in the range of published values for CdTe [21–23].

Calculations of the spin relaxation time in CdTe for two doping levels $n_d = 10^{14}$ cm^{-3} (dotted curve) and $n_d = 10^{13}$ cm^{-3} (dashed-dotted curve) are shown in figure 3.16. The last curve - the dashed one - corresponds to calculations for GaAs at $n_d = 5 \times 10^{14}$ cm^{-3}. In the long correlation regime, this line merges with those calculated for CdTe because the same δ_e has been observed in GaAs and in CdTe.

Discussion

From these calculations, we can distinguish three different spin relaxation regimes. For $\tau_c < 10^{-9}$ s^{-1} the relaxation is dominated by the AEI, thus γ_s and τ_c are inversely proportional. For $\tau_c > 10^{-9}$ s^{-1} the relaxation is dominated by the HI, in the motional narrowing regime up to 5×10^{-9} s^{-1}. For $\tau_c > 5 \times 10^{-9}$ s^{-1} one enters in the regime of pure spin dephasing where the broadening is constant.
Increasing the doping level shifts the transition between the AEI and the HI relaxation regimes to smaller τ_c.

In the long correlation time regime, the calculated value $\gamma_s = \sqrt{\log(2)}\delta_e$ is about 40 MHz and fits very well with the experimental points. The similarity between GaAs and CdTe is striking.
In the short correlation time regime however, spin relaxation in CdTe and in GaAs behave differently. In GaAs the regime of dynamic averaging of the random nuclear fields is evidenced by the decrease of γ_s with τ_c. This is not the case in CdTe where γ_s increases as τ_c decreases. But here shorter τ_c are reached on the same sample by increasing the temperature, while in GaAs the measurements were all performed at low temperatures and τ_c is mainly correlated to the doping level. It is plausible that in this case some other spin relaxation mechanism comes into play.
It is also remarkable that for $n_d = 10^{13}$ cm^{-3} one obtains a good agreement between theory and experiment, simultaneously for γ_s and D_s without additional fitting parameters.

Finally, we compare our results with the literature. To date the most systematic study of electron spin relaxation in n-doped CdTe has been performed by time-resolved Kerr rotation experiments [24]. In this work, the longest spin relaxation time was found to be $\simeq 2.5$ ns for $n_d \simeq 5 \times 10^{16}$ cm^{-3}. This relaxation time sharply decreases at lower concentrations to reach about 40 ps for $n_d < 10^{16}$ cm^{-3}. This behaviour seems hardly compatible with the well understood spin relaxation mechanisms established for GaAs.
Our results differ considerably from those obtained in [24], since we measured longer spin relaxation times $\sim 6 - 7$ ns for a broad range of doping level and that this relaxation seems to be due to HI only.

3.4 Conclusion

In conclusion we demonstrated a spin noise setup providing direct access to both spatial and temporal spin correlations. This promising setup allowed us to measure spin noise spectra for many different n-doped CdTe samples and to detect rather systematically a satellite line in the zero-field spectra due to the local nuclear fields. The existence of this satellites implies long spin correlation times $\tau_c > 6$ ns, even for large doping levels, which is quite surprising and not understood. Simultaneous determination of γ_s and D_s has allowed us to compare spin relaxation in CdTe and GaAs and to point out their unexpected difference. Probably a complete understanding of electron spin relaxation mechanisms in CdTe will require a joint

study of spin relaxation and transport properties similar to what has been done for GaAs [25].

Bibliography

[1] PS Pershan, JP Van der Ziel, and LD Malmstrom. Theoretical discussion of the inverse faraday effect, raman scattering, and related phenomena. *Physical Review*, 143(2):574, 1966. [3.1]

[2] R Romestain, S Geschwind, and GE Devlin. Measurement of spin-flip-raman-scattering cross section and exchange effects for donors in cds by faraday rotation. *Physical Review Letters*, 35(12):803, 1975. []

[3] BM Gorbovitsky and VI Perel. Aleksandrov and zapassky experiment and raman effect. *OPTIKA I SPEKTROSKOPIYA*, 54(3):388–390, 1983. [3.1]

[4] Georg M Müller, Michael Römer, Dieter Schuh, Werner Wegscheider, Jens Hübner, and Michael Oestreich. Spin noise spectroscopy in gaas (110) quantum wells: Access to intrinsic spin lifetimes and equilibrium electron dynamics. *Physical review letters*, 101(20):206601, 2008. [3.1]

[5] VG Lucivero, ND McDonough, N Dural, and Michael V Romalis. Correlation function of spin noise due to atomic diffusion. *Physical Review A*, 96(6):062702, 2017. [3.1]

[6] Yuriy V Pershin, Valeriy A Slipko, Dibyendu Roy, and Nikolai A Sinitsyn. Two-beam spin noise spectroscopy. *Applied Physics Letters*, 102(20):202405, 2013. [3.1]

[7] GG Kozlov, II Ryzhov, and VS Zapasskii. Light scattering in a medium with fluctuating gyrotropy: Application to spin-noise spectroscopy. *Physical Review A*, 95(4):043810, 2017. [3.1]

[8] GG Kozlov, II Ryzhov, and VS Zapasskii. Spin-noise spectroscopy of randomly moving spins in the model of light scattering: Two-beam arrangement. *Physical Review A*, 97(1):013848, 2018. [3.1]

[9] Felix Bloch. Nuclear induction. *Physical review*, 70(7-8):460, 1946. [3.1]

[10] Henry C Torrey. Bloch equations with diffusion terms. *Physical review*, 104(3):563, 1956. [3.1]

[11] BM Gorbovitskii and VI Perel. Aleksandrov and zapasskii experiment and the raman effect. *Optics and Spectroscopy*, 54:229–230, 1983. [3.1]

[12] Steeve Cronenberger and Denis Scalbert. Quantum limited heterodyne detection of spin noise. *Review of Scientific Instruments*, 87(9):093111, 2016. [3.1]

[13] Pavel Sterin, Julia Wiegand, Jens Hübner, and Michael Oestreich. Optical amplification of spin noise spectroscopy via homodyne detection. *Physical Review Applied*, 9(3):034003, 2018. []

[14] M Yu Petrov, AN Kamenskii, VS Zapasskii, M Bayer, and A Greilich. Increased sensitivity of spin noise spectroscopy using homodyne detection in n-doped gaas. *Physical Review B*, 97(12):125202, 2018. [3.1]

[15] AV Poshakinskiy and SA Tarasenko. Spatiotemporal spin fluctuations caused by spin-orbit-coupled brownian motion. *Physical Review B*, 92(4):045308, 2015. [3.1]

[16] AR Cameron, P Riblet, and A Miller. Spin gratings and the measurement of electron drift mobility in multiple quantum well semiconductors. *Physical review letters*, 76(25):4793, 1996. [3.2.4]

[17] SG Carter, Z Chen, and Steven T Cundiff. Optical measurement and control of spin diffusion in n-doped gaas quantum wells. *Physical review letters*, 97(13):136602, 2006. [3.2.4]

[18] Fabian Berski, Jens Hübner, Michael Oestreich, Arne Ludwig, AD Wieck, and Mikhail Glazov. Interplay of electron and nuclear spin noise in n-type gaas. *Physical review letters*, 115(17):176601, 2015. [3.16, 3.3.2]

[19] RI Dzhioev, KV Kavokin, VL Korenev, MV Lazarev, B Ya Meltser, MN Stepanova, BP Zakharchenya, D Gammon, and DS Katzer. Low-temperature spin relaxation in n-type gaas. *Physical Review B*, 66(24):245204, 2002. [3.16, 3.3.2, 3.3.2, 3.3.2]

[20] K_V Kavokin. Anisotropic exchange interaction of localized conduction-band electrons in semiconductors. *Physical Review B*, 64(7):075305, 2001. [3.3.2, 3.3.2]

[21] M Cardona, NE Christensen, and G Fasol. Relativistic band structure and spin-orbit splitting of zinc-blende-type semiconductors. *Physical Review B*, 38(3):1806, 1988. [3.3.2]

[22] Marko D Petrović and Nenad Vukmirović. Spin relaxation in cdte quantum dots with a single mn atom. *Physical Review B*, 85(19):195311, 2012. []

[23] F Passmann, S Anghel, T Tischler, AV Poshakinskiy, SA Tarasenko, G Karczewski, T Wojtowicz, AD Bristow, and M Betz. Persistent spin helix manipulation by optical doping of a cdte quantum well. *Physical Review B*, 97(20):201413, 2018. [3.3.2]

[24] D. Sprinzl, P. Horodyská, N. Tesařová, E. Rozkotová, E. Belas, R. Grill, P. Malý, and P. Němec. Influence of n-type doping on electron spin dephasing in cdte. *Phys. Rev. B*, 82:153201, Oct 2010. [3.3.2]

[25] Jan G Lonnemann, Eddy P Rugeramigabo, Michael Oestreich, and Jens Hübner. Closing the gap between spatial and spin dynamics of electrons at the metal-to-insulator transition. *Physical Review B*, 96(4):045201, 2017. [3.4]

Chapter 4

Indirect excitons in asymmetric coupled quantum wells

Contents

This chapter is dedicated to the study of the spin and population dynamics of indirect excitons (IX). In the first section, the motivations and the objectives of this work are presented. Section 4.2 introduces the sample and section 4.3 is a description of the setup used for PL. Sections 4.4 and 4.5 present photoluminescence measurements which offer a good understanding of the dynamics of the system. The main results of these two sections were published in [1]. Finally, section 4.6 is dedicated to pump-probe spectroscopy of IX in coupled asymmetric GaAs/AlGaAs QW. Summary and perspectives of this work are presented in section 4.7.

4.1 Context and objectives

We have discussed in section 1.3 the potential of IX for studies of collective quantum states (BEC) in semiconductors. Among various solutions to create high-density excitonic fluids (we should speak about fluids because excitons are interacting particles), we have chosen IX or dipolar excitons in CQW. Such excitons have been addressed since 1978 mainly in GaAs/AlGaAs structures with typically characterised by well width between 8 and 16 nm, a thin barrier of 4 nm and a Al concentration around 30% [2–7].

Cold and dense IX gases - that means under 1 K for $n \approx 10^{10}$ cm^{-2} that is below $T_c \approx 3$ K - have been realised in such structures. The reported experimental findings include spontaneous transport into spatially modulated state [8, 9], spontaneous coherence and condensation [10–12], long-range spin currents and textures [13–15], formation of dark [16] and bright [17] excionic liquids, as well as superfluidity [18, 19]. The majority of these experiments relies on in plane-confinement of IX to create high IX densities. The most promising solution is that of electrostatic traps [20]. However, the important issue related to the studies of IX condensation is due to the darkening of its emission.

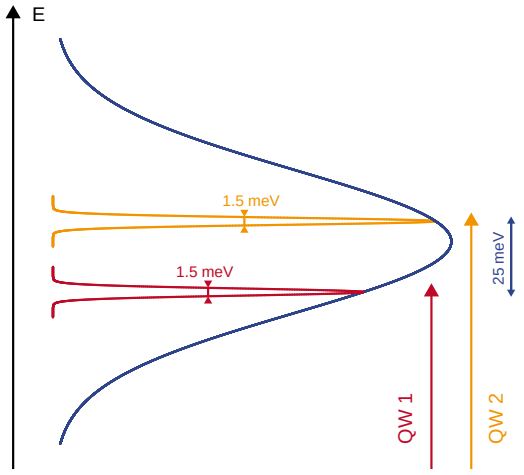

Figure 4.1: Basic idea of the spectroscopy of dark IX. Selective excitation on two different QW leads to two different signals, allowing discrimination between exciton subsystems (energy split ≈ 25 meV). Spectral filtering of the wide in energy femtosecond laser pulses (blue line) provides two laser pulses selectively resonant (≈ 1.5 meV width) with each QW (red and yellow lines).

The dark nature of the lowest in energy IX states was pointed out by Combescot *et al.* in [21] and confirmed experimentally [9, 18, 22]. It was shown that the photolu-

minescence is not a suitable method to look for exciton BEC, at least in the regime where dark states are not mixed with the bright ones [12, 23].

The objective of this work is to explore the non linear technics proposed in [24] to study IX in CQWs. Proof-of-concept of this method has been provided in [6] in a symmetric CQW structure. It was therefore impossible to address dark states independently from bright states (see section 1.3.2). Thus, an asymmetric CQW structure has been designed by François Dubin in INSP and by Aristide Lemaître in C2N. Such a structure enables to address selectively the two different direct transitions (see figure 4.1) and therefore to reach spin polarisation and density of bright and dark IXs.

* *
*

The main motivation of this work on IX was to study asymmetric CQW structures specially designed in order to enable selective resonant excitation on the two different wells. Unfortunately, the objective of studying dark IX has not been achieved, pump probe signal having been obtained in only one resonance. Nevertheless, we were able to characterise the structure, to demonstrate the presence of IX and to measure their lifetime and spin relaxation time both by photoluminescence and pump-probe spectroscopy. The following sections present our work, starting by a description of our sample in the next section.

4.2 Sample

Structure

The structure of the studied sample is shown in figure 4.2. The active region consists in a pair of GaAs quantum wells. The well where electron is confined under electrical field is 8 nm wide as in previously studied samples [2, 6, 25, 26]. The other well is larger (12 nm) in order to lift the degeneracy of the two direct transitions. They are separated by a 4 nm $Al_{0.33}Ga_{0.67}As$ barrier just like typically studied samples [2–7, 25, 26] in order to allows for the electron spin tunnelling [27]. This active region is placed 150 nm above an n-doped GaAs layer serving as ground electrode.
The relative position of the CQW with respect to the electrodes is chosen to obtain a homogeneous field [20]. The electrical insulation of CQWs with respect to the sample holder is provided by a super-lattice grown between n-GaAs and undoped 800 nm-thick GaAs layer which acts as a barrier for leakage currents.
The bottom electrode is realised etching the structure at the edge down to the 200 nm

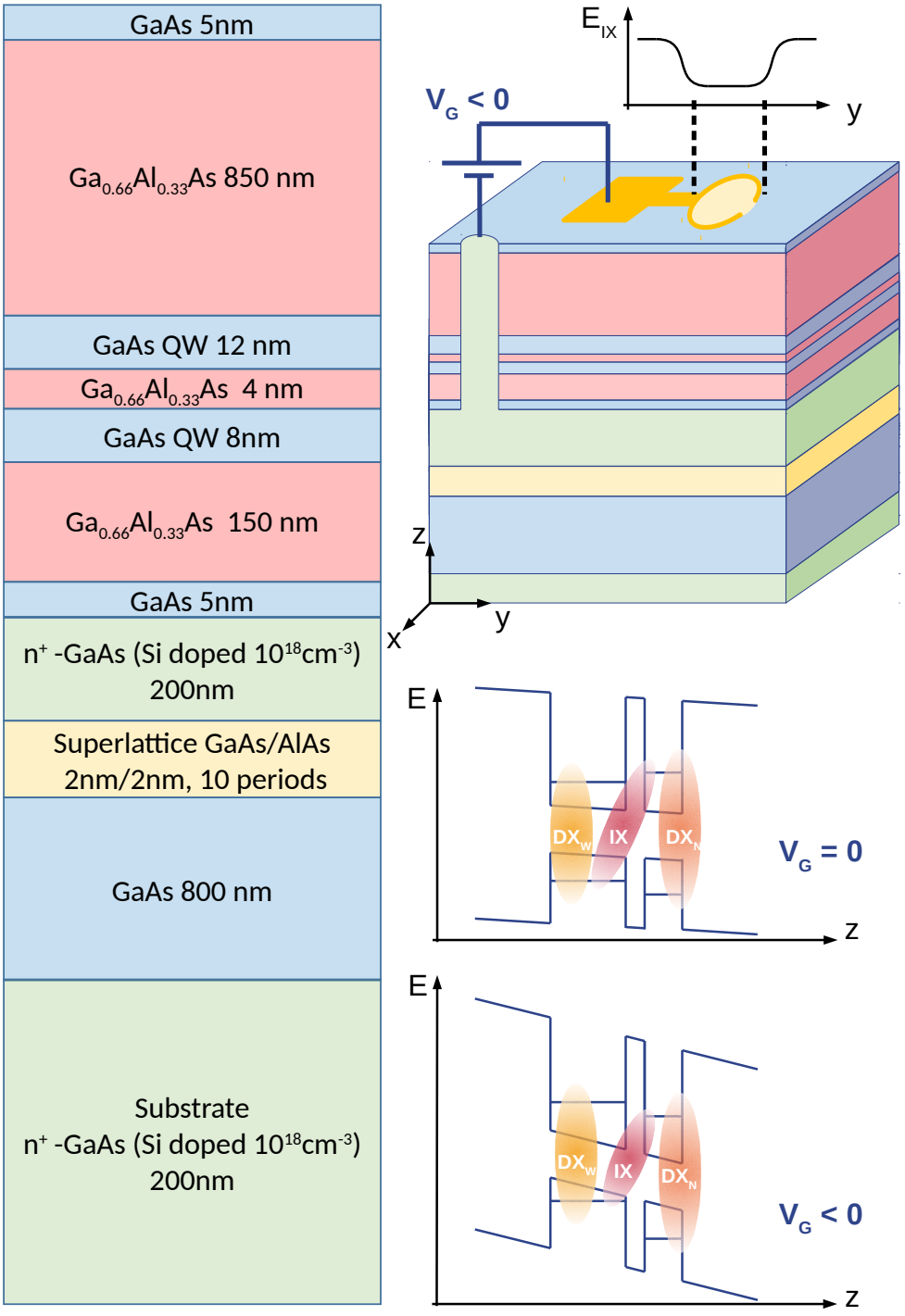

Figure 4.2: Left panel: schematic description of the heterostructure. Right top panel: schematic 3D view of the sample and its electrode which provide both the electrostatic trap and electrical connections (top). On top of the structure are the top electrode and the electrostatic trap. A simplistic spatial evolution of the corresponding in plane potential seen by IX is shown in black. The green column shows the electrical contact with the bottom electrode. Right middle and bottom panels: evolution of the band diagram of the structure with the applied voltage.

doped GaAs layer and depositing Ge/In contacts. Disc-shaped semi-transparent electrodes have been deposited by optical lithography on the surface of the heterostructure. 200 nm-thick gold electrodes deposited on top ensure reliable electrical contact and the possibility to solder Al wire bond. Many identical sets of patterns have been realised. Each set of pattern consists in five discs of different diameters from 5 to 100 μm (see figure 4.3). In this work, we focus only on two of these traps denoted 1 and 2 of 100 μm. Note that symmetric CQW identical in terms of structure and fabrication have been addressed in [2].

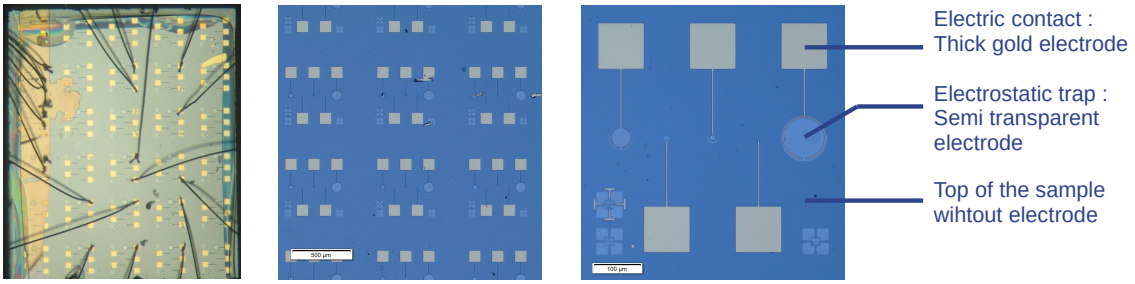

Figure 4.3: Left panel: picture of the sample after bonding. The yellow thin area on the left is the contact to the bottom electrode. Yellow squares are the top electrodes. Al bonding wire are soldered on different traps and also on the bottom electrode. Middle and right panels: Top view of the sample before bonding (microscopy) showing few designed patterns (middle panel) and one pattern with traps (right panel). Grey areas correspond to thick electrode and light blue areas correspond to semi transparent electrode (light blue disks are electrostatic traps)

Electrical characterisation

At the interface between semi-transparent electrodes and GaAs top layer, a Schottky junction forms. As a result, even in the absence of external bias, the built-in electric field is present (see figure 4.2). Application of a positive bias results in a strong leakage current - that can even damage the device - and it is probably impossible to redress the built-in field.

Figure 4.4 shows the electrical characteristics of the studied trap (trap 1, see below) under resonant excitation for different laser powers. The right panel displays the photocurrent, defined as the difference of current with laser ON and OFF. It appears an important contribution due to light excitation even at low excitation power ($P_{laser} = 120$ μW).

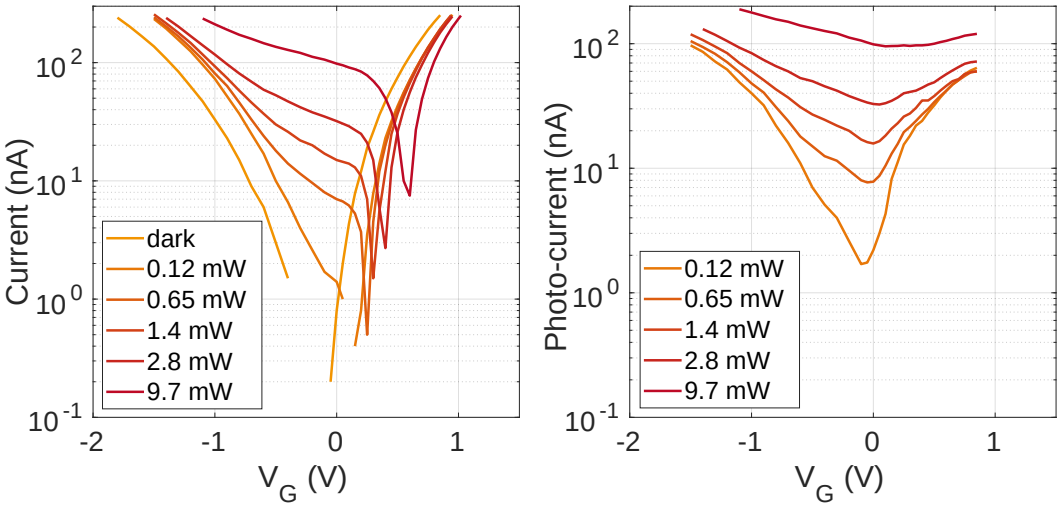

Figure 4.4: Left panel: Electrical characteristic of the studied trap (trap 1, see below) for different light power (laser resonant with the narrow well). Right panel: Corresponding photo-current calculated as the difference with the dark electrical characteristic. Experimental conditions: $T = 3$ K.

Interband transitions in asymmetric CQW

Since the photoluminescence energies depend on the applied gate voltage and the resulting total electric field, we estimate the built-in electric field by comparing the experimentally measured transition energies with the simple numerical calculations described below.

Applying an electric field across the sample tilts the energy bands of the structure by introducing a z-dependent term in the electron and hole Hamiltonians: $H_V = \pm eFz$. Electrons and holes tunnel in opposite directions. Quantum confined Stark effect modifies their energy levels. Increasing the electric field, the excitonic ground state changes from direct to indirect exciton (see figure 4.2). If we neglect interaction between electrons and holes, both their discrete energy levels and their envelope wave function can be obtained resolving the following Schrödinger equation:

$$-\frac{\hbar^2}{z}\frac{\partial}{\partial z}\frac{1}{m_{e,h}}\frac{\partial}{\partial z}\Psi_{e,h}(z) + V_{e,h}(z)\Psi_{e,h}(z) = E_{e,h}\Psi_{e,h}(z) \tag{4.1}$$

where m_i, Ψ_i and E_i are respectively the effective mass, the potential, the wave function and the energy for electrons ($i = e$) and holes ($i = h$). Here, the potential $V_i = H_{C_i} + H_{V_i}$ is due to the confinement potential H_C (see figure 4.2) and the applied electric field H_V.

Solving equation 4.1 numerically (matlab code provided by François Chiaruttini), one can determine the possible electron-hole transitions in this structure.

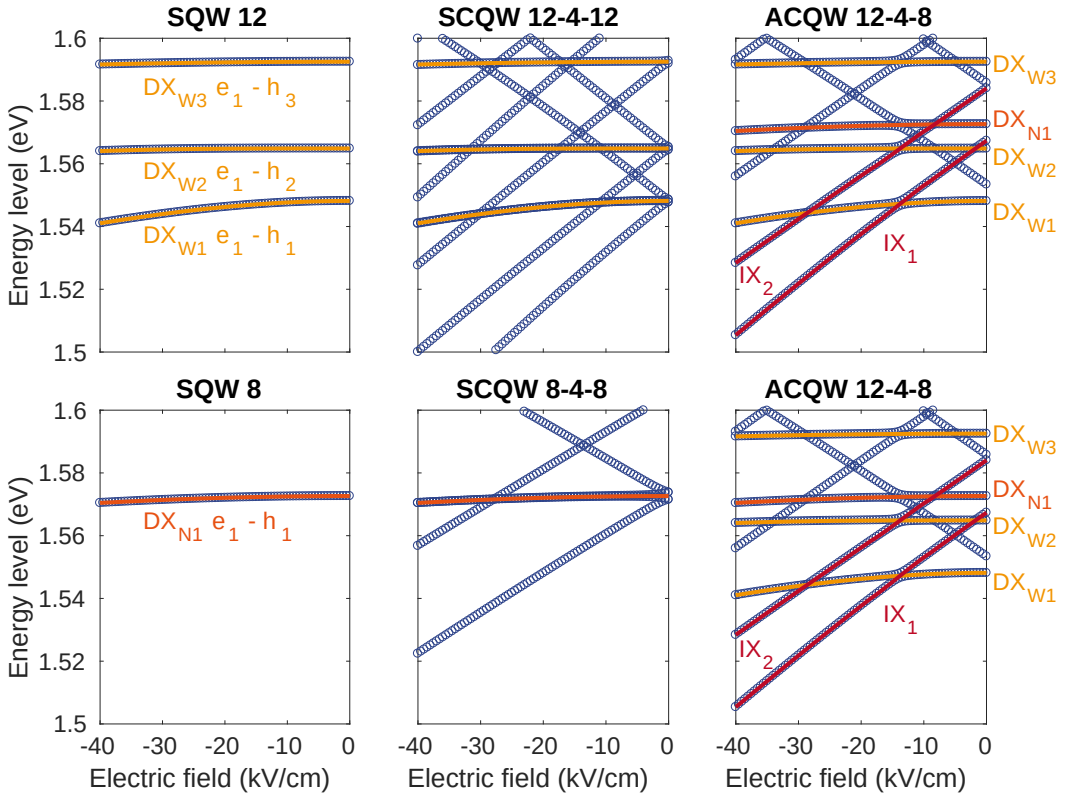

Figure 4.5: Numerical resolution of Schrödinger equation for five different structures (blue red circles). Left panels: Two different single QW (8 nm and 12 nm). Middle panels: two different symmetric CQW (8 and 12 nm wells respectively, and 4 nm barrier). Right panels: asymmetric CQW we study here (8-4-12 nm for the first well, the barrier, and the second well). Solid lines identify electron-hole transitions which correspond to direct and indirect excitons in these structures.

The evolution of several of the lowest electron-hole transition energies as a function of the electric field along the growth axis is shown in figure 4.5. Five cases are considered: two single QW (SQW) corresponding to the QW of our structure (8 and 12 nm), two symmetric CQW with the same width than SQW (8-4-8 nm and 12-4-12 nm respectively) and our asymmetric CQW structure (12-4-8 nm).
In SQW, the transitions do not vary much with the electrical field. The lowest in energy transition in the thinner SQW has an higher energy than the first excited transition of the wide SQW. They are attributed to DX transitions. They exist also in the corresponding symmetric CQW and both of them exist in the asymmetric CQW (yellow and orange solid lines).
In symmetric CQW structures, these direct transitions are still present but they are degenerate because the two wells are identical. The electric field lifts this degeneracy. These interwell transition energies correspond to the IX states and shift linearly with

the electric field.
In the asymmetric CQW, the direct transitions of both 8 nm and 12 nm SQW are present. They are denoted as DX_N and DX_W respectively. Indexes denote the energies of excited states. Here, the electric field mixes the excited states and the observed indirect transitions (red solid lines) are different from the symmetric CQW.

* *
*

In what follows, we compare the calculated transition energies with the experimental data from photoluminescence and excitation of the photoluminescence (PLE) in order to identify the excitonic transitions.

4.3 Photoluminescence Setup

The used setup allows us to make both time-integrated and time-resolved measurements. The sample is placed in the variable temperature insert of a He flow cryostat allowing measurements at 2 K and at variable gate voltage. To do so, the sample mount and holder of the magneto-optical cryostat have been modified to provide electrical connection. The sample is also mounted on a socket for semiconductor devices (see figure4.6). The bonding has been realised in the Montpellier University clean-room by Christophe Roblin.

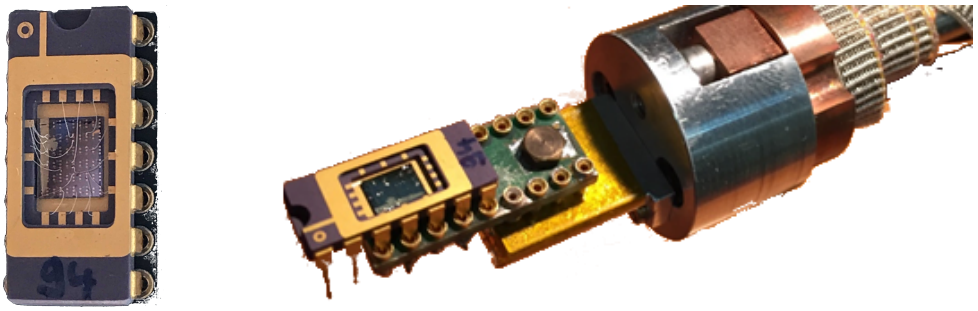

Figure 4.6: Left: picture of the sample mounted on the socket with 14 contacts. We can see the bonding wires. They provide the electrical contact for top electrode of 13 traps and one contact with the bottom electrode. Right: picture of the sample at the end of the electrified mount and holder.

Excitons in the CQWs are created by optical excitation (with different power, wavelength, polarisation, with either pulsed or continuous wave (cw) excitation). The cw excitation is provided by tunable Ti-Sapphire laser (Spectra-Physics T3900). The pulsed excitation is provided by an ultrafast Ti:Sapphire oscillator (Spectra-Physics Tsunami).

The laser beam passes through the spatial filter and its polarisation state is tailored, with a half (for linearly polarised excitation) or quarter (for circularly polarised excitation) waveplate. Then, it is focused on a 20 μm spot in the center of the electrostatic trap. The spot position on the surface is monitored by the web camera (see figure4.8). The PL collected by the same lens passes through the NPBS, and then it is focused on the 50 μm-wide slit of the spectrometer. The spectrally resolved signal is analysed by cooled CCD camera.

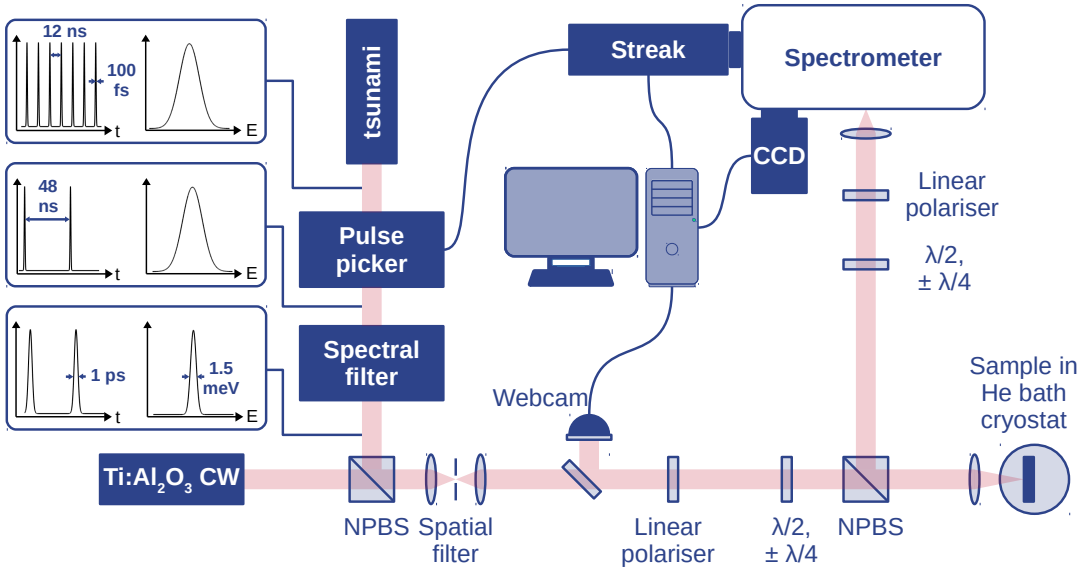

Figure 4.7: Sketch of the PL setup. Focus on the sample and positioning in the center of a trap is monitored by the web-camera. This setup allows both polarisation-resolved and/or time-resolved measurement.

For time-resolved measurements, both the excitation and the detection are modified. The ultrafast Ti:Sapphire laser delivers 100 fs pulses at 82 MHz frequency which are sent to a 4f dispersion line. This spectral filtering ensures a narrow energy band excitation. The resulting pulse duration is about 1 ps, and the spectral width is 1.5 meV (which is well below the 25 meV splitting between the DX_W and the DX_N transitions see figure 4.1). We use a home-build pulse picker to reduce laser repetition rate down to 20 MHz in order to avoid exciton accumulation between pulses. For the detection, the signal is analysed by the streak camera which is synchronised with the pulse picker.

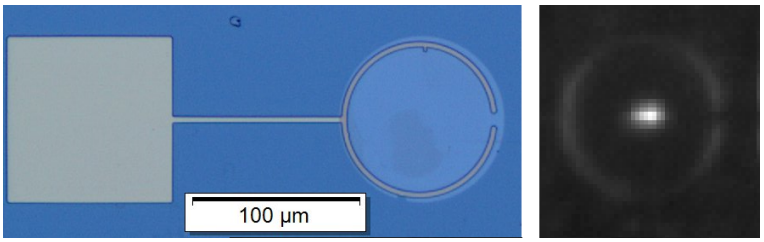

Figure 4.8: Top view of a 100 μm trap (microscopy) and image from the CCD for the positioning of the 20 μm diameter spot into the trap. The sample is illuminated with white light allowing for the visualisation of the thin gold electrode at the edge of the trap.

4.4 Continuous wave measurements

The first paragraph of this section will describe the setup we used to perform PL measurement. Then, results are presented and discussed in order to understand the studied system.

4.4.1 Identification of optical transitions

The identification of the optical transitions relies upon the comparison between the excitation of the photoluminescence spectra and simulations (see section 4.2).
PLE measurements in Trap 2 for two different values of V_G are shown in figure 4.9. They are performed at 2 K. The x-axis correspond to the detection and the y-axis corresponds to the excitation energies. When the detection energy corresponds to the excitation energy, we observe a sharp peak due to the laser. We observe a broad band and several narrow peaks.

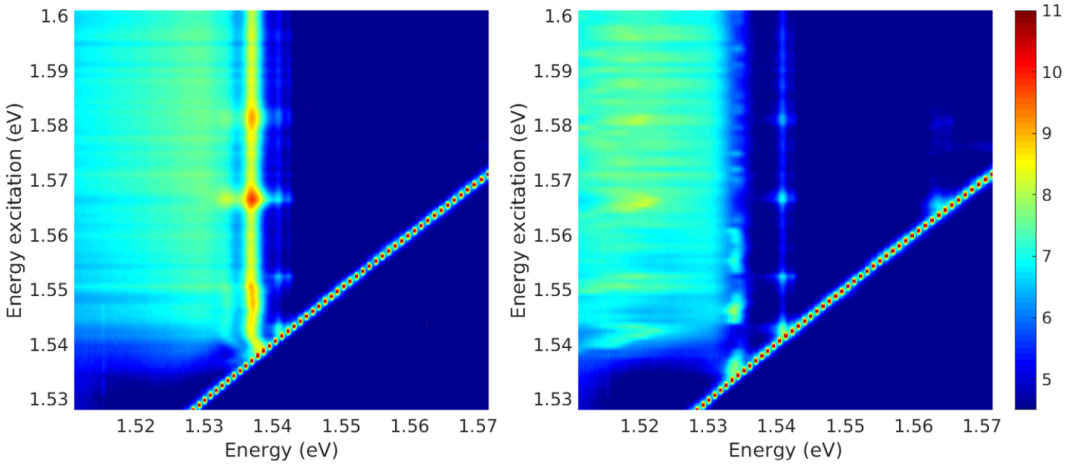

Figure 4.9: PLE spectra in Trap 2. Intensity is color-encoded in logarithm scale. Right panel: $V_G = -1$ V, left panel: $V_G = 0$ V. Experimental conditions: $P_{exc} = 40\mu W$ and $T = 2$ K.

The ≈ 20 meV-broad emission line present in the two figures can be attributed to the emission of the n^+ layer. In both cases, we observe a two-peaks structure emitting at ≈ 1.541 eV. The intense line emitting at 1.538 eV at $V_G = 0$ V disappears at $V_G = -1$ V and a weaker and broader line appears at 1.52 eV at $V_G = -1$ V. Finally, a weak peak emits at 1.538 eV under negative bias. We also distinguish four resonant excitation energies easily identifiable on the two-peaks structure at 1.541 eV.

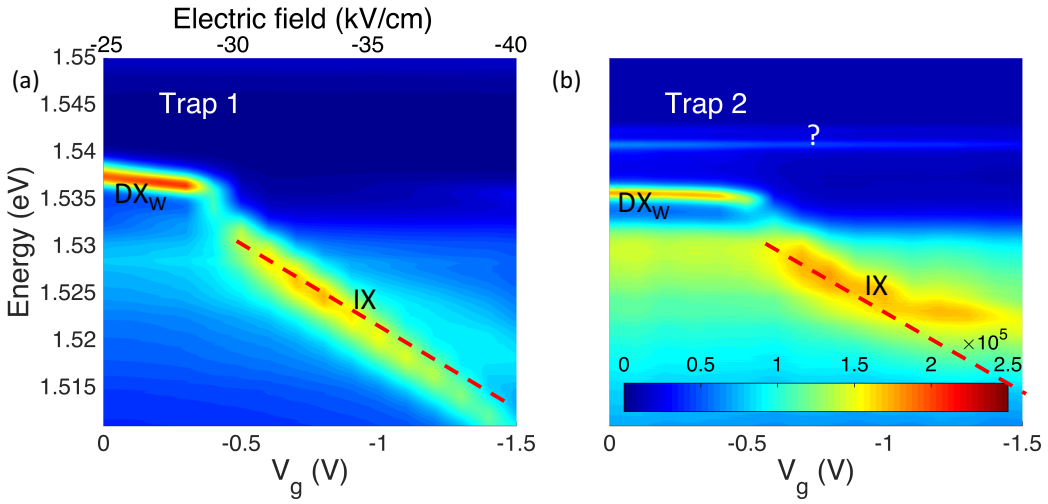

Figure 4.10: Variation of PL spectra with applied voltage in Trap 1 (left panel) and Trap 2 (right panel). Experimental conditions: excitation is resonant with the narrow well ($E_{exc} = 1.568$ eV) $P_{exc} \approx 10$ μW and $T = 2$ K.

Photoluminescence spectra in Trap 1 and Trap 2 at applied bias V_G from 0 to -1.5V are shown in figure 4.10. Measurement are performed at 2 K for an excitation at $E_{exc} = 1.568$ eV (which corresponds to the DX_W transition, see below) with a power $P_{exc} \approx 10\mu W$.

It appears that the two traps do not show the same behaviour. First, the line at $E_? = 1.542$ eV detected in Trap 2 is not present in Trap 1. This line, denoted as "?" in figure 4.10 and figure 4.11, does not shift when the voltage is applied, and its intensity remains constant.

The second point is that the bias induced shift of the IX emission is not identical in the two traps. Dashed lines on top of the color maps show the position of the IX energy as a function of V_G estimated from electric field dependence of the electron-hole transition energies (see figure 4.5). While for Trap 1 (at least for $V_G < -0.5$ V) IX energy shifts faster than expected, in Trap 2 the behaviour is opposite. This means that for a given value of V_G the electric field may not be exactly the same in the two traps. Note also, that the change in the slope of energy as a function of the gate voltage and jump in the IX energy observed at ≈ −0.3 V is apparently related to

the level crossing between DX_W and IX levels that can be seen in figure 4.5. From comparison between the calculated levels we conclude that range of the electric fields accessible between 0 and 1.5 V lies between 25 and 40 kV/cm.

PLE spectra from figure 4.9 combined with corresponding PL spectra from figure 4.10 allow for the identification of the observed transitions. For convenience, representative PL and PLE spectra for $V_G = -1V$ and $V_G = 0$ are shown in figure 4.11.

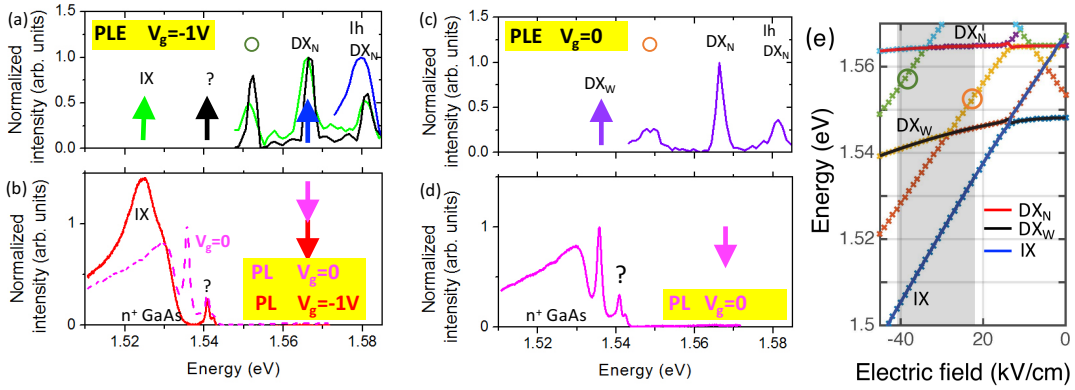

Figure 4.11: PLE (a, c) and PL (b, d) measurements in Trap 2 at $V_G = 0$ (c, d) and $V_G = -1$ V (a, b). Arrows indicate PLE detection (a, c) and PL excitation (b, d) energies. In (b) dashed line shows $V_G = 0$ PL spectrum for comparison with $V_G = -1$ V. Open cercles indicate the optical resonances corresponding to excited states indicated in panel (e)

They enable us to identify of the two DX resonances, DX_W at 1.538 eV and DX_N at 1.565 eV which are separated by $\approx$ 25 meV, as expected from the solution of Schrödinger equation. Additional peaks in PLE can be attributed to the direct transition involving light hole in the narrow QW (lh DX_N at $E = 1.583$ eV), and to the two indirect transitions at lower energies. They are shown by circles in figure 4.11.

The PLE spectrum detected at DX_N energy (blue line) demonstrates that DX_N is resonantly excited when the DX transition involving the light hole in the same QW is pumped.

The PLE spectrum detected at the energy of the non-identified resonance $E_? = 1.542$ eV (black line) presents peaks as the spectrum detected at IX energy (green line), suggesting that it originates from the CQWs as well.

PL spectra are picked from figure 4.10 and are normalised to the "?" peak intensity. Similarly to the PL spectra measured in Trap 1, one can clearly distinguish three features: DX_W emission at $V_G = 0$, IX emission at $V_G = -1$ V, and the broad emission line that can be attributed to the emission of the n^+ layer. The latter

emission complicates the analysis of the IX spectrum under CW excitation, while it can be separated in time-resolved experiments due to long lifetime of IXs.

4.4.2 Polarisation of the photoluminescence

At that point, we have identified the IX transition and we know how it shifts with V_G. Therefore we now have to define the conditions whereby the polarisation of the PL is optimal. To do this, we excite the Trap 1 with circularly polarised light and resolve the co-circular and the counter-circular polarisation of the PL for V_G from zero to -2 V. Figure 4.12 shows the polarisation rate of the PL.

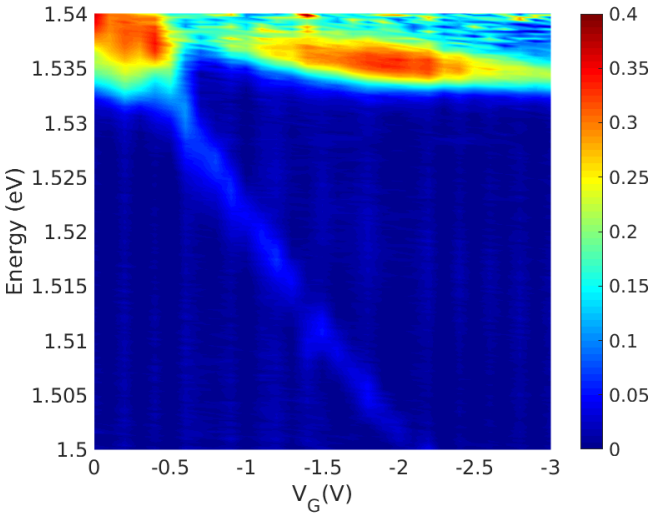

Figure 4.12: Polarisation of the PL calculated as $\mathcal{P}_c = (I_{\sigma^+} - I_{\sigma^-})(I_{\sigma^+} + I_{\sigma^-})$. Measurements comes from measurement shows in figure 4.10. Experimental conditions: excitation is resonant with the narrow well ($E_{exc} = 1.568$ eV) $P_{exc} \approx 10$ μW and $T = 2$ K

The DX_W is strongly polarised (up to 35%) and displays a minimum at voltage corresponding to the appearance of the IX transition. Polarisation of IX transition is weaker (in the order of 5%) and does not vary by much with V_G. Once again, the n^+ layer is an inconvenience. Indeed, this low polarisation rate can be imputed to the intensity ratio between the IX transition (which is low because of the low IX oscillator strength) and the n^+ layer. In this configuration we are not able to observe any variation of the polarisation with the applied voltage.

In conclusion, we successfully identified the main resonances and observed the transition from a DX ground state to an IX ground state applying V_G. We have also faced technical issues. The presence of an emission from the n^+ layer makes it difficult to study the IX emission. Indeed, the oscillator strength of the IX transition

is such that its PL emission is weak and, as we see in figure 4.10, the more indirect excitons are, the weaker the PL intensity is.
Moreover, the polarisation of the emission from the IX is very weak. It can be imputed to the n^+ layer. Indeed, its emission could not be polarised and is added to the emission from the IX, decreasing the total polarisation.
The IX energy dependence on the gate voltage is not the same in trap 1 and 2 and even in a given trap, each scan of V_G could give not identical slope. This could be attributed to a carrier trapping. It results in the electrostatic environment which vary at each scan of the gate voltage and at each scan of the temperature.

* *
*

The problem of n^+ layer could be circumvented in time-resolved measurements because the emission from the n^+ layer should not have a long lifetime. The following section is dedicated to time resolved measurements which enable studying the density and spin dynamics of IX.

4.5 Time resolved photoluminescence

Being able to identify the IX emission is PL spectra, we now perform time-resolved photo-luminescence (TRPL). Unfortunately, the emission of n^+ layer keeps us unable to determine the optimal gate voltage corresponding to the highest polarisation rate. Thus, we will study the evolution of TRPL spectra with V_G. In what follows, all measurements have been performed in Trap 1.

4.5.1 Results

Identification of the signal due to IX We compare the TRPL of the DX_W ($V_G = 0V$) transition and the IX ($V_G = -0.9V$) transition in Trap 1. Color-encoded TRPL spectra are shown in figure 4.13 in logarithmic scale ((a) and (b)). We used a linearly polarised excitation resonant with DX_N (power is $P_{exc} = 7\mu W$) with picosecond laser pulses.

At $V_G = 0$ (figure 4.13(a)), there is no long-living signal. We therefore use the streak in a short time range (0 to 5 ns) in order to have a sufficient resolution. We observe two contributions. The first one is intense and localised around 1.537 eV. It is therefore attributed to the DX_W transition (see figure 4.11). The second one is broader and weaker. Its energy range corresponds to the emission of the substrate.
At $V_G = -0.9$ V (figure 4.13(b)), there is a broad emission during ≈ 1 ns and a

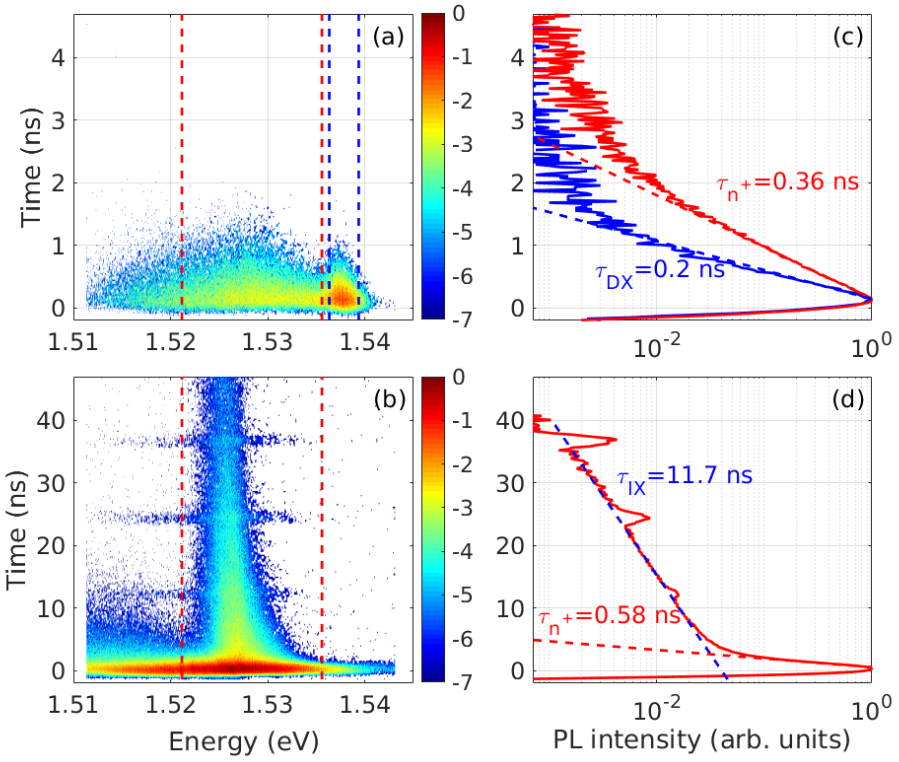

Figure 4.13: Time-resolved PL spectra at $V_G = 0$ V (a) and $V_G = -0.9$ V (b) in Trap 1. PL intensity is represented in logarithmic scale. Respective spectrally integrated PL are shown beside ((c) and (d)). Their color correspond to the color of the window used for spectral integration which are represented with dashed lines in (a) and (b). Experimental conditions: $P_{exc} = 7$ μW, E_{exc} is resonant with DX_N, $T = 2$ K

much thinner one which persists for more than 40 ns. Three horizontal lines appear. They correspond to the incomplete suppression by the pulse picker of the laser pulses delivered at 82 MHz. We have checked that the resulting perturbation of the system is weak enough to not be important for the hereafter analysis.

Spectrally integrated spectra are shown beside (figure 4.13(c) and (d)). Integration windows are shown in dashed lines. At $V_G = -0.9$ V, the red dashed line corresponds to a wide window around the IX emission but also includes the n^+ layer emission, as we have seen at $V_G = 0$ V. At $V_G = 0$ V, we use the same window (red dashed line) to study the decay of the n^+ layer emission. The blue window corresponds to the DX_W emission. At $V_G = 0$ V, decays are exponential. It appears that the DX_W emission is not only shorter than the IX but also shorter than the n^+ layer emission. Radiative times extracted from exponential fits (dashed lines in figure 4.13(c)) are actually $\tau_{n^+}(V_G = 0) = 0.36$ ns and $\tau_{DXW}(V_G = 0) = 0.2$ ns. At $V_G = -0.9$ V, the decay is bi-exponential. The short contribution attributed to the n^+ layer. The much longer

one which is attributed to the IX emission. From bi-exponential fit (dashed lines in figure 4.13(d)), we extract $\tau_{n^+}(V_G = -0.9) = 0.58$ ns and $\tau_{\mathrm{IX}}(V_G = -0.9) = 11.7$ ns. Values of τ_{n^+} obtained at $V_G = 0$ and $V_G = -0.9$ V are similar.

Evolution of IX lifetime with electrical field We now study the evolution of the IX emission line with V_G. Figure 4.14 shows color-encoded images of TRPL spectra (in logarithmic scale) at four different gate voltages, from -0.7 V to -1.5 V. Excitation conditions are identical to those of figure 4.13.

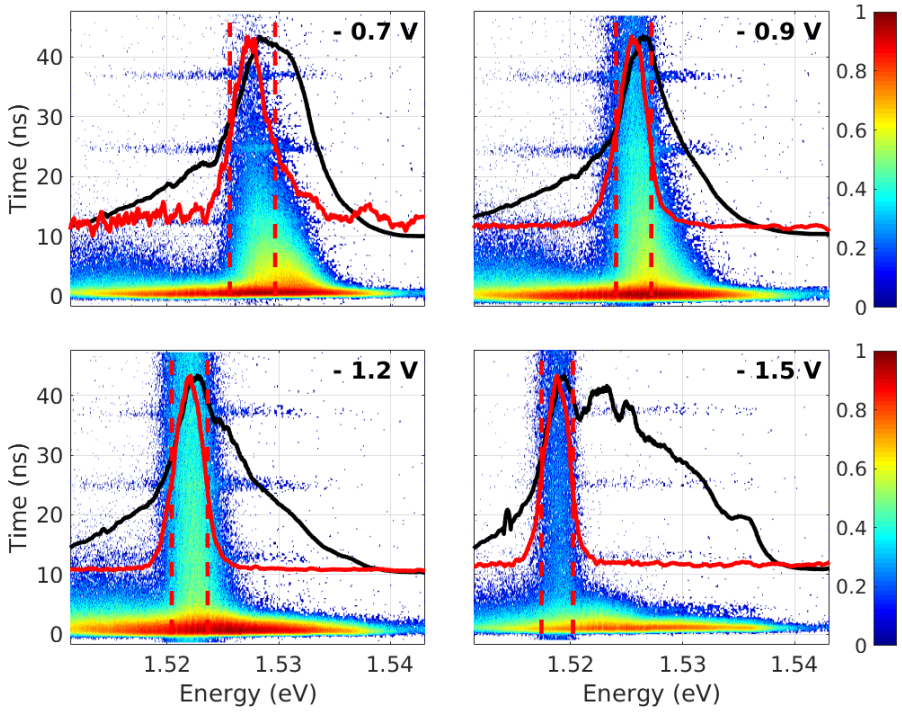

Figure 4.14: Time-resolved PL spectra for different values of V_G in Trap 1. PL intensity is represented in logarithmic scale. Corresponding time integrated PL spectra on the whole time-range (black lines) and for delays higher than 40 ns (red lines) are superimposed onto TRPL images. Red dashed lines correspond to spectral integration windows used for the fits. Experimental conditions: $P_{exc} = 7$ μW, E_{exc} is resonant with DX_N, $T = 2$ K

As we have seen in figure 4.13, a long-living spectrally narrow emission replaces at long delay the very broad and intense emission of the first ns. The former is attributed to the IX and the latter is attributed to the n^+ layer.

We now focus on evolution of the IX emission with V_G. The energy of the IX long-living contribution shifts with V_G. We can also notice a variation of the lifetime with V_G.

A qualitative analysis of the evolution of this lifetime with V_G require a spectral integration of the PL spectra. In order to perform such an analysis, we chose to

integrate the spectrum over a spectral window centred on the maximum of the time integrated PL spectra obtained for delays longer than 40 ns. The width of this window is determined by the full width at half maximum of the same time integrated PL spectra. These windows are shown on top of the TRPL images by red dashed lines. Note however that the long-living component is slightly red-shifted as a function of time. This is presumably due to the decrease of IX density and will be discussed below.

The resulting integrated PL intensity decays are shown in figure 4.15.

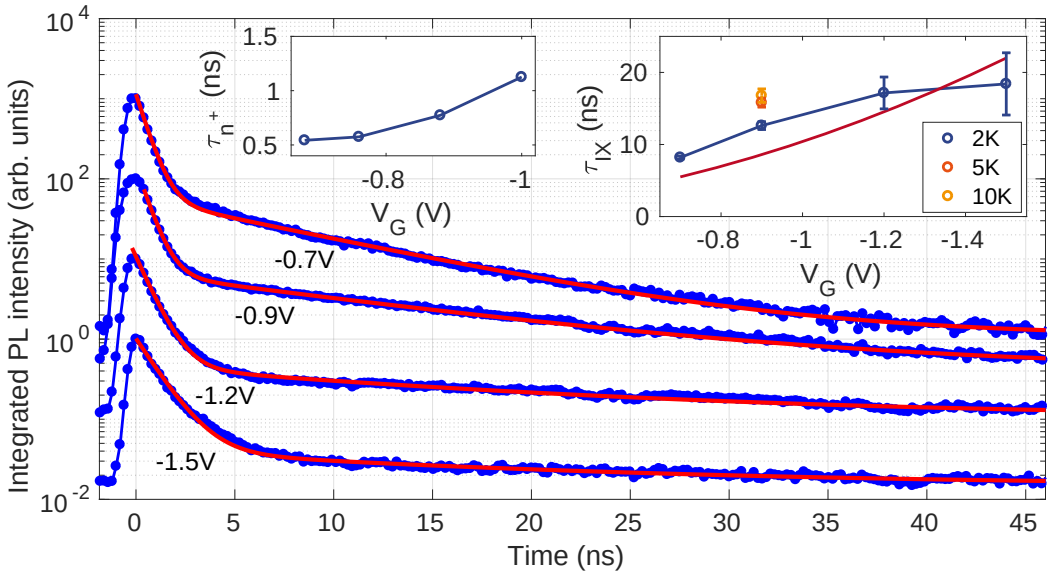

Figure 4.15: Spectrally-integrated TRPL spectra for different values of V_G in Trap 1 (blue solid lines). The PL intensity is represented in logarithmic scale and data are shifted vertically. Corresponding bi-exponential fit are shown in red dashed lines. Insets show the decay times extracted from fits (short time (a) and long time (b)). $P_{exc} = 7$ μW, E_{exc} is resonant with DX_N, $T = 2$ K

The data are shifted vertically, and the spurious peaks at 12, 24 and 36 ns are filtered out for the sake of the presentation clarity. On top of the data the results of the fitting to the bi-exponential decay are shown (dashed lines). The resulting decay times are summarised in inset.

Because IX and n^+ are spectrally superposed, the shortest decay time τ_S in inset (a) is expected to be a mixture of the lifetime of the photo-carriers in the substrate and in the QW, and thus increases with V_G [28]. The longest decay time, which increases in the studied range of V_G from roughly 10–20 ns (inset (b)), can be identified as the lifetime of IXs. This time is expected to be controlled by the gate voltage-dependent coupling between DX and IX states. Indeed, the energy splitting between IX and DX (DX_W in our case) decreases linearly when increasing V_G. The lifetime of IX has been shown to depend quadratically on the energy difference between DX and

IX [6, 29]. Such dependence recalculated in terms of V_G is shown in inset (b) by the solid line. One can see that it does not match perfectly the experimental data, which exhibit rather sublinear dependence on V_G . Note also that the lifetime we measure is shorter than expected from the measurements on similar samples [2, 6]. This suggests that some additional mechanisms we could not identify in this work are involved in the IX recombination dynamics.

Estimation of the exciton density Due to the spatial separation and the electrical charge of their constituents, IX are aligned electrical dipoles. Interactions between such dipoles screen the electric field along the z-direction leading to a blueshift of the IX emission at high densities. The relation between this blueshift and the IX density could be quite complex due to exciton-exciton interaction. We limit ourselves here to the simplest model of non-interacting IXs [30].
The slight time variation of the center of the IX emission seen in figure 4.14, can be attributed to this phenomenon. Excitons recombine progressively, their density - and thus their energy - decreases.

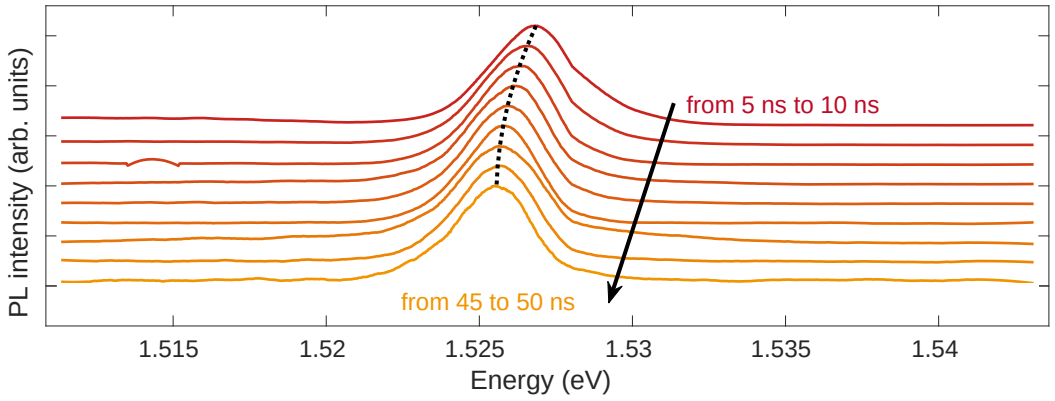

Figure 4.16: IX PL spectra integrated over successive 5 ns windows at $V_G = -0.9$ V. Spectra are extracted from figure 4.14 and smoothed. Black dashed line is a guide for the eye.

Figure 4.16 shows successive time-integrated PL spectra every 5 ns from the first 5 ns to the end of the time range (50 ns). The energy corresponding to the maximum of the PL spectra decreases and finally stabilises (see black dashed line). The corresponding energy shift is about 1.5 meV from which we can evaluate the exciton density.
In the simplest - the plate capacitor - approximation, the energy blueshift and the exciton density are proportional $E_{bs} = u_0\ n_x$ and the ratio is given by [31]:

$$u_0 = \frac{e^2 d}{\epsilon_0 \epsilon_b} \tag{4.2}$$

where d is the distance between the electron and the hole, and ϵ_b is the background relative permittivity.
In our sample, $d = 14$ nm (taking the centre of the two QW), $\epsilon_b = 12.9$ in GaAs and we can determine $u_0 \approx 1.9\ 10^{-10}\ meV/cm^2$. The energy shift 1.5 meV therefore corresponds to a density of 7.6 $10^9 cm^{-2}$.
For this density, the corresponding quantum degeneracy temperature is ≈ 2 K. Darkenning of the IX emisison have already been reported at pumped Helium temperatures. Morever, the plate capacitor approximation may underestimate the IX density up to a factor 10 [32, 33]. Thus, in principle we can deal here with some collective excitonic effects.

IX spin dynamics In order to study IX spin relaxation we use circularly polarised excitation and analyse the decay of the emission in co- and counter-circular polarisation using variable quarter wave plate. Laser energy is resonant with DX_N transition, so that spin polarised electrons and holes are created in the narrow quantum well. In the absence of the external electric field, optically created spin polarisation of DX disappears in tens of picoseconds. Indeed, due to exchange interaction between electron and hole, exciton momentum scattering constitutes an efficient channel for the spin relaxation (Maialle-Andrada e Silva-Sham mechanism) [34, 35]. In the presence of the reverse bias, electrons tunnel to the wide quantum well and form IXs. The tunnelling (typically on the picosecond time scale) is even faster than DX spin relaxation, therefore spin polarisation can be at least partially conserved in this process [36]. While the spin polarisation of holes is lost on the same scale as the electron tunnelling time, spin relaxation of IXs is much slower than that of DXs, and limited by the electron spin relaxation [3, 6, 7, 37, 38]. This is the result of the spatial separation of the electron and the hole within IX. Assuming infinitely fast hole spin relaxation, one finds that spin relaxation time of the electron within IX τ_e is equal to decay time of the PL polarisation τ_p that can be measured experimentally [3, 7, 34].
The spectrally integrated intensity of PL for two opposite helicities (I_+ and I_-) is shown in figure 4.17 (a) for $V_G = -0.9$ V and $T = 2$ K. One can see that, at short delays, the emission intensity is not polarised. This is because the signal is dominated by the emission of the n^+ layer. The intensity difference between the two polarisations becomes clearly visible only after roughly 5 ns, when the n^+ contribution disappears. Subsequently, it fades away at longer delays. Figure 4.17 (b) shows the circular polarisation degree, $\mathcal{P}_c = \frac{I_{\sigma+} - I_{\sigma-}}{I_{\sigma+} + I_{\sigma-}}$, extracted from these measurements. The presence of the unpolarised emission from the n^+ layer masks the IX polarisation degree and its decay during several nanoseconds following the excitation. The initial

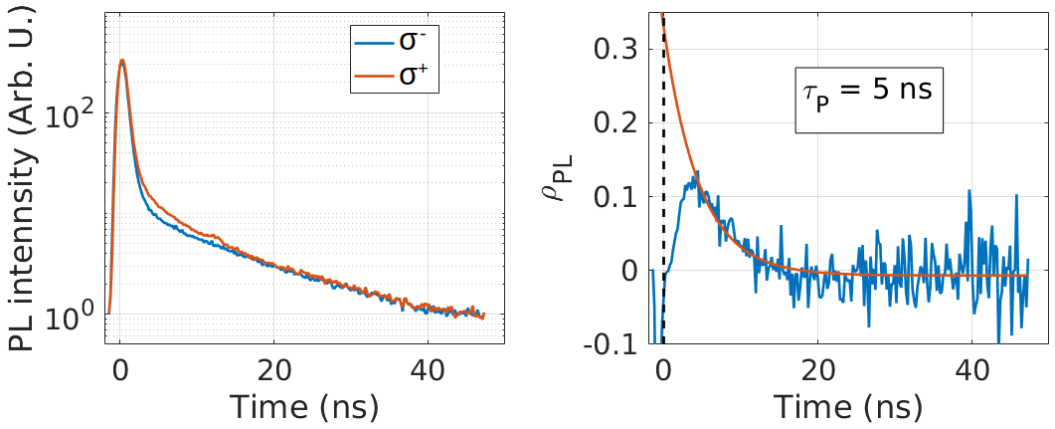

Figure 4.17: (a) Spectrally integrated, polarisation and time-resolved PL measured under σ^+ excitation in the same conditions as an figure 4.15, $V_G = -0.9$ V, $T = 2$ K. (b) Circular polarisation degree of PL extracted from (a) are shown by open circles. Solid line is the exponential decay fit to the data. The initial build-up of polarisation results from the faster decay of the unpolarised emission from the n^+ layer, as compared to polarised emission of the IXs.

build-up of polarisation results from the faster decay of the unpolarised emission from the n^+ layer, as compared to polarised emission of IXs. Thus, exponential fit of the decaying part of the data allows for the determination of not only the decay time τ_p - and hence τ_s - but also of the initial degree of polarisation of the IX emission $\rho_c(t = 0)$. This fit is shown by solid line in figure 4.17 (b) and yields $\rho_c(t = 0) = 0.3$ and $\tau_p = 5$ ns. The decay of the PL polarisation degree is just the spin lifetime for the IX, $\tau_p = \tau_s$.

4.5.2 Discussion and conclusions

Let us compare IX spin lifetime, τ_s, measured in this work with the results from the literature. The data are summarised in Table 4.1. Only the data on GaAs/AlGaAs CQWs at 2 K are considered, all the results are obtained under resonant circularly polarized excitation of the DX, at low excitation densities, where excitons are presumably localised. Note, however, that the localization degree can only be determined in CW experiments with spatial resolution.

One can see from Table 4.1 that the dispersion of the measured spin lifetime is huge, and the measured values do not show any clear correlation neither with the excitation type (CW *versus* pulsed) nor with the dipole moment of the IXs. The value $\tau_p = 5$ ns measured in this work is among the shortest spin lifetimes measured. The reasons for that are difficult to identify. Nevertheless, the sample seems to be suitable for considering the implementation of the pump-probe experiments suggested in reference [24] and presented in section 4.1. Because the experimental conditions

source	d (nm)	τ_s(ns)	pulse duration	PL/pump-probe
Beian *et al.* [2]	12	18	50 ns	PL
Leonard *et al.* [3]	12	10	CW	PL
Violante *et al.* [4]	19.5	6	CW	PL
Kowalik-Seidl *et al.* [5]	12	> 80	400 ns	PL
Andreakou *et al.* [6]	12	9	1 ps	pump-probe
Finkelstein *et al.* [7]	16	22	CW	PL
This work	14	5	1 ps	PL

Table 4.1: Summary of the data from the literature. Only GaAs/AlGaAs CQWs are considered, d stands for the separation between the QW centres, τ_s is measured IX spin relaxation time. The last two columns indicate the type of experiment used to extract τ_s: either from space, or from time-resolved measurements (laser pulse duration is indicated in later case), either using PL or pump-probe spectroscopy.

chosen in this work are very similar to the ones used in reference [6], we expected to get new insights into the dark exciton spin and population dynamics using this asymmetric CQW sample.

* *
*

The next section is dedicated to the study of spin dynamics in Trap 1 with pump-probe spectroscopy and provides complementary information.

4.6 Spin dynamics in ACQW by pump-probe spectroscopy

This section deals with to the study of spin dynamics in Trap 1 by pump-probe spectroscopy. All these measurements have been performed at Dortmund university in the E2 team under the supervision of Vasilii Belykh.
The main goal of these experiments was to detect independently the signal from the two different transitions (wide and narrow QW) in order to reach dynamics of dark IX (see section 1.3.2). Unfortunately, we could not obtained any signal for an excitation resonant with the narrow well. Nevertheless, we measured density and spin dynamics in order to compare with the results obtained in TRPL. We also studied the spin coherence under magnetic field.

4.6.1 Setup

Pump-probe spectroscopy is a two-beams method. As its name indicates, it modifies a system with the pump and probe its state afterwards through a modification of

the probe feature. When the intensity of the reflection of the probe is considered, the method is referred to as time-resolved photo-induced reflectivity (TRPR). When it is the rotation of the polarisation plane of a linearly polarised probe which is considered, the method is referred to as time-resolved Kerr-effect (TRKR).
The varying delay between the two beams is typically controlled using a mechanical delay line. This actually provides a high time-resolution for macroscopic displacements. Because of the light celerity, a variation of one mm corresponds to a resolution of 3 ps. The resulting drawback is the maximum accessible delay. At this celerity, three meters are required to introduce a 10 ns delay and the delay is usually limited by a reasonable length of the delay line. In the previous work on symmetric CQW structure [6] for instance, the maximum accessible delay was 4.5 ns.

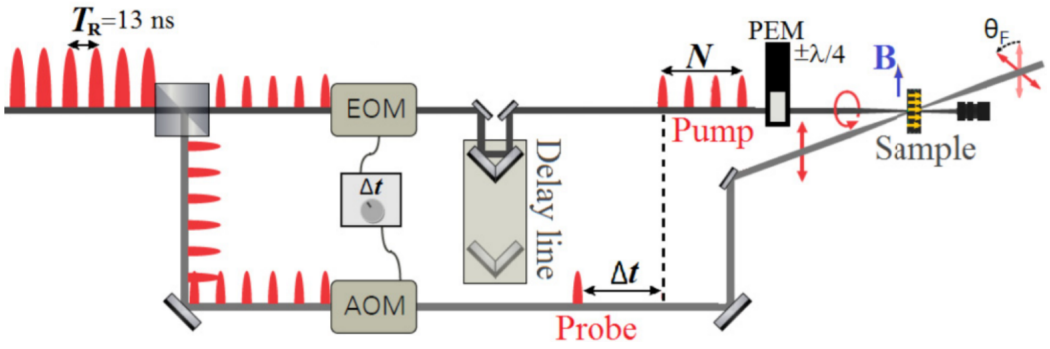

Figure 4.18: Pump-probe setup. Ultrafast pulses are split into pump and probe. EOM and AOM are synchronised in order to control the differential delay in term of $T_R = 13$ ns (period between two pulses). The delay line allows for a fine setting of the delay. Circular polarisation of the pump is modulated by the PEM. The probe is circularly polarised. The detection scheme is not represented here. For our sample we worked in reflection geometry. Thus, the reflected light was collected and analysed using lock-in detection. Figure taken from [39]

We performed both TRPR and TRKR with an extended pump-probe setup proposed by Belykh *et al.* [39]. This setup enables to study submicrosecond spin dynamics with a picosecond resolution. A sketch of this setup is shown in figure 4.18. Here, the delay range between the pump and the probe is extended by sampling one of the probe pulses with an acousto optic modulator (AOM). It enables one to insert a non-limited coarse but well controlled (that means equal to a certain number of pulse delay) delay between the two pulses. Then, a mechanical delay line allows for an additional delay up to 12 ns in order to explore the dynamics at short delays. The challenge lies in the synchronisation between the probe and the pump.
The excitation is provided by a Ti:sapphire laser which delivers 2 ps pulses at a rate of $f_r = 76$ MHz. The laser beam is split into pump and probe. It is important to note that pump and probe have the same energy so that spectral analysis - as in

[6] - is not possible. The probe is sent through an AOM in order to select a single pulse with a controlled $\Delta t = n/f_r$ delay with the pump (here n is an integer). The pump beam passes through a mechanical delay line and its polarisation is modulated between σ^+ and σ^- by a photoeleastic modulator (modulation frequency is 84 kHz) in order to perform lock-in detection. It also avoids an eventual nuclear polarisation [40].

Disabling the AOM and the EOM makes it possible to perform pump-probe spectroscopy in the standard configuration, that means settling for the delay line as the only delay between pump and probe. A predominant particularity of this setup is that the AOM is not able to sample more than one pulse out of 40. That means $n \leq 40$. Thus, the repetition rate of the pump is bound to be either equal to the repetition rate of the laser (standard configuration) or 40 times lower (extended configuration).

4.6.2 Results

Photoluminescence under continuous excitation The experimental configuration being different from our work in Montpellier (different cryostat thus different electrical connection and different cooling condition), we first measured the photoluminescence of our sample for an excitation expected to be resonant with the direct transition in the narrow well ($E_{exc} = 1.565$ eV) and at low power ($P_{exc} = 10$ μW).

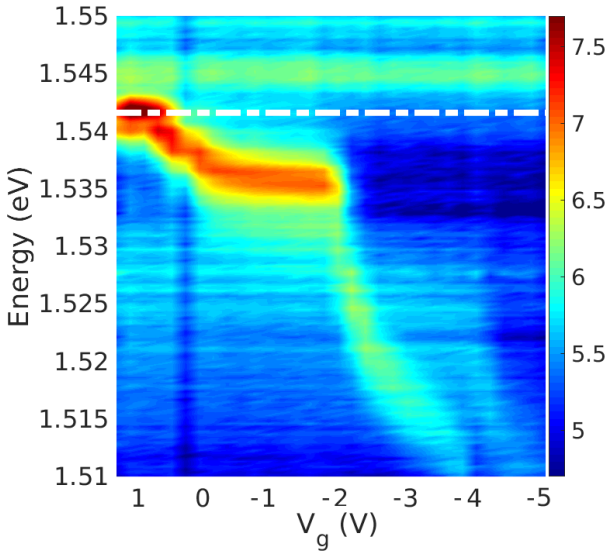

Figure 4.19: Variation of the PL spectra with the applied voltage in Trap 1 (log scale). The dashed-dotted white line corresponds to the excitation energy for the pump-probe experiments discussed below. Experimental conditions: $E_{exc} = 1.565$ eV, $P_{exc} = 10$ μW and T=6K.

In figure 4.19, we observe two lines. The first one corresponds to an energy

$E \approx 1.545$ eV and does not vary with V_G. The second line shifs from $E \approx 1.541$ eV at $V_G = +1$ V to less than $E \approx 1.515$ eV at $V_G < -3$ V. In comparison to what we observed in Montpellier, we attributed this second line to the IX transition. Here, we note that the transition from direct to an indirect transition occurs at positive V_G. Finally, the energy of the direct exciton in the wide well seems to emit a slightly higher (1.541 eV rather than 1.538 eV).

Spin coherence We first realised preliminary measurements in standard configuration (without the AOM). We thus performed TRKR measurements in Voigt configuration varying the gate voltage from -3.5 V to $+1$ V. Transverse magnetic field ranges from 50 mT to 1 T. Excitation energy has been adjusted in order to optimise the signal, corresponding to the direct transition in the wide well. Typical set of data corresponding to three representative values of V_G are shown in figure 4.20 for different applied magnetic field.

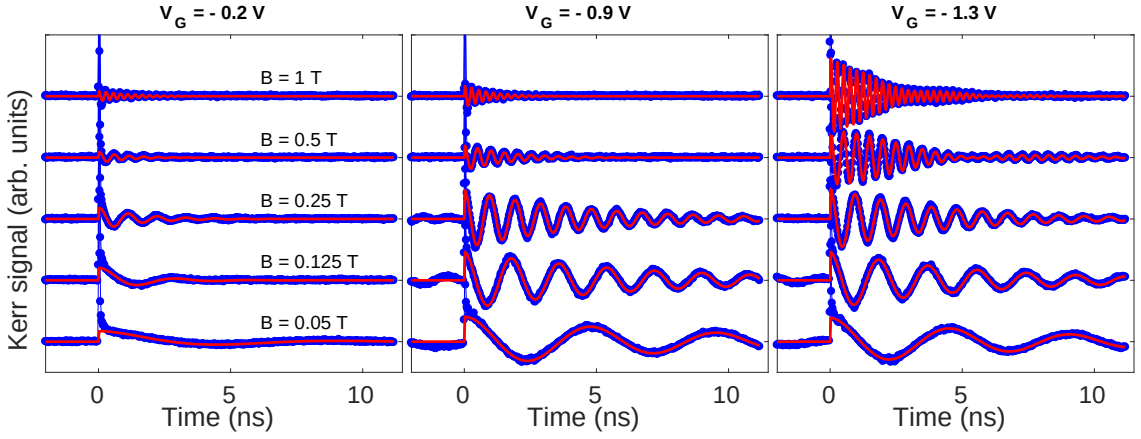

Figure 4.20: Typical TRKR series (blue symbols) and corresponding fits (red solid lines) for $V_G = -0.2,\ -0.9,\ -1.3$ V (left, middle and right panel). Experimental conditions: $T = 6$ K, $P_{pump} = 60\ \mu$W, $P_{probe} = 30\ \mu$W, $E_{laser} = 1.541$ eV

Strong peak at $\Delta t = 0$ ns is the coherent artefact [41] and is not taken into account for the understanding of the system. The signal is presented in arbitrary units. It could correspond to electrical signal from the lock-in amplifier or Kerr rotation angle. For each value of V_G, TRKR scans for different magnetic fields are shifted for convenience.

In figure 4.20, we observe damped oscillations (blue markers) reflecting the precession of electron spins in the plane perpendicular to the applied magnetic field and the spin decoherence characterised by the T_2^* time (spin relaxation and dephasing, see section 1.1.3). Most of data can be fit with exponentially damped cosines function

(red solid lines).

The frequency of oscillations is given by the Zeeman splitting $\hbar\omega_L = \mu_B g B$ where g is the Landé g-factor and $\mu_B = e/2m$ is the Bohr magneton. It therefore becomes shorter when the magnetic field increases.

Spin dephasing affects the coherence time more severely at high magnetic fields. We therefore observe longer decay times at lower magnetic field (three first (bottom) lines for all V_G). The spin relaxation time also increases with $|V_G|$ (see middle and right panels). We can even observe oscillations at negative delays corresponding to a signal subsisting more than 13 ns for low magnetic fields and high gate voltages.

For highest V_G and highest magnetic fields, we also observe beats which are strong clue of the presence of two different contributions (see right panel). In these case, data are fitted with two independent damped oscillations (two last (top) red solid lines in right panel).

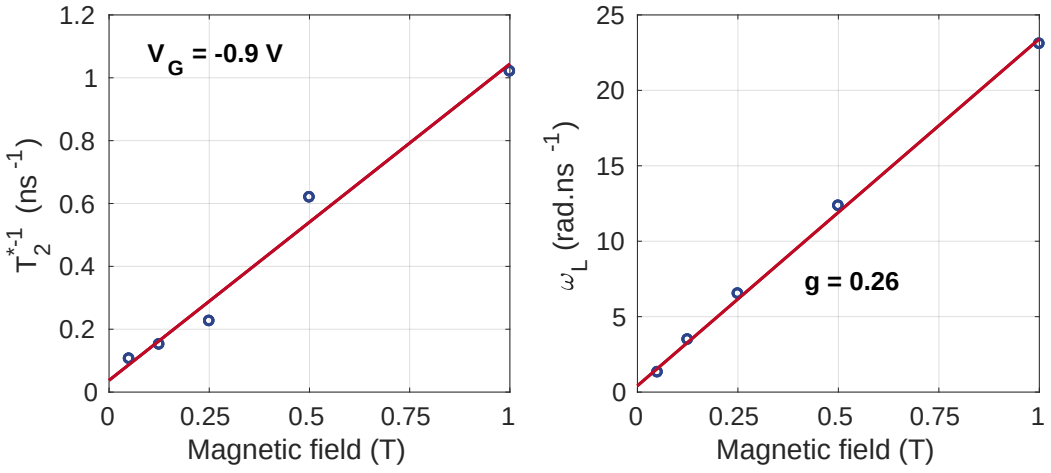

Figure 4.21: Determination of T_2 and g-factor from field dependence of T_2^* and ω_L. Blue circles are Larmor frequencies (right panel) and inverse of T_2^* decay times (left panel) from fits for all values of B at $V_G = -0.9$ V. Red solid lines are linear fits.

For each fit, we can extract the Larmor frequency $\hbar\omega_L$ and the decay time T_2^*. Figure 4.21 shows the magnetic field dependence of T_2^* and of the g-factor at a fixed $V_G = -0.9$ V.

The Larmor frequency is proportional to B. From its linear dependence, we can extract $g = \hbar\omega_L/\mu_B B$. T_2^{*-1} is proportional to B as well (see section 4.6). This linear dependence is given by:

$$\frac{1}{T_2^*} = \frac{1}{T_2} + \frac{\Delta g \mu_B}{\hbar} B \tag{4.3}$$

where T_2 is the spin dephasing time and Δg is the spread of g-factor. A linear fit of the field dependence of T_2^{*-1} provides Δg from the slope and the inverse of the T_2

time from the extrapolated y-intercept.

Finally, fitting the full set of data provides the g-factor, the T_2 time and the g-spread for all the values of V_G. Their variations with V_G are shown in figure 4.22. Variation T_2 with V_G has a peak shape and we observe promising long spin dephasing times up to 25 ns for intermediate $V_G \approx -0.9$ V. Due to the repetition rate of the laser (12 ns), IX accumulate at high V_G. Such an accumulation could explain the decrease of T_2.

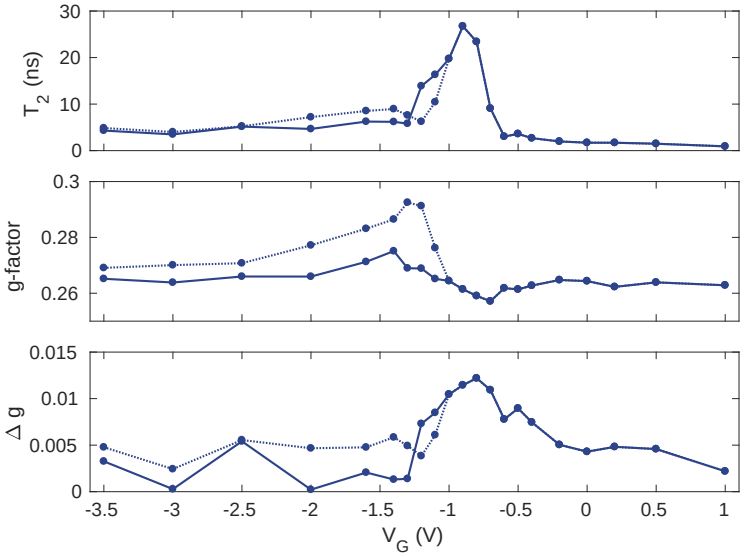

Figure 4.22: Extracted parameters from fits of the whole serie (B = 0.05, 0.125, 0.25, 0.5 and 1 T and V_G from -3.5 to 1 V). For $V_G < -1$ V, two distinct contributions are discernable for $B = 0.5$, 1 T. Thus, we can extract a couple of parameters which are differentiated using solid and dashed lines.

This maximum corresponds also to the onset of two distinct contributions which manifest themselves in beats. These two contributions have slightly different g-factors but comparable T_2 time. The second contribution could come from electrons not bound to an exciton. Their apparition could correspond to electrically injected electrons, for sufficiently high V_G. The presence of free electrons could also explain the decrease of the T_2 time. Their very long spin relaxation time - comparable to the spin relaxation time of bound to exciton electrons - is in contradiction with the results presented in [6]. This should indicate a difference of injected electrons density. It should fianlly be noticed that a similar non-monotonous behaviour has been reported in [2].

Density and spin dynamics using the extended setup We then studied life-time and spin relaxation time with the extended setup. Because the AOM leads to a

drastic diminution of the signal, only a few conditions have been surveyed.
Figure 4.23 shows TRPR measurements for different gate voltages. Here, we do not apply any magnetic field. The same data are shown in logarithmic scale and in linear scale.
We observe a bi-exponential decay with time. The slow component corresponds to very long lifetimes (the signal persisting after 60 ns) that should be related to IX. Thus, we focus on high delays and fit the tail of curves (red dashed lines) in order to extract measured long decay times.

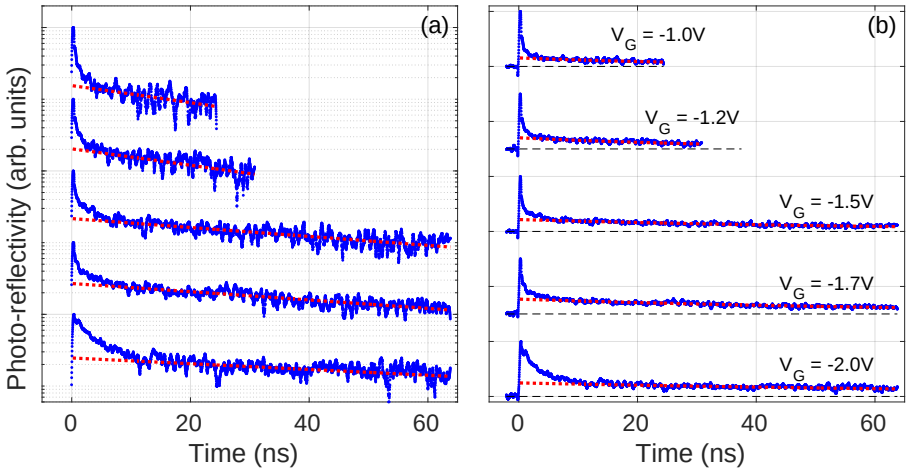

Figure 4.23: Photoreflectivity measurements (blue dots) in log scale to check the slope of fits (left panel) and in linear scale to check the zero at negative delays (right panel). Data are shifted for convenience. Experimental conditions: $T = 2$ K,$P_{pump} = 1$ μW, $P_{probe} = 5$ μW, $E_{laser} = 1.541$ eV, extended setup.

TRKR signal under low magnetic field is shown in figure 4.24. These measurements have not been performed on the same day than previously presented experiments. The electrical behaviour of the structure changing with successive heating and cooling, we first performed measurements in identical experimental conditions but in the standard configuration (by switching on-off the AOM). It allows for the determination of the position of the T_2 peak with V_G. Here, it turns out that the peak occurs for $V_G = -0.6$ V rather than $V_G = -0.9$.
Single damped oscillation fits are shown in red solid lines. Extracted frequencies correspond to the same g-factor but the extended setup enables us to observe the very slow precession in a 5 mT transverse magnetic field. Negative delays correspond to very long times (more than 500 ns) because the AOM releases one pulse out of 40. From the two points at $V_G = -0.6$ V and $T = 6$ K we could extrapolate the value of $T_2 = 25.6$ ns.

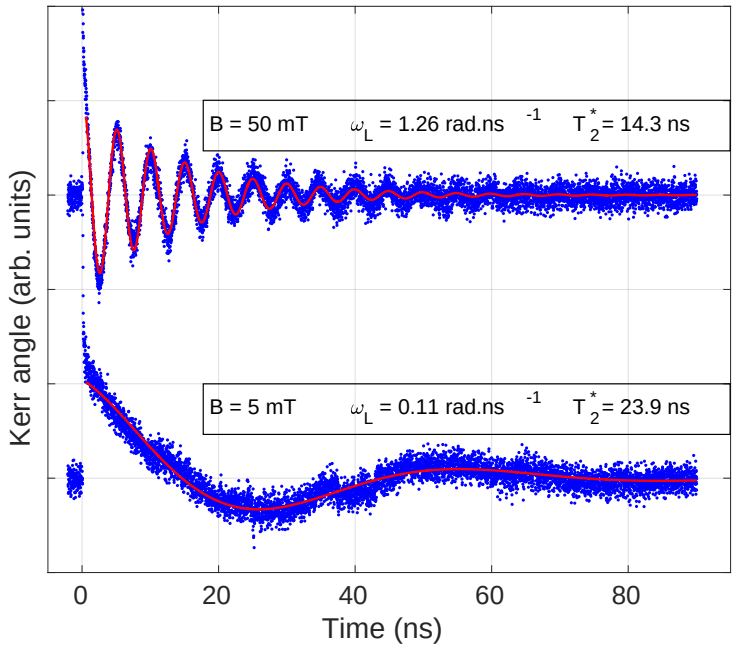

Figure 4.24: Kerr signal as a function of time (blue dots) and corresponding fits (red solid lines). Data are shifted for visibility. Experimental conditions: $P_{pump} = 0.8$ μW, $P_{probe} = 1$ μW, $E_{laser} = 1.541$ eV, $V_G = -0.6$ V, $T = 6$ K, extended setup.

Discussion

Although the ensemble of the performed measurements is not complete, let's summarise the lifetimes and spin relaxation times obtained in pump-probe experiments and compare them with TRPL results.
Figure 4.25 summarises all the extracted times present in logarithmic scale. It is important to note that the blue triangle (the only T_2 time obtained with extended setup) corresponds *a priori* to a maximum in V_G and should be compared with the maximum of green triangles. This is due to the uncontrolled electrical dependence of the sample and indicated in the figure with horizontal errorbars.

Three regimes can be identified: (i) in TRPL, our AOM picks one pulse out of four and the repetition rate is 82 MHz, successive pulses are thus separated by 48 ns; (ii) in standard pump-probe setup, two pulses are separated by 13.1 ns; (iii) in extended pump-probe setup, $40 \times 13.1 = 524$ ns separate two successive laser pulses. In addition to these delays, excitation power and spot size were also different for each regime. In TRPL, we used $P_{exc} = 7$ μW and a 20 μm diameter spot while typical powers used in pump-probe spectroscopy were $P_{exc} = 60$ μW and $P_{exc} \approx 1$ μW in standard and extended configurations respectively and a 100 μm diameter spot. For a laser energy of $E_{laser} \approx 1.55$ eV, these different regime can be

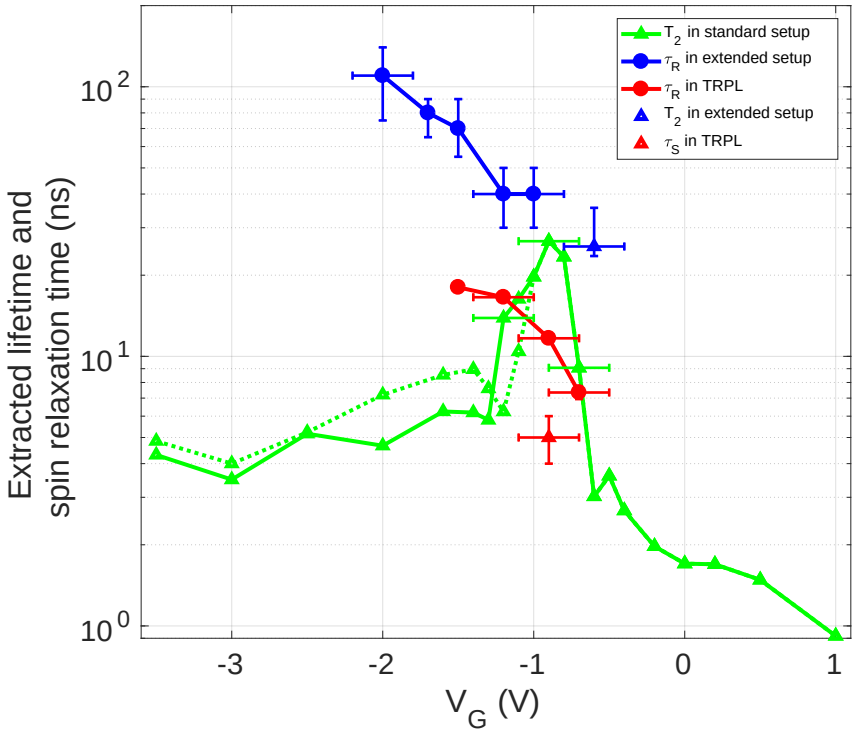

Figure 4.25: Lifetimes (circles) and spin relaxation times (triangles) obtained with PL (red symbols), standard pump-probe setup (green symbols) and extended pump-probe setup (blue symbols).

compared using the corresponding photon density per pulse. We respectively obtain $n_{exc}^{TRPL} = 6.8 \times 10^{11}$ cm^{-2}, $n_{exc}^{stand} = 6.3 \times 10^{10}$ cm^{-2} and $n_{exc}^{extend} = 4.2 \times 10^{10}$ cm^{-2} which are expressed in number of photon per square centimeter and per pulse.
The longest lifetimes are obtained in regime (iii) for which no accumulation can occur. In TRPL, the delay between laser pulses is approximately twice the longest lifetime obtained in TRPL (20 ns). However, negative delay PL indicate an accumulation regime which could explain why the obtained lifetimes are shorter in TRPL than in extended pump-probe photo-reflectivity. The excitation density is also higher and this may also be involved. Enhancing the delay between pulses and reducing the excitation power could enable to observe longer lifetimes.
Concerning the spin relaxation time, it seems that accumulation does not affect the T_2 time. Indeed, the maximum time obtained in regime (ii) is very close to the one observed in regime (iii). However, this does not explain why the spin relaxation time measured in polar resolved TRPL is shorter. It should be imputed to the fact that we have only one point ($V_G = -0.9$ V) which does not necessarily correspond to the maximum of $\tau_S(V)$.

Measurements under magnetic field have also provided access to the g-factor which

is found to be about $g = 0.26$. We interpret the origin of the signal in pump-probe measurements as coming from electrons - because holes and excitons are inaccessibles - which could be free or bound in an exciton. And yet, the obtained g-factor is higher than values reported in the literature for 8 nm GaAs/AlGaAs QW (our narrow QW) and correspond rather t what one would expect for 12 nm GaAs/AlGaAs QW (our wide QW) [27, 42, 43].
This surprising value might be explained by an overflow of the wavefunction of the electron out of the well due to the asymmetry. However, numerical simulation does not indicate any clue in this direction. We have also considered the influence of the Al concentration or the width of the wide well and none of these parameter can explain this value.

An other interesting point is the presence of two contributions in the signal. These contributions having very close g-factors, they are hard to unravel at least in the standard pump-probe configuration. At low magnetic fields, we are not able to conclude the presence of one or two contributions. However, they appears clearly for $|V_G|$ higher than the gate voltage of the peak of spin relaxation time. This could be imputed to the presence of electrically injected electrons. This could be confirmed by simultaneous electrical measurement during optical measurement.

4.7 Conclusion and perspectives

In conclusion, we have studied by PL and pump-probe spectroscopy the density and spin dynamics of IX at low temperatures in asymmetric CQWs with two distinct DX resonances that can be addressed independently. We have experienced the following technical issues. First, the IX emission is weak and the n^+-layer hinders both its emission and its polarisation. Then, the electrical behaviour of the structure is not reliable making it hard to analyse our data. Finally, our initial goal to probe independently the two direct resonances can not be reached in this structure. Here, we discuss their consequences and also propose potential solutions.

As we have seen, the n^+-layer emission have a lifetime about ≈ 1 ns. Time-resolved measurements under pulsed excitation therefore enable to circumvent this issue. However, IX can only be studied after the first few ns. In addition to the weakness of their emission, this is a strong constraint because the typical observed decay times are longer but in the order of a few ns. Therefore, the IX signal has already strongly declined after the limitation period imposed by the n^+-layer emission. In concrete

terms, sufficient signal-to-noises ratio require minimal acquisition times of several minutes in PL.
Despite these experimental difficulties, we observed long lifetime (up to several tens of ns) and spin relaxation time about 5 ns in time-resolved PL and up to 25 ns in pump-probe spectroscopy. This difference evidences an other issue: when IX have a lifetime comparable or longer than the period between two laser pulses, we observe an accumulation regime which deteriorate both their lifetime and their spin relaxation time. This imposes us to slow down the repetition rate of the laser, at the expense of longer acquisition times making systematic measurement harder. Nonetheless, longer characteristic times should be obtained on this sample with adapted setups (the extended pump-probe for instance or a modified TRPL setup).

The uncontrolled electrical dependence of the IX transition has also been a major impediment in performing systematic measurements. The threshold voltage of both the emergence of long time (transition from DX to IX as the ground state) and of the maximum of the spin relaxation time changes from one set of measurement to an other. Successive heating and cooling are incriminated but other reasons - related to the sample or to the electrical setup as well - could exist.
Electrical connection implemented in our setup - from the top of the cryostat to the socket and from the socket to each trap - should therefore be characterised at low temperatures for high impedance samples.
It should also be considered to work on a more mature technology, providing samples with a well controlled electrical behaviour, hence a better reproducibility. An example of more reliable samples can be found in [18, 19, 44, 45].
On this occasion, it would also be advisable to invert the respective position of the wide and the narrow wells. Indeed, the electrical behaviour of an ACQW in which the electrons lie on the wide well rather than in the narrow well is expected to be simpler. While the respective confinement potential of such ACQW structures ideally differ only by the sign of the electric field, in practice, the Schottky junction prevents the application of a positive electric field, this explain why an other structure is required.
Because numerical simulations do not take into account the environment of the CQW, they allow for the comparison of the two situations by changing the sign of the electric field. Figure 4.26 shows such numerical simulations for the 12-4-8 structure at negative (left panel) and positive (right panel) electric fields. The IX formed with the electron in the wide well becomes the ground state at very lower - positive - field than the IX formed with the electron in the narrow well. This situation should be better suited for the study of IX because they appear at lower electric fields, hence at lower currents.

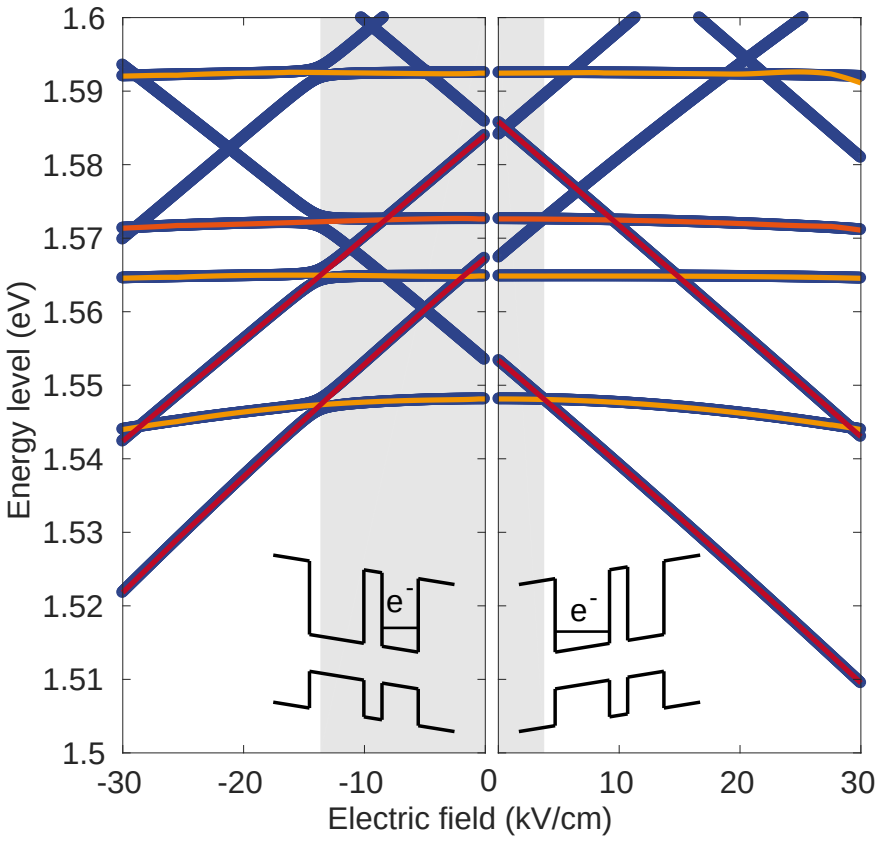

Figure 4.26: Numerical simulation of the 12-4-8 structure for negative (left panel) and positive electric fields (right panel). Both situations are depicted on the bottom of the figure.

Finally, the absence of non-linear signal resonant with the narrow well raises the question of the possibility of probing dark states. In [24], the coupling of the IX and DX subpopulations is considered to be due to exchange interaction and to be identical for each resonance. Non-degenerate pump-probe spectroscopy of this structure should question this assumption. It would actually be rewarding to pump the DX_W transition and to probe the DX_N and vice-versa. Here again, the study of the two different structures - 8-4-12 and 12-4-8 nm - would also provide new indications to understand why only one transition can be probed.

Bibliography

[1] C. Abbas, F. Chiaruttini, S. Cronenberger, D. Scalbert, F. Dubin, A Lemaître, and M. Vladimirova. Spin relaxation of indirect excitons in asymmetric coupled quantum wells. *Superlattices and Microstructures*, 122:643–649, 2018. [4]

[2] Mussie Beian, Mathieu Alloing, Edmond Cambril, Carmen Gomez Carbonell, Johann Osmond, Aristide Lemaître, and François Dubin. Long-lived spin coherence of indirect excitons in GaAs coupled quantum wells. *EPL*, 110(2):27001–5, April 2015. [4.1, 4.2, 4.2, 4.5.1, 4.5.2, 4.6.2]

[3] J. R. Leonard, Y. Y. Kuznetsova, Sen Yang, L. V. Butov, T. Ostatnický, A. Kavokin, and A. C. Gossard. Spin transport of excitons. *Nano Lett*, 9:4204–4208, 2009. [4.5.1, 4.5.2]

[4] A Violante, R Hey, and P V Santos. Coherent transport and manipulation of spins in indirect-exciton nanostructures. *Phys. Rev. B*, 91(12):125302, March 2015. [4.5.2]

[5] K Kowalik-Seidl, X P Vögele, B N Rimpfl, S Manus, J P Kotthaus, D Schuh, W Wegscheider, and A W Holleitner. Long exciton spin relaxation in coupled quantum wells. *Appl. Phys. Lett.*, 97(1):011104, 2010. [4.5.2]

[6] Peristera Andreakou, Steeve Cronenberger, Denis Scalbert, A Nalitov, NA Gippius, AV Kavokin, Michal Nawrocki, JR Leonard, LV Butov, KL Campman, et al. Nonlinear optical spectroscopy of indirect excitons in coupled quantum wells. *Physical Review B*, 91(12):125437, 2015. [4.1, 4.2, 4.5.1, 4.5.1, 4.5.2, 4.5.2, 4.6.1, 4.6.1, 4.6.2]

[7] Ran Finkelstein, Kobi Cohen, Benoit Jouault, Ken West, Loren N Pfeiffer, Masha Vladimirova, and Ronen Rapaport. Transition from spin-orbit to hyperfine interaction dominated spin relaxation in a cold fluid of dipolar excitons. *Phys. Rev. B*, 96(8):085404, August 2017. [4.1, 4.2, 4.5.1, 4.5.2]

[8] LV Butov, LS Levitov, AV Mintsev, BD Simons, AC Gossard, and DS Chemla. Formation mechanism and low-temperature instability of exciton rings. *Physical review letters*, 92(11):117404, 2004. [4.1]

[9] Mathieu Alloing, Mussie Beian, Maciej Lewenstein, David Fuster, Yolanda González, Luisa González, Roland Combescot, Monique Combescot, and François Dubin. Evidence for a bose-einstein condensate of excitons. *EPL (Europhysics Letters)*, 107(1):10012, 2014. [4.1, 4.1]

[10] A. A. High, J. R. Leonard, A. T. Hammack, M. M. Fogler, L. V. Butov, A. V. Kavokin, K. L. Campman, and A. C. Gossard. Spontaneous coherence in a cold exciton gas. *Nature*, 483:584–588, 2012. [4.1]

[11] A. A. High, A. T. Hammack, J. R. Leonard, Sen Yang, L. V. Butov, T. Ostatnický, M. Vladimirova, A. V. Kavokin, T. C. H. Liew, K. L. Campman, and A. C. Gossard. Spin currents in a coherent exciton gas. *Phys. Rev. Lett.*, 110:246403, 2013. []

[12] Mathieu Alloing, Mussie Beian, Maciej Lewenstein, David Fuster, Yolanda González, Luisa González, Roland Combescot, Monique Combescot, and François Dubin. Evidence for a Bose-Einstein condensate of excitons. *EPL*, 107(1):10012, July 2014. [4.1, 4.1]

[13] L. V. Butov, A. C. Gossard, and D. S. Chemla. Spontaneous coherence in a cold exciton gas. *Nature*, 418:751–754, 2002. [4.1]

[14] L V Butov. Condensation and pattern formation in cold exciton gases in coupled quantum wells. *J. Phys.: Condens. Matter*, 16(50):R1577–R1613, December 2004. []

[15] L. V. Butov, L. S. Levitov, A. V. Mintsev, B. D. Simons, A. C. Gossard, and D. S. Chemla. Formation mechanism and low-temperature instability of exciton rings. *Phys. Rev. Lett.*, 92:117404, 2004. [4.1]

[16] Yehiel Shilo, Kobi Cohen, Boris Laikhtman, Ken West, Loren Pfeiffer, and Ronen Rapaport. Particle correlations and evidence for dark state condensation in a cold dipolar exciton fluid. *Nature communications*, 4:2335, 2013. [4.1]

[17] Michael Stern, Vladimir Umansky, and Israel Bar-Joseph. Exciton liquid in coupled quantum wells. *Science*, 343(6166):55–57, 2014. [4.1]

[18] Mussie Beian, Mathieu Alloing, Romain Anankine, Edmond Cambril, Carmen Gomez Carbonell, Aristide Lemaître, and François Dubin. Spectroscopic signatures for the dark bose-einstein condensation of spatially indirect excitons. *EPL (Europhysics Letters)*, 119(3):37004, 2017. [4.1, 4.1, 4.7]

[19] Romain Anankine, Mussie Beian, Suzanne Dang, Mathieu Alloing, Edmond Cambril, Kamel Merghem, Carmen Gomez Carbonell, Aristide Lemaître, and François Dubin. Quantized vortices and four-component superfluidity of semiconductor excitons. *Physical review letters*, 118(12):127402, 2017. [4.1, 4.7]

[20] AT Hammack, NA Gippius, Sen Yang, GO Andreev, LV Butov, M Hanson, and AC Gossard. Excitons in electrostatic traps, 2006. [4.1, 4.2]

[21] Monique Combescot, Odile Betbeder-Matibet, and Roland Combescot. Bose-einstein condensation in semiconductors: The key role of dark excitons. *Physical review letters*, 99(17):176403, 2007. [4.1]

[22] Monique Combescot, Roland Combescot, Mathieu Alloing, and François Dubin. Optical signatures of a fully dark exciton condensate. *EPL (Europhysics Letters)*, 105(4):47011, 2014. [4.1]

[23] M Combescot and M N Leuenberger. General argument supporting Bose–Einstein condensate of dark excitons in single and double quantum wells. *Solid State Communications*, 149(13-14):567–571, April 2009. [4.1]

[24] AV Nalitov, Maria Vladimirova, AV Kavokin, LV Butov, and NA Gippius. Nonlinear optical probe of indirect excitons. *Physical Review B*, 89(15):155309, 2014. [4.1, 4.5.2, 4.7]

[25] LV Butov, A Imamoglu, AV Mintsev, KL Campman, and AC Gossard. Photoluminescence kinetics of indirect excitons in g a a s/a l x ga 1- x as coupled quantum wells. *Physical Review B*, 59(3):1625, 1999. [4.2]

[26] Romain Anankine, Mussie Beian, Suzanne Dang, Mathieu Alloing, Edmond Cambril, Kamel Merghem, Carmen Gomez Carbonell, Aristide Lemaître, and François Dubin. Quantized Vortices and Four-Component Superfluidity of Semiconductor Excitons. *Phys. Rev. Lett.*, 118(12):127402, March 2017. [4.2]

[27] M Poggio, GM Steeves, RC Myers, NP Stern, AC Gossard, and DD Awschalom. Spin transfer and coherence in coupled quantum wells. *Physical Review B*, 70(12):121305, 2004. [4.2, 4.6.2]

[28] L. V. Butov, A. Imamoglu, A. V. Mintsev, K. L. Campman, and A. C. Gossard. Photoluminescence kinetics of indirect excitons in GaAs/$Al_xGa_{1-x}As$ coupled quantum wells. *Phys. Rev. B*, 59:1625–1628, 1999. [4.5.1]

[29] Yotam Mazuz-Harpaz, Kobi Cohen, Boris Laikhtman, Ronen Rapaport, Ken West, and Loren N Pfeiffer. Radiative lifetimes of dipolar excitons in double quantum wells. *Phys. Rev. B*, 95(15):155302, April 2017. [4.5.1]

[30] B Laikhtman and Ronen Rapaport. Correlations in a two-dimensional Bose gas with long-range interaction. *EPL*, 87(2):27010, July 2009. [4.5.1]

[31] AL Ivanov. Quantum diffusion of dipole-oriented indirect excitons in coupled quantum wells. *EPL (Europhysics Letters)*, 59(4):586, 2002. [4.5.1]

[32] Christoph Schindler and Roland Zimmermann. Analysis of the exciton-exciton interaction in semiconductor quantum wells. *Physical Review B*, 78(4):045313, 2008. [4.5.1]

[33] B Laikhtman and R Rapaport. Exciton correlations in coupled quantum wells and their luminescence blue shift. *Physical Review B*, 80(19):195313, 2009. [4.5.1]

[34] M. Z. Maialle, E. A. de Andrada e Silva, and L. J. Sham. Exciton spin dynamics in quantum wells. *Phys. Rev. B*, 47:15776–15788, 1993. [4.5.1]

[35] EA de Andrada e Silva, GC La Rocca, and F Bassani. Spin-orbit splitting of electronic states in semiconductor asymmetric quantum wells. *Physical Review B*, 55(24):16293, 1997. [4.5.1]

[36] M Poggio, G M Steeves, R C Myers, N P Stern, A C Gossard, and D D Awschalom. Spin transfer and coherence in coupled quantum wells. *Phys. Rev. B*, 70(12):121305–4, September 2004. [4.5.1]

[37] Erasmo A de Andrada e Silva and Giuseppe C La Rocca. Exciton-bound electron-spin relaxation. *Physical Review B*, 56(15):9259, 1997. [4.5.1]

[38] M Dyakonov, X Marie, T Amand, P Le Jeune, D Robart, M Brousseau, and J Barrau. Coherent spin dynamics of excitons in quantum wells. *Physical Review B*, 56(16):10412, 1997. [4.5.1]

[39] VV Belykh, E Evers, DR Yakovlev, F Fobbe, A Greilich, and M Bayer. Extended pump-probe faraday rotation spectroscopy of the submicrosecond electron spin dynamics in n-type gaas. *Physical Review B*, 94(24):241202, 2016. [4.18, 4.6.1]

[40] G Salis, DT Fuchs, JM Kikkawa, DD Awschalom, Y Ohno, and H Ohno. Optical manipulation of nuclear spin by a two-dimensional electron gas. *Physical review letters*, 86(12):2677, 2001. [4.6.1]

[41] Z Vardeny and J Tauc. Picosecond coherence coupling in the pump and probe technique. *Optics Communications*, 39(6):396–400, 1981. [4.6.2]

[42] MJ Snelling, E Blackwood, CJ McDonagh, RT Harley, and CTB Foxon. Exciton, heavy-hole, and electron g factors in type-i gaas/al x ga 1- x as quantum wells. *Physical Review B*, 45(7):3922, 1992. [4.6.2]

[43] P Andreakou, AV Mikhailov, S Cronenberger, D Scalbert, A Nalitov, AV Kavokin, M Nawrocki, LV Butov, KL Campman, AC Gossard, et al. Influence of magnetic quantum confined stark effect on the spin lifetime of indirect excitons. *Physical Review B*, 93(11):115410, 2016. [4.6.2]

[44] Romain Anankine, Suzanne Dang, Mussie Beian, Edmond Cambril, Carmen Gomez Carbonell, Aristide Lemaitre, and François Dubin. Temporal coherence of spatially indirect excitons across bose–einstein condensation: the role of free carriers. *New Journal of Physics*, 20(7):073049, 2018. [4.7]

[45] Suzanne Dang, Romain Anankine, Carmen Gomez, Aristide Lemaître, Markus Holzmann, and François Dubin. Defect proliferation at the quasicondensate crossover of two-dimensional dipolar excitons trapped in coupled gaas quantum wells. *Physical Review Letters*, 122(11):117402, 2019. [4.7]

Conclusion

In this work, two different systems are investigated: electron gases in CdTe thin layers and indirect excitons in GaAs/(AlGa)As asymmetric CQW. Their common denominator is the optical study of spin dynamics which is much less known in CdTe than in GaAs.

Here, we provide the first SN-based study of electron spin dynamics in n-CdTe. It allows for the observation of the electron spin precession in the frozen random nuclear spin fluctuations at low temperatures. This precession manifests itself as a contribution in the SN spectra centred on a non-zero frequency, even in the absence of magnetic field. It allows for the determination of the nuclear field at saturation in CdTe which is found to be $B_S = 0.094$ T.
This observation is quite intriguing for samples with high nominal doping densities because it implies long correlation times τ_c on a donor site. We have therefore developed an innovative SNS setup which offers the possibility of reaching both temporal and spatial correlations of a spin system. The basic idea of this setup consists in introducing a wave vector difference q between the probe and the local oscillator and in examining the resulting modification of the SN spectra. Here, we report on the first implementation of such a setup and provide the explicit formulation of the evolution of SN spectra with q, taking into account the influence of the imaging system. We experimentally demonstrate the expected broadening of SN spectra with q and also clarify the dependence of the SN intensity on potential spatial spin correlations.
In CdTe thin layers, it enables us to measure simultaneously - that means in strictly similar conditions - the electron spin relaxation time and the electron spin diffusion coefficient, and thus to determine the corresponding correlation time τ_c. Varying the experimental conditions, we were able to explore a wide range of τ_c and hence to observe different spin dynamics regimes. The evolution of the spin relaxation time as a function of τ_c can be well described in terms of a competition between the hyperfine interaction and the anisotropic exchange interaction. However, it imposes

us to consider a doping density several order of magnitude lower than the nominal values of the studied samples. It therefore evidences that our knowledge of electron spin dynamics in GaAs can not be directly transposed to CdTe.
The first part of this thesis opens up two main perspectives. On the one hand, a systematic study of n-CdTe layers with different - and well controlled - doping levels should allow for a better comprehension of spin dynamics in CdTe. On the other hand, our brand new setup is expected to detect spatial correlations characterised by a correlation length longer than or equal to 0.3 μm. Sufficient characteristic length can be found in different systems such as persitent spin helix for instance.

In the second part of this work, we carry out the first comparative study between time-resolved PL and pump-probe spectroscopy of indirect excitons in asymmetric CQW. Under appropriate electric fields, we obtained both long lifetimes and long spin relaxation times just as in symmetric structures. Nevertheless, the unreliability of the field-effect structure compromises a straightforward quantitative comparison. The shift of the IX emission actually depends on successive cooling and heating cycles of the sample. The gate voltage dependence of the measured times are therefore different for each set of experiments, making a direct comparison difficult. Despite very constraining experimental conditions, we have also evidenced the negative role of the IX accumulation and possibly of electrically injected carriers.
In addition, the studied structure was expected to give an access to spin and density dynamics of dark indirect excitons. This access should have been provided in pump-probe spectroscopy by probing independently each direct transition. However, we were only able to probe the wide well. This issue is still unexplained and could indicate that the DX-IX interactions taken into account in this method are more complicated than expected.
In this context, two complementary approaches can be explored to develop further this study. On the one hand, we could envisage better suited experimental setups. In TRPL, lower repetition rates are needed to avoid the IX accumulation. In pump-probe spectroscopy, the extended configuration serves very well its purpose and complementary experiments would be interesting. However, the impossibility to remove the degeneracy between the pump and the probe is restricting. Pumping a direct resonance and probing the other, or studying the evolution of the signal when the energy varies would provide precious information to understand why no signal has been obtained in the narrow well.
On the other hand, moving on a new technology of structure seems to be essential. Designs with double top electrodes (in and out the traps) may for instance enable a better controlled electric field. A reasonable repeatability would allow for a reliable

study of lifetime and spin relaxation time voltage-dependence, and therefore for the determination of optimal conditions. On this occasion, it would be relevant to invert the relative position of the wells. Indirect excitons would actually appear at lower electric fields, hence in better experimental conditions.

Finally, a SN-based study of indirect excitons could be a more distant prospect common to both aspect of this work. Spin relaxation time of several ns - as we have measured here - are actually compatible with the spin noise spectroscopy. In this case, the exciton spin system should be created by a linearly polarised pump, and then, its spontaneous spin fluctuations should be probed.
Furthermore, IX systems are potentially well suited to take advantage of the new possibility offered by our setup, that is the detection of spatial spin correlations. Of course, these exciting perspectives will be practicable only if a strong control of the electrical behaviour of the structure is achieved.

Titre de la thèse en français:

Spectroscopie optique du spin d'excitons indirects et d'électrons dans les nanostructures semiconductrices

Résumé de la thèse en français:

Ce travail porte sur l'étude optique de la dynamique de spin de deux systèmes: un gaz d'électrons dans des couches minces de CdTe d'une part et des excitons indirects dans un double puits quantique asymétrique en GaAs d'autre part.
Des mesures de photoluminescence résolue en temps et en polarisation et des mesures de spectroscopie pompe-sonde ont permis la détermination des temps de vie et des temps de relaxation de spin des excitons indirects. Le comportement général de la structure a été décrit, les contraintes techniques ont été mise en évidence et les meilleurs conditions expérimentales ont été identifiées. En photoluminescence, nous avons mesuré des temps de vie de l'ordre de la quinzaine de ns et des temps de relaxation de spin de 5 ns dans le meilleur cas. L'utilisation d'un setup de spectroscopie pompe-sonde permettant d'étudier des délais très longs a démontré que des temps plus longs peuvent être atteints en séparant d'avantage deux impulsions lasers successives.
Pour les électrons dans CdTe nous avons utilisé une autre méthode optique: la spectroscopie de bruit de spin qui s'est récemment imposée comme un outil de choix pour étudier la dynamique de spin dans les semiconducteurs. Son principe consiste à sonder la dynamique d'un système de spins à travers ses fluctuations spontanées. Pour ce faire, ces fluctuations sont encodées dans le plan de polarisation d'un laser hors résonnant par l'intermédiaire de la rotation Faraday.
Alors que les réalisations concrètes de cette technique se limitaient jusqu'à présent aux corrélations temporelles, nous proposons ici la première implémentation permettant d'accéder aussi aux corrélations spatiales du systèmes de spin. Cet accès à la dynamique spatiale est autorisé par une sélectivité en vecteur d'onde de la lumière diffusée venant de l'échantillon et nous offre l'opportunité de mesurer simultanément le temps de relaxation de spin et le coefficient de diffusion de spin. Ayant ainsi une vision complète de la dynamique de spin dans CdTe, nous avons pu confronter la physique du spin bien connue dans GaAs à nos observations dans CdTe. Contre toutes attentes, il semblerait que nos connaissances de GaAs ne soient pas directement transposables à CdTe.

Mots clés en français:

Dynamique de spin, Spectroscopie de bruit de spin, Excitons indirects

Titre de la thèse en anglais:

Optical spectroscopy of indirect excitons and electrons spin in semiconductor nanostructures

Résumé de la thèse en anglais:

This work provides an optical study of spin dynamics in two different systems: electron gas in n-doped CdTe thin layers and indirect excitons in asymmetric GaAs coupled quantum wells.
Time and polar resolved photoluminescence and pump-probe spectroscopy allowed the determination of both the lifetime and the relaxation time of indirect excitons. The global behaviour of the dedicated biased sample has been described, major technical constraints have been pointed out and optimal working conditions have been identified. In photoluminescence, we obtained lifetime of $\tau_r = 15$ ns and spin relaxation time of $\tau_s = 5$ ns. Pump-probe spectroscopy with an exceptional delay range shown that longer characteristic times could be obtained increasing the delay between two laser pulses.
An other optical method has been used for study electrons in CdTe thin layers. Spin noise spectroscopy has recently emerged as an ideal tool to study dynamics of spin systems through their spontaneous fluctuations which are encoded in the polarisation state of a laser beam by means of Faraday rotation. Common spin noise setups provide only temporal fluctuations, spatial informations being lost averaging the signal on the laser spot. Here, we demonstrate the first implementation of a spin noise setup providing both spatial and temporal spin correlations thanks to a wave vector selectivity of the scattered light. This gave us the opportunity to measure both the spin relaxation time and the spin diffusion coefficient. This complete vision of the spin dynamics in CdTe has been compared to our understanding of spin physics in GaAs. Against all odds, this knowledge seems to be not directly transposable from GaAs to CdTe.

Mots clés en anglais:

Spin dynamics, Spin noise spectroscopy, Indirect excitons